Doctoral thesis

Magnetism at the nanoscale: Electron spin resonance

Jose Reina Gálvez

Supervisor	Co-supervisor
Nicolás Lorente Palacios	Fernando Delgado Acosta

March 25, 2021

eman ta zabal zazu

Universidad del País Vasco
Euskal Herriko Unibertsitatea

Contents

Acknowledgements

Hacer un doctorado siempre es duro, ya me lo comentaron muchos desde el principio. Sin embargo, por suerte, el viaje nunca se hace solo. Ya sea por las personas que ya estaban en tu vida antes del doctorado o por las que conoces en el camino. Eso sí, y aunque no sea yo la persona más familiar del mundo, no puedo sino estar increíblemente agradecido a mi madre por todo el sacrificio que hizo para que me sacara la carrera en su día y por estar ahí siempre. También agradezco a mi hermano, abuela y familiares cercanos.

Eso sí, no considero menos importante a la familia que uno elije. A los compañeros de la facultad de Sevilla, Javi, Gonzi y Antonio, les digo que a ver si es posible reunirnos este año, que se os extraña bastante. A los chavales del CFM, DIPC, nanogune les estaré siempre agradecidos por el buenísimo ambiente que siempre hemos tenido y las cantidad de cervezas que cayeron para aliviar el doctorado. Mención especial para Mariarita, Lars, Aaron, Carmelo, Pablo, Raúl, Carmen, Marina y Matteo. Fuera del ambiente científico, debo agradecer muchísimo Fernando y Carlos, amigos que me conocen más que mi madre prácticamente, por todo lo que me habéis apoyado. Sobretodo a Carlos que raro es el día en el que no nos hemos quejado de algo relacionado con nuestros doctorados. Por supuesto, tengo que agradecer a mis compañeros de piso David y Elena. Simplemente por el hecho de vivir conmigo ya tienen el cielo ganando. Por eso y por la buena cantidad de series que hemos visto en estos tiempos de Covid. Y como no, muchas gracias a Soledad por aguantar mis quejas de la tesis y tener una paciencia infinita para apoyarme.

Para terminar, como no agradecer a mis jefes por sus encomendables labores para sacar esta tesis adelante. Sin sus innumerables consejos y charlas distendidas, nada habría sido lo mismo.

Resumen

Scanning tunneling microscope (STM) lleva revolucionando el campo de la materia condensada desde hace unos años. Esta técnica ofrece tanto una gran resolución espacial como energética, permitiendo la manipulación atómica gracias a un control de la punta a nivel subatómico. Sin embargo, desde 2015, una nueva técnica con mayor resolución energética e igual espacial apareció: Electrón Spin Resonance (ESR). La gran diferencia con STM viene de modular la diferencia de potencial entre la punta y el substrato a través de un voltaje alterno AC. Cuando la frecuencia de este campo eléctrico coincide con la separación enérgica (frecuencia de Larmor) entre dos estados de un momento magnético localizado en una superficie aislante, la corriente sufre un cambio brusco. De esta forma, el espín del momento magnético empieza a precesar.

Algunas de las aplicaciones más interesantes que ofrece esta técnica han sido la identificación de distintos isotopos de Ti y Fe, así como obtener información de átomos con electrones tipo f como el Ho. También, recientemente, se está intentado hacer manipulación coherente entre átomos magnéticos. De esta forma, se podrían realizar operaciones cuánticas que tendrían un gran impacto en el campo de la información cuántica. Sin embargo, un marco teórico de predicción todavía no ha sido descubierto. La gran dificultad recae en como puede afectar un campo eléctrico alterno al espín atómico. Las propuestas han sido varias: desde excitaciones de fonones en la superficie hasta desplazamientos del átomo magnético, entre otras. El objetivo de esta tesis es arrojar un poco de luz a este asunto y obtener un modelo teórico que pueda predecir y simular experimentos.

Inicialmente aplicaremos Density Functional Theory (DFT) para intentar sacar algunas primeras conclusiones de como el sistema magnético (Fe sobre MgO/Ag(001)) reacciona

ante un campo eléctrico. Para ello, primero, debemos seguir un procedimiento estándar de relajación de los sistemas bulk del MgO y Ag. Extrayendo los parámetros de red correspondientes y construyendo la superficie MgO/Ag en la que colocaremos el átomo magnético sobre un O. La exposición a un campo eléctrico estático nos permite ver que cambios hay en la PDOS y en el planar average potential (PAP). Las conclusiones resultan inmediatas: el campo eléctrico afecta mucho más el PAP, lo que implica que se este modulando la barrera de potencial. Es interesante apreciar que en otros sistemas como Cu_2N/Cu o ClCu/Cu no se tiene una respuesta tan notable con el campo eléctrico.

Con la conclusión anterior, empezamos a aplicar ciertos modelos teóricos que podrían permitir simular los experimentos. El primero es el llamado cotunneling. Inicialmente se parte de un Hamiltoniano total que contiene el Hamiltoniano del entorno, el del sistema central o impureza magnética (modelo de Anderson generalizado) y la conexión entre ambos, llamado tunneling. Dicho Hamiltioniano resulta demasiado complejo de tratar por lo que se aplica teoría de perturbaciones a segundo orden en el término tunneling. El objetivo detrás de esta aproximación es conseguir escribir el llamado Hamiltoniano de cotunneling, cuya forma permite usar la teoría Bloch-Redfield. Dicha teoría aplica un lenguaje de matrices de densidad muy práctico para problemas de sistemas abiertos pero, además, es fácilmente extensible al regimen con dependencia temporal que nos interesa. Teniendo en cuenta ciertas consideraciones, el producto final de mezclar cotunneling con dependencia temporal nos lleva a una ecuación de los elementos de la matriz de densidad reducida que presenta un nuevo parámetro. Este parámetro resulta estar asociado a la precesión del espín y se le llama frecuencia de Rabi.

Los resultados del modelo de cotunneling muestran que la frecuencia de Rabi es el pilar fundamental de la teoría. Sin este parámetro, no es posible inducir resonancia ya que la altura del pico en la corriente es directamente proporcional al cuadrado de la Rabi. Aunque los cálculos con la teoría son bastante satisfactorios, los valores de la frecuencia de Rabi resultan ser un factor 10-20 más grandes que los experimentales. Un rápido vistazo al modelo y las ecuaciones empleadas nos dice que hemos tendido a sobresimplificar demasiado los cálculos. Varias estrategias pueden ejecutarse para mejorar estos pero, sin duda, la más destacable es usar Wannier para conocer mejor la hibridación entre el sistema

y el entorno. Sin embargo, esto es algo que escapa del contenido de la tesis.

La siguiente teoría que empleamos, en un intento de mejorar los resultados de cotunneling, es la de Floquet combinada con funciones de Green fuera del equilibrio. La teoría de Floquet estudia la estabilidad de sistema de ecuaciones diferenciales periódicos y permite reescribirlos como uno algebraico mediante el uso del teorema de Floquet. En nuestro caso, partimos de un Hamiltoniano total parecido al no perturbado del cotunneling y aplicamos funciones de Green junto con operadores Hubbard. Así, llegamos a una ecuación diferencial en los elementos reducidos de la matrix de la densidad que cumple la forma requerida para aplicar Floquet. De esta forma, podemos transformar dicho sistema de ecuaciones en uno algebraico, resolverlo y calcular la corriente junto con cualquier otro observable del sistema. La forma en la que definimos el Hamiltoniano del sistema nos permite introducir interacciones entre espines y simular otros experimentos ESR más recientes.

De las ecuaciones master de Floquet que derivamos podemos calcular todos los parámetros que afectan a la señal ESR tales como los tiempos de vida, de decoherencia o la frecuencia de Rabi de forma natural. En cualquier caso, en el momento de escribir la tesis, este último modelo aún no ha sido totalmente explorado. Por tanto, tenemos margen de mejora de cara a los resultados. Sin embargo, cabe destacar que estos resultan ser bastante satisfactorios.

Abstract

Scanning tunneling microscope (STM) has revolutionized the field of condensed matter physics since years. The reason why comes from offering an amazing spatial and energy resolutions, which allows to manipulate atoms thank to a precise control of the tip. However, since 2015, a new technique emerged with a better energy resolution and the same amazing spatial one. The technique is called Electron Spin Resonance (ESR). The ESR-STM technique consists in modulating the tip-surface bias potential with a radiofrequency (AC) component. When the frequency matches the Larmor frequency of a local magnetic moment, the current changes rapidly and the spin precesses.

Some of the most interesting application have been the identification of isotopes of Ti and Fe, and to gather information on the elusive f-electron of Ho atoms. Recently, STM-ESR has been used to make coherence manipulation of local magnetic atoms. In this way, quantum operations could be possible and it could revolutionize the field of quantum information. However, the mechanism is still not perfectly understood. The challenge is to fully comprehend how the electric field can alter a magnetic moment. Different mechanisms have been proposed: phonons excitations, displacement of the magnetic atom etc. The aim of this thesis is light up this questions and trying to come up with a theoretical model that can simulate and predict experiments.

Initially, we will apply Density Functional Theory (DFT) in order to gather information on the magnetic system (Fe on MgO/Ag(001)) when an electric field is applied. To this end, we follow the standard procedure of relaxation of the bulk system MgO and Ag. After extracting the lattice parameter, we build the surface MgO/Ag(001) and place the Fe on the top O. If we now compute the PDOS and planar average potential (PAP) for different

electric fields, we can easily see that PAP feel it significantly more. Therefore, we can conclude that the electric field is modulating the tunneling barrier. It is worthy to notice that the surface Cu_2N/Cu o $ClCu/Cu$ feels the electric field much less compare to the MgO/Ag surface.

With this information, we can start applying certain theories that could allow us to simulate the experiments. We first try the cotunneling approach. We use a Hamiltonian that contains the reservoirs, the impurity Hamiltonian (generalized Anderson model) and the connection between both, called tunneling Hamiltonian. This last contribution is approximated by perturbation theory up to second order. The objective is to derive a cotunneling Hamiltonian from this approximation and apply Bloch Redfield theory. This theory is extremely useful for open quantum system such that ESR because it uses a density matrix language. The theory can be easily expanded to time dependent problems too. Combining cotunneling and Bloch-Redfield lead master equation that contains a new parameter: the Rabi frequency. Rabi frequency becomes essential to explain the ESR. Without it, the spin do not precess since the resonance peak is proportional to the square of the Rabi frequency.

Even though the cotunneling results are quite satisfactory, the Rabi frequency is still a factor 10-20 larger than the one we find in the experiments. A quick look at the expression we are using gives us the reason of this discrepancy: we are oversimplifying the calculations. To improve the results one could apply Wannier but we are not going to talk about it in this thesis.

The next theory we apply, in order to improve our results, is the Floquet theory together with non equilibrium Green's function. Floquet theory is the study of the stability of linear periodic systems in continuous time. It allows us to transform a time differential system of equation into an algebraic one, using the so called Floquet theorem. If we use a total Hamiltonian similar to the one we talked early, while introducing Hubbard operator and Green's Function, we arrive to a master equation of the reduced density matrix. This master equation satisfies the Floquet condition so that we transform the system into a simpler algebraic one to compute the density matrix element, current or any

other observable. The master equation contains all the ESR important parameter such as lifetime, decoherence times or Rabi frequencies. Moreover, since we also introduce an exchange interaction between spins, we can simulate other experimental situations.

In any case, at the moment of writing the thesis, Floquet Green's function model is still quite unexplored. Therefore, it can be greatly improved and extended even though the results are already quite satisfactory.

Chapter 1

Introduction: ESR-STM Experiment

The *scanning tunneling microscope* (STM) is a surface analysis technique that has revolutionized not only the study of surfaces but virtually all fields of condensed matter physics. The reasons are multiple, but they can be summarized into good energy resolution in resolving electronic states together with unprecedented spatial resolution. The STM consists in a sharp metallic tip etched and atomically manipulated until the tip acquires an atomic edge, that is electrically polarized with respect to a solid surface that can hold atoms, molecules, nanoscopic structures besides complex surfaces. The tip-surface distance can be controlled to sub-Å precision thanks to piezoelectric actuators, and the current established between tip and sample. This current can be made to change rapidly as the tip retracts or approaches the surface leading to enhanced spatial resolution. This is possible because, for tip-surface voltages below the surface or tip work functions, the current takes place via the tunneling effect. Thus, it decreases exponentially with the distance, such that a small change in the separation tip-surface translates into a measurable current that can be controlled with an external feed-back circuit. Figure 1.1 shows a scheme of the STM.

The usual operational modes of the STM are scanning at constant current or scanning at constant tip-surface distance. In the case of constant-current operation, the feedback loop is closed and the tip is allowed to vertically move in order to keep the current constant. The ensemble of x, y, z points of the tip position defines a constant-current STM image.

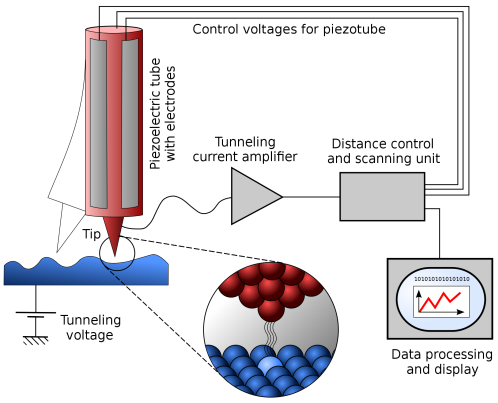

Figure 1.1: Scheme of a scanning tunneling microscope (STM) that polarizes a metallic tip with respect to a conductive surface at low biases (below the work function of the constituents) such that the current proceed via the tunneling effect. Electrons tunnel from tip to substrate if the tip is grounded and the substrate is held at positive bias. At positive bias the current probes empty states of the surface. The piezoelectric system and the atomic termination of the tip grants atomic resolution, because the current changes in atomic distances. (Figure taken from wikipedia)

The other operational mode is to keep the tip-surface distance constant and measure the tunneling current. However, this mode is more difficult to control since the distance changes much less than the current. The tip can be position over interesting spots on a surface (for example a magnetic adatom), and the bias can be increased. In this way the current gives information on the surface states contributing to the current. These states also include excitations of the electronic system such that phonons, magnetic excitations, etc. This is simple to see. When the bias matches some excitation threshold of the studied system, a new conduction channel can open. Indeed, the electron can either transmit elastically, i.e. without exciting the substrate, or inelastically by exciting it. These two possibilities lead to an increase of possible final electronic states, permitting an increase of the current. The increase takes place over the bias threshold, such that an abrupt change in differential conductance, dI/dV, can be measured. The study of the differential conductance as a function of the applied bias is then a powerful local spectroscopy [1, 2].

Figures of merit of the above spectroscopy are ~ 1 meV in energy resolution, together with

0.01 Å in lateral spatial resolution and 0.1 Å in vertical one. These numbers show the precise measurements that can be performed with the STM. Unfortunately, many interactions are smaller and escape to these commom measurements of the STM. However, since 2015, a new technique with the STM has revolutionized the field. *Electron spin resonance* (ESR) can enhance the energy resolution to detect nano-eV shifts while conserving the atomic spatial resolution of the STM. The increase in energy resolution is a millionth of the previous resolution in dI/dV-mode. The ESR-STM technique consists in modulating the tip-surface bias with a radiofrequency (AC) component. This sinuosoidal signal is added to the constant bias and the tunneling current is detected as a function of the signal frequency. When the frequency matches the Larmor frequency of a local magnetic moment, the current changes rapidly, yielding a way of detecting precession frequencies of an atomic spin.

The first experiments of ESR-STM were conductacted by Manassen and co-workers [3, 4]. In these experiments a magnetic field was modulated, instead of the bias, and a detector with a narrow bandwidth was used to detect the time-dependent tunneling current. These experiments showed the presence of ESR features, revealed as an increased noise in the tunnel current at the spin precession frequency [3, 4, 5]. However, the technique proved difficult to perform. Later on, Müllegger *et al.* [6] simplified the setup by using static magnetic fields and using an AC component of the tip-surface bias. They showed that a signal that could be due to ESR was induced in a bis(phthalocyaninato)terbium(III) molecule adsorbed on Au (111). Short after, similar experiments were performed on a single Fe adsorbate on a bilayer of MgO on Ag (001), showing an ESR signal [7].

The demonstration of reproducible single-atom [7] and single-molecule [6, 8] electron spin resonance (ESR) has opened new venues in the analysis of surface science at the atomic scale. Moreover, it can be combined with high-time-resolution pump-and-probe techniques [9, 10]. This has allowed access to the dipolar interaction between close magnetic adatoms, GPS-like localization of magnetic impurities on a surface [11], single-atom magnetic resonance imaging [12], and spectroscopy [13], probing an adatom quantum coherence [14], tailoring the spin interactions between $S = 1/2$ spins [15], measuring and manipulating the hyperfine interaction of individual atoms [16] and molecules [6, 8] or

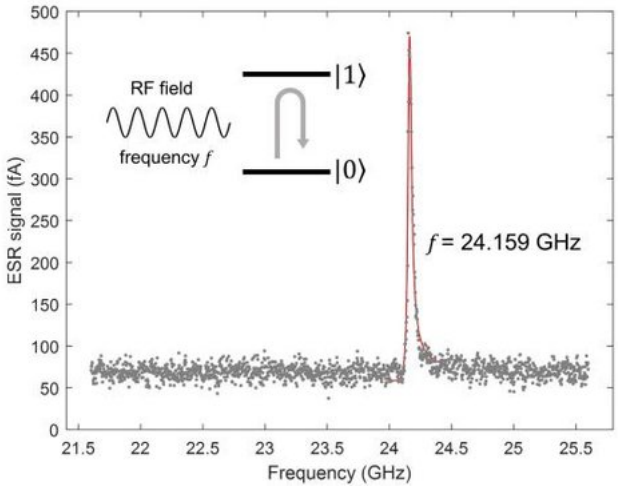

Figure 1.2: ESR spectrum taken with an STM over a Ti atom on a bilayer of MgO on Ag (001). The resonance frequency coincides with the energy difference between the two spin states $\pm 1/2$ in the presence of a static external field of 0.9 T. The bias between tip and sample contains a constant component and a snusoidal component at the frequency marked in the x-axis. The y-axis shows the measured tunneling current. Figure adapted from [15].

controlling the nuclear polarization of individual atoms [17].

Figure 1.2 gives an example [15] of a typical measurement over a Ti atom adsorbed on two layers of MgO grown on Ag (001). The current is measured as a function of the driving frequency, and a clear spike is seen above the resonance frequency. The frequency corresponds to twice the Zeeman splitting of a spin $1/2$ in a 0.9 T magnetic field. This shows that the Ti atom is a spin-1/2 system on the MgO/Ag(001) surface, and the ESR corresponds to inducing Rabi oscillations between the two states with spin proyections $\pm 1/2$.

The experimental data seems to show that magnetic adatoms can display magnetic resonances when they are decoupled from the susbtrate's electrons via an MgO layer. However, molecules may be a different story [6]. All these experiments seem to show that it is the electric field that really couples to the magnetic moment of the studied object. This is somewhat a startling observation because electric fields do not interact with magnetic moment. Here, the time variation of the field induces a magnetic field, but estimates of

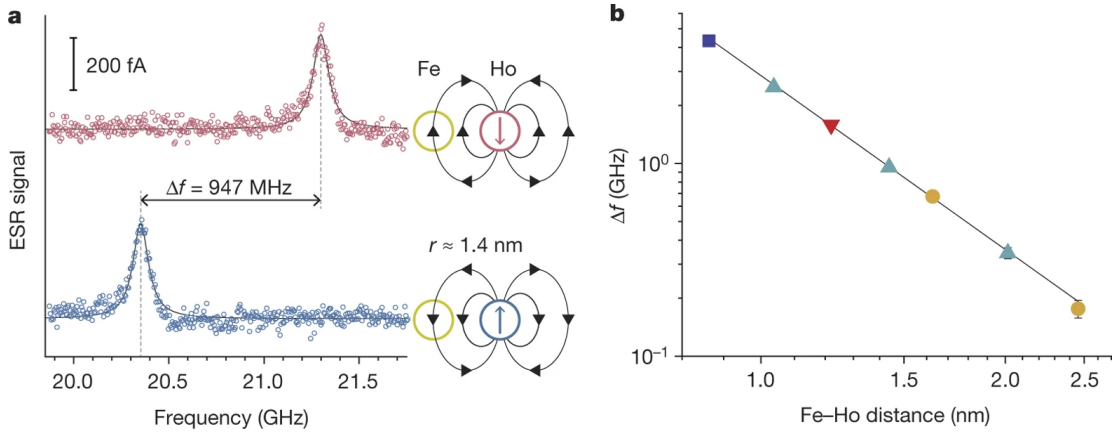

Figure 1.3: The ESR-STM signal (DC current) on an adsorbed Fe on MgO/Ag (001) was recorded showing the characteristic signal for the $S_z \approx \pm 2$ transition, in (a). The shift in the Larmor frequency is due to the dipolar interaction with a neighboring Ho atom as indicated in the sketch. (b) This shift is plotted as a function of distance in a log-log graph. The slope is -3 showing that indeed the interaction is dipolar. These data permitted the authors to fit the magnetic moment of the Ho atom, yielding a value of $(10 \pm 0.1)\mu_B$, in good agreement with the free-atom magnetic moment. Reprinted from Natterer *et al.* [13].

the size of the mangetic field show that the interaction with this field should be negligible [18].

Recent experiments [18, 19] have modified the ESR-STM setup by explicity including a coaxial electrode next to the STM tip. In this way, the macroscopic extra electrode is driven by microwaves and the ending electrode acts as an antenna that radiates the susbtrate. The agreement with the previous experiments is excellent. This shows that indeed the electric field is at the origin of the ESR signal.

In any case, all the experiments mentioned shows how excellent ESR-STM technique can be. Let me get into two dramatic measurements showing at first hand the capabilities of ESR-STM. First, Natterer *et al.* [13] use their well-studied Fe atom on MgO/Ag(001) to gather information on the elusive f-electron Ho atom. Ho atom displays a large magnetic moment due to the contribution of the impaired f-electrons. However, conductance experiments directly performed on Ho atoms do not seem to obtain information on the f-shell due to its very compact structure. Magnetic dipolar interactions that decay as $1/d^3$

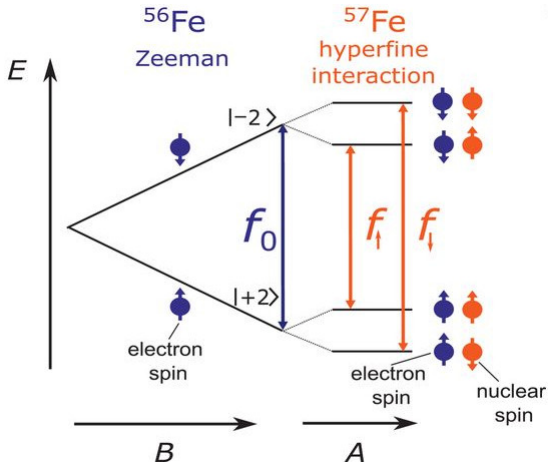

Figure 1.4: The Rabi oscillations giving rise to the electron spin resonance involve flipping spins in a coherent way. When the nuclear spin is interacting with the electronic spin, the nuclear spin can also flip due to the exchange (hyperfine) interaction between the nuclear magnetic moment and the electronic magnetic moment. The scheme shows the two posibilities now involving the flipping of a spin up or down of different energy, leading to two Larmor frequencies. Adapted from Willke *et al.* [17].

where d is the distance between magnetic moments are very weak, which is the perfect scenario for ESR.

Natterer *et al.* [13] study the Larmor frequency of the Fe atom exposed to a constant external magnetic field as the distance to a Ho atom is varied. ESR is so sensitive that it can measure the small shifts of the Larmor frequency as a function of the Ho-Fe distance. Figure 1.3 shows an example of the ESR data as the distance between the two atoms is changed. The ESR peak shifts. When the shifts of the ESR signals are plotted as a fucntion of the interatomic distance, a perfect $1/d^3$ law is retrieved and the magnetic moment for Ho is found to be $(10 \pm 0.1)\mu_B$.

Another example is the determination of the nuclear atomic number of individual atoms. This was done by Willke *et al.* [17]. They measured Fe and Ti atoms on MgO/Ag(001). For Fe, they found the previously shown peak, Fig. 1.3. But sometimes they found a split peak. The value of the splitting perfectly agreed with the known hyperfine interaction of ^{57}Fe. The nuclear spin of ^{57}Fe is $I = 1/2$, explaining why two peaks are found, see Fig. 1.4.

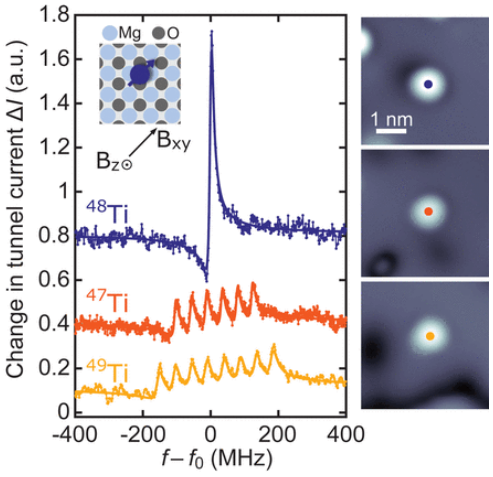

Figure 1.5: The ESR-STM spectra for three different Ti isotopes are shown (^{48}Ti with $I = 0$, ^{47}Ti, with $I = 5/2$ and^{49}Ti with $I = 7/2$). The righ pannel shows constant-current images of the corresponding atoms. Reprinted from Willke *et al.* [17].

The more usual case is ^{56}Fe, which is closed shell and has $I = 0$, leading to no hyperfine interaction. The case of Ti is more interesting. There are three typical isotopes. The more abundant one, ^{48}Ti, has a nuclear spin $I = 0$, and leads to a single ESR peak. See Fig. 1.5. On the same figure, you can also see the spectra for ^{47}Ti, with $I = 5/2$ and consequently 6 peaks, and ^{49}Ti with $I = 7/2$ with 8 peaks as corresponds to the mutliplicity of the nuclear spin.

Recently, pulsed ESR has become available [20]. This is a very interesting development that ushers the STM in the realm of quantum operations. Now, the STM can be used to coherently manipulate local magnetic moments and induce extraordinary operations. New things should be soon discovered.

The above experiments show the interest of the newly developed ESR-STM technique. However, as any other technique, analysis tools need to be developed that permit us to unravel the full potential of this technique.

1.1 Unsolved questions

Despite the success of this new experimental technique, there are still many open questions about the mechanism leading to the all-electric ESR signal. The most prominent question is, how can a magnetic moment respond resonantly to an AC electric field? There is some puzzlement in the community studying ESR-STM, because the associated magnetic field is very small and unable of driving the spin. Therefore, several theoretical proposals have been formulated. Baumann *et al.* conjecture [7] that the AC electric field induces an adiabatic mechanical oscillation of the adatom, leading to a modulation of the crystal field that, together with the atomic spin-orbit interaction, originates spin transitions under very particular symmetry constrains.

A different mechanism could be the phonon excitations induced by the electric field, which efficiently couple to the atomic magnetic moments as described by Chudnovsky and collaborators [21, 22]. This model has been successfully applied to explaining the ESR signal in molecular magnets [8]. Unfortunately, the excitation of unperturbed phonons in MgO/Ag(100) by a driving AC electric field leads to zero spin-phonon coupling. Many other mechanism have been proposed using some variation of the above ideas [23, 24, 25]. However, either these works failed in reproducing strong enough signals or they cannot explain that the ESR resonance can be observed in different atomic species (Fe, Ti, Mn, Cu, and Co) [7, 11, 12, 13, 14, 15, 16, 17][1] with similar Rabi frequencies. Importantly, other surfaces, notably Cu_2N/Cu (001), have failed to yield any ESR signal even though it seems a valid substrate.

The process itself of the Rabi oscillation in ESR is very interesting. The ESR Rabi oscillations can be understood as coherent spin flips. This interpretation brings in more need for modelling because if we take Fe, how a $S_z \approx \pm 2$ Rabi oscillation can take place? The objective of this thesis is to bring some light to these questions and to try to perform quantitative simulations of ESR-STM signals. To his end, we first use computational methods such as Density Functional Theory (DFT) to learn about the overall electronic

[1] Although in the first work on ESR [7], there was not any resonant signal on Co, the authors have confirmed us that it can also be detected.

and magnetic structure of the studied systems. Then, we apply a cotunneling picture to the problem so that we can show that a frequency-dependent DC current can appear as a consequence of the modulation of the tunnel barrier in the STM setup, in the spirit of the Bardeen theory for tunneling current [26]. The resulting spin-electron coupling is similar to the mechanism behind the excitation of molecular vibrations in the inelastic electron tunneling spectroscopy conducted with STM [27, 28]. Finally, we make use of a Floquet approach to develop a simulation tool that produces ESR-STM spectra taking into account the full spin quantum dynamics, the driving electrical field and the electron current reflecting the coherent electron spin oscillations.

Chapter 2

Methods

In this chapter we summarize all the theoretical methods used in the thesis. Because the system is quite complex electronically, we first employed Density Functional Theory (DFT) as a computational method. Although it has serious flaws due to be mainly a mean-field theory, it can provide a good understanding on the main properties of the magnetic impurity with the advantage of not depending on adjustable parameters. An outline of our calculation will be added at the end of this section.

The second method we introduce is the effective time-dependent cotunneling theory. Our aim is to build a cotunneling Hamiltonian which gives an effective total Hamiltonian of the open quantum system (impurity atom plus electrodes) so that we are able to apply the Bloch-Redfield (BRF) formalism [29]. BRF allows us to derive a master equation for the reduced density matrix elements, which results to be quite useful since it provides the general understanding of relaxation and decoherence times, in addition to the Rabi frequency. A multiplet calculation of the atomic electron structure must be applied to achieve proper results. Otherwise, the theoretical calculations lead to inaccurate conclusions.

Finally, we talk about the Floquet-Green's Function technique. This theory tries to provide an easy-to-understand method powerful enough to predict and compute ESR spectra. As in the BRF theory, a low coupling of the impurity atom with the reservoirs is assumed, which is a good approximation for tunneling currents. The theory uses density matrix language to arrive to a master equation that provides a way to compute any observable of interest.

2.1 Electronic Structure Methods

This section of the theory is inspired by two PhD theses [30, 31]. Any quantum system, composed of nuclei and electrons, can be described by the time-dependent Schrödinger equation [32], where the Hamiltonian plays a central role. Solving the Schrödinger equation provides the wavefunction that allows us to extract all important observables of the system. Unfortunately, a full computation of the wavefunctions become impossible for most cases. Hence, several approximations are needed, such as the Born-Oppenheimer one, which separates the motion of the nuclei from the electrons [33]. However, although the nuclear part can be solved using this approximation that reduces the dimension of the problem, the electronic part remains unsolved. The cause of this is the problematic electron-electron interaction of the total Hamiltonian. A possible method to overcome this is the Density Functional Theory (DFT).

2.1.1 Basic DFT formalism, Kohn-Sham (KS) equations. The correlation problem

The idea behind DFT is to not explicitly make use of the many-body electronic wavefunction but instead use the electronic density, $n(\mathbf{r})$, to describe the system [34]. This approach results to be quite versatile and simpler compare to other method such as the Hartree-Fock approximation and, more importantly, less computationally time consuming. In fact, DFT provides a solution of the problem that grows as a power of the number of electrons N, whereas an exact solution of the N-electron Schrödinger equation requires time that grows exponentially with N. The advantage of this method stems from two theorems due to Hohenberg and Kohn [35] (H-K theorems) that we present next. Consider an N-electron system described by the Hamiltonian

$$\hat{\mathcal{H}} = \hat{T} + \hat{V}_{ee} + \hat{V}.$$

$\hat{V}_{ee}$ and $\hat{T}$ are the kinetic and electron-electron interaction terms,

$$\begin{aligned}\hat{V}_{ee} &= \frac{e^2}{2}\sum_{i\neq j}^{N}\frac{1}{|\hat{\mathbf{r}}_i - \hat{\mathbf{r}}_j|}\\ \hat{T} &= \sum_{i=1}^{N}\frac{\hat{\mathbf{p}}_i^2}{2m},\end{aligned}$$

and

$$\hat{V} = \int d^3r V_{ext}(\mathbf{r})\hat{n}(\mathbf{r}),$$

is the potential due to atomic nuclei and external charges, often called external potential. The electron density operator is defined as

$$\hat{n}(\mathbf{r}) = \sum_{i=1}^{N}\delta(\mathbf{r} - \hat{\mathbf{r}}_i), \tag{2.1}$$

being $\hat{\mathbf{r}}_i$ the i-th electron's position operator. The H-K theorems then read as

Theorem 1 *The external potential $\hat{V}_{ext}$ is uniquely determined by the electron density operator $\hat{n}(\mathbf{r})$, apart from a trivial additive constant. Thus, knowing the external potential leads to a fully-determined Hamiltonian.*

Theorem 2 *A universal density functional $E[n]$ for the energy can be defined given the external potential and it is minimized by the exact ground-state electron density.*

Therefore, the ground-state energy is

$$E_{GS} = \min_{n(\mathbf{r})} E[n].$$

The solution lies in performing such minimization. However, this becomes impossible since the exact dependence on the electron density is unknown. Using these theorems, Kohn and Sham [36] proposed to construct the electron density $n(\mathbf{r})$. This leads to a sort of mean-field equations known as the Kohn-Sham (KS) equations whose solutions result to be much simpler and powerful than the Hartree-Fock and more accurate for the ground-state.

In order to derive the KS equations, let us write the energy functional. It can be divided into two parts as follows

$$E[n] = E_0[n] + \int d^3\mathbf{r} V_{ext}(\mathbf{r}) n(\mathbf{r}),$$

where $E_0[n]$ is called the universal functional since it depends on the specific electron-nuclei system implicitly through the electron density. We will write this functional as

$$E_0[n] = E_{kin}[n] + \frac{e^2}{2} \iint \frac{n(\mathbf{r}) n(\mathbf{r}')}{|\mathbf{r} - \mathbf{r}'|} d^3\mathbf{r} d^3\mathbf{r}' + E_{XC}[n].$$

The first term is the kinetic energy of a system of non-interacting particles with the density $n(\mathbf{r})$, which is easy to compute. The second one is the usual Hartree energy and the rest is the exchange, $E_X[n]$, and correlation , $E_C[n]$, energies that take into account the missing electron-electron interaction contributions in the Hartree term. In general, both contributions are not separable and we will refer to them as the exchange-and-correlation functional, $E_{XC}[n]$. At this point, we can apply the second theorem to write

$$\int n(\mathbf{r}') d^3\mathbf{r}' \left(V_{ext}(\mathbf{r}) + e^2 \int \frac{n(\mathbf{r})}{|\mathbf{r} - \mathbf{r}'|} d^3\mathbf{r} + \frac{\delta E_{kin}[n]}{\delta n(\mathbf{r})} + \frac{\delta E_{XC}[n]}{\delta n(\mathbf{r})} \right) = 0, \tag{2.2}$$

These equations for the ground-state density are mean-field like as we mentioned. Thus, we write $n(\mathbf{r}) = \sum_\nu |\phi_\nu(\mathbf{r})|^2$, where the electron density is given by $\phi_\nu(\mathbf{r})$, which are called Kohn-Sham orbitals. The equations for these orbitals can be already extracted from Eq. (2.2):

$$\left(-\frac{\nabla^2}{2m} + V_{ext}(\mathbf{r}) + e^2 \int \frac{n(\mathbf{r})}{|\mathbf{r} - \mathbf{r}'|} d^3\mathbf{r} + V_{XC}(\mathbf{r}) \right) \phi_\nu(\mathbf{r}) = \left(-\frac{\nabla^2}{2m} + V_{eff}(\mathbf{r}) \right) \phi_\nu(\mathbf{r}) = \epsilon_\nu \phi_\nu(\mathbf{r}), \tag{2.3}$$

being ϵ_ν the Lagrange multipliers. Equation (2.3) are the so called Kohn-Sham equations and they have to be solved iteratively.

Notice that KS equations just introduced the concept of a non-interacting reference system built from a set of one-electron orbitals $\phi_\nu(\mathbf{r})$ such that the major part of the kinetic energy, the non interacting one, can be calculated with enough accuracy. The effective field created by the electron-nuclei system minimizes the functional energy where only the exchange

correlation potential $V_{XC}(\mathbf{r})$ is unknown and it has to be approximated. The good news is that the correlation term is usually much smaller than the Hartree and kinetic energies, then we expect that this approximation works well enough. However, many times is not the case and the field of searching for a universal electronic structure method is still opened.

Among of the initial approaches to approximate the exchange and correlation functionals $E_{XC}[n_\uparrow, n_\downarrow]$[1], the local density approximation (LDA) and the generalized gradient approximation (GGA) have become standard. The first one makes use of a uniform-electron-gas model defined by the exchange and correlation functional of a constant electron density. Hence, exchange and correlation energies are local functionals of the electron density and $E_{XC}[n_\uparrow, n_\downarrow]$ can be decomposed linearly into exchange and correlation terms. The exchange part can be approximately computed but the correlation one needs to be parametrized from quantum Monte Carlo simulations [37]. As one would expect from its construction, the LDA is meant to be used for "nearly-homogeneous" electronic systems but surprisingly, it performs very well even in systems where the electronic density changes rapidly.

In order to allow for non-local density variations in the exchange-and-correlation functional, a step beyond is needed. A proposed improvement is the Generalized Gradient Approximation (GGA). To account for the non-homogeneity, the GGA scheme intents to improve LDA by expanding the exchange-correlation energy functional into gradients of the electronic density instead of only using the density at a particular point $\mathbf{r}$. Different parametrizations of GGA have been considered. Among the most spread ones is the Perdew-Burke-Ernzernhof (PBE) [38, 39]. This type of parametrization corrects the LDA exchange term by a multiplicative factor that depends on the density gradients while the correlation part is corrected by a density-dependent additive term. Although GGA tends to "over-correct" LDA, GGA-PBE approximations are accurate enough for most of the electronic structure properties of adsorbed atoms and small molecules on metal sur-

[1]Here we have included spin polarization as a new independent variable that is convenient for many practical calculations, $n = n_\uparrow + n_\downarrow$. DFT theory follows the same principle, now we just need to minimize $E[n_\uparrow, n_\downarrow]$ using the ground state spin-resolved electron densities $n_\uparrow(\mathbf{r})$ and $n_\downarrow(\mathbf{r})$.

faces. However, non-local interactions, such as Van deer Waals forces, have to be explicitly included outside the functional scheme [40].

In order to summarize this section, let us point out the advantages of the DFT method: it offers universality, versatility, simplicity and consumes less computer resources. However, the following considerations have to be taken into account when using the DFT methodology:

- A closed exact form of the density functional is so far unknown, hence it has to be approximated.
- The many-body wavefunction is not accessible. We compute the KS orbitals that are not, by any means, a good approximation to the true wavefunction of the system.
- The universal functional formulation hides the distinguishing characteristics of individual systems. Consideration of simplified models which reveal these characteristics is still needed.
- The theory cannot describe excited electronic states.
- Time-dependent problems require the use of time-dependent density-functional theory (TDDFT). However, the development of approximations for this theory is behind DFT, although, it is progressing [41].

These last two points cause that we cannot apply DFT to the study of ESR, even if the electron density and correlation were available. However, we can extract useful conclusions from DFT.

2.1.2 Outline of our calculation

We have chosen the Vienna Ab initio Simulation Package (VASP) for our impurity calculations which is a DFT computer program for atomic scale materials modelling, e.g. electronic structure calculations and quantum-mechanical molecular dynamics, from first principles. To this end, VASP can compute the solution of the many-body Schrödinger equation using the DFT approach already exposed. Additionally, central quantities, like the one-electron orbitals, the electronic charge density, and the local potential are ex-

pressed in plane wave basis sets. The interactions between the electrons and nucleis are described using either norm-conserving, ultrasoft pseudopotentials, or the projector-augmented-wave, PAW, method which has been demonstrated to be highly accurate [42]. Thus, PAW_PBE potentials will be use in all cases since, as we mentioned, PBE provides a good enough faithfulness for most of the electronic structure properties.

The plane-wave basis set expands all KS orbitals in Fourier components of the reciprocal lattice vector. This implies the use of real-space periodic boundary conditions in order to represent the plane-wave basis set by a discrete set of Fourier components. As a consequence, the systems are faithfully represented by a few atoms in a unit cell that is periodically repeated in space. Attention must be paid to possible interactions between periodic images when simulating very dilute systems or isolated impurities. The Fourier expansion is truncated at large reciprocal vectors. The kinetic energy corresponding to these components is so large that the details of the Hamiltonian are not important and the maximum reciprocal vector can be mapped into a cutoff energy that is used to truncated the Fourier expansion. Since the reciprocal vectors correspond to a small step in space, $G = \frac{2\pi N}{L}$ where N is a large integer number and L is a typical unit cell dimension, the smallest step is $L/2\pi$. This defines the spatial resolution that the plane-wave expansion can achieved. As a consequence, softly varying potentials are numerically better evaluated and this leads to a different types of pseudopotentials to account for the electron-ion interactions. The energy cutoff of the calculation is a crucial parameter that has to be maximized in search of accuracy and reduced in terms of computational efficiency. A second important parameter is the sampling of $\vec{k}$ in the first Brillouin zone in order to abide by Bloch's theorem. Indeed, the use of periodic boundary conditions forces the use of Bloch's theorem to solve Schrödinger's equation. Again the minimum number of k-points, $\vec{k}$, is interesting for computational efficiency albeit detrimental for describing the electron density.

In order to build the surface experimentally used, we first compute the bulk lattice parameters of the MgO crystal structure and Ag FCC following the typical steps of choosing the appropriate cutoff energies and K-points in the range where we expect to find the lattice parameter that minimizes the free energy. Once the bulk lattice parameter is found,

we create a slab of atoms such that one termination is an accurate representation of the experimental surface. It is important to compromise between a large number of atoms to accurately represent the surface and a small number of atoms for faster execution. The unit cell then contains a slab of atoms such that in, say, the z-spatial direction, there are atoms and then vacuum. This is repeated periodically. In the other two directions, the unit cell is chosen such that it patches the surface entirely, effectively representing an infinite system. Van der Waals corrections have to be taken into account by making IVDW= 12 in the INCAR in order to reproduce results closer to the experimental measurements [43]. With the information of the lattice parameter, the next steps to follow are:

- Building the slab of 1-4 monolayers (ML) of MgO over four monolayers of Ag (001), being the Ag atoms under O, and performing three relaxation procedures. Initially we made a first low accuracy calculation, then, we repited it adding a dipole correction setting LDIPOL=.TRUE.[2]. Since the slab is built in the xy plane, IDIPOL= 3. Finally, we performed another relaxation lowering the convergence criterions to the desire value.

- Being the slab relaxed, we placed the Fe impurity in the top MgO layer above one oxygen. In order to take into acount the magnetic behaviour, we have to write in the INCAR file ISPIN= 2 and LDAU = .TRUE. while introducing an on–site Coulomb repulsion U of 3.2 eV, value took from [45]. Then, relaxations are performed lowering the convergence criterions until the system is relaxed enough. The reason to introduce an LDA+U scheme is to correct for the lower magnetization of atoms in the local and semi-local LDA and GGA.

- At this point, we can make calculations for different electric force fields trying to emulate the effect of an electric field in the experiment. Although the field is static, it provides useful information. We compute the Planar Average Potential (PAP) to visually see the difference in the self-consistent electron potential. This potential is the one used to find the KS orbitals and mimics the trapping potential for electrons

[2]The periodic boundary conditions, apart from slowing down the energy convergence with respect to the size of the supercell, affect the potential and the forces by finite size errors. This effect can be counterbalanced by setting LDIPOL=.TRUE. in the INCAR file and it follows the spirit of [44].

in the surface. In the presence of an external electrical field, this potential changes giving us a measurement of the effect of the tip electric field in the potential felt by the surface electrons.

These steps close the Fe on MgO/Ag procedure but, additionally, we built two more surface systems: Cu_2N/Cu and CuCl/Cu. We followed the same previous steps. Both slabs have 4 layers of copper plus a top one where we introduce copper and nitrogen or chlorine. The reason why we study these systems is to compare their electric-field responses with the MgO one since they could provide a better ESR signal. DFT permits us to compute the forces exerted on atoms by virtue of the Hellmann-Feynman theorem. Hence, studying the forces induced in the surface atoms by an external electrical field gives us interesting data on the piezoelectric response of the different system. This is relevant to identify the importance of the surface piezoelectric as a possible mechanism triggering ESR.

2.2 Cotunneling theory approach

Here, we extend the cotunneling formulation of STM-ESR presented in Ref. [46] with some additional details. In our first attempt to simulate the ESR experiments, we used a cotunneling approach where the hybridization with the leads is treated up to second order in perturbation theory. The formalism of time-independent cotunneling provides an effective Hamiltonian of the coupled system that can be introduced into the Bloch-Redfield theory [47]. This theory leads to a markovian master equation for the reduced density matrix.

We recall that the *density matrix* or *density matrix operator* is an alternative way of representing a quantum state instead of using wavefunctions. This formalism, pioneered by J. von Neumann in 1927 [48], presents significant practical advantages since the description becomes especially useful to treat mixed states. A pure quantum state is the one that can be described by a single ket vector while a mixed state is a statistical mixture of pure states without phase relation between the elements of the mixture. Coherent superposition of states gives rise to the so called coherence. These states inevitably arise if we have two or more interacting quantum systems. As a consequence, the density matrix is particularly useful to study open quantum systems. ESR experiments can be thought not only as an open quantum system (the local) interacting with two electronic baths (the two metallic leads of the STM), but this interaction is also *weak*, so the situation is ideal for the application of the perturbative Bloch-Redfield approach.

Therefore, the aim in this section would be to derive a time independent cotunneling Hamiltonian and extend it to the time dependent regime. Then, we will apply the Bloch-Redfield theory and compute transition and decoherence rates, as well as the Rabi frequency.

2.2.1 Effective Cotunneling Hamiltonian

Following A.P. Jahuo *et al.* [49], the total Hamiltonian is described by

$$\hat{\mathcal{H}} = \hat{\mathcal{H}}_{res} + \hat{\mathcal{H}}_S + \hat{\mathcal{H}}_T. \tag{2.4}$$

$\hat{\mathcal{H}}_{res}$ is the Hamiltonian of the $\alpha = L, R$ (left or right) electrode described by

$$\hat{\mathcal{H}}_{res} = \sum_{\alpha k\sigma} (\varepsilon_{\alpha k\sigma} - \mu_\alpha) c^\dagger_{\alpha k\sigma} c_{\alpha k\sigma} = \sum_{\alpha k\sigma} \xi_{\alpha k\sigma} c^\dagger_{\alpha k\sigma} c_{\alpha k\sigma}, \tag{2.5}$$

where the operators $c_{\alpha k\sigma}$ ($c^\dagger_{\alpha k\sigma}$) annihilate (create) electrons in the α-reservoir with a spin projection $\sigma = -1/2, 1/2$ and momentum k. These two reservoirs have temperatures and chemical potentials T_α, μ_α. Notice that for spin unpolarized electrodes, $\xi_{\alpha k\sigma} \equiv \xi_{\alpha k}$. In accordance to Ref. [49], we assume that the occupation of each single particle state $\alpha k\sigma$ is time independent.[3] $\hat{\mathcal{H}}_S$ is the Hamiltonian of the central system which is assumed to be a generalized Anderson model:

$$\hat{\mathcal{H}}_S = \sum_{\ell\sigma} \varepsilon_{\ell,\sigma} \hat{n}_{\ell\sigma} + U \sum_{\ell} \hat{n}_{\ell\uparrow} \hat{n}_{\ell\downarrow} + \frac{1}{2} \sum_{\ell \neq \ell'} \sum_{\sigma,\sigma'} (V_{\ell\ell',\ell'\ell} - V_{\ell\ell',\ell\ell'} \delta_{\sigma\sigma'}) \hat{n}_{\ell\sigma} \hat{n}_{\ell'\sigma'}, \tag{2.6}$$

where $\hat{n}_{\ell\sigma} = d^\dagger_{\ell\sigma} d^\dagger_{\ell\sigma}$ and ℓ indicates the orbital. U is the onsite Coulomb repulsion or charge energy, and $V_{\ell\ell',\ell'\ell}$ and $V_{\ell\ell',\ell\ell'}$ ($\ell \neq \ell'$) are the intersite direct and exchange Coulomb integrals. We assume that this system Hamiltonian is time independent. Hence, only the single-particle energy, $\varepsilon_{\ell,\sigma}(t)$, could be time-dependent. If this is the case, an analysis in terms of Floquet wavefunctions and quasienergies would be required [50]. In the regime of interest, the average charge on the central system is conserved, i.e., $\langle \sum_{\ell,\sigma} \hat{n}_{\ell\sigma} \rangle = N_e$, the total number of electrons. Hamiltonian $\mathcal{H}_S \equiv \mathcal{H}_S(N_e)$ can be then written in the bases of configurations of N_e electrons distributed on the $N_{\rm orb}$ ($N_{\rm orb} = 6$ when only the d-shell of the transition metal atom is considered). This is done by the electronic multiplet calculation developed by F. Delgado. Appendix A includes the bases of the used Multiplet code.

As a result of the coupling to the electrodes, the total charge can fluctuate during very short time periods (virtual processes). Thus, if the coupling to the electrodes is weak enough, only three charge configurations contribute significantly and we can reduce the Hamiltonian in Eq. (2.6) to these 3 charge sectors, $Q = 0, \pm$. The 0 sector is the one corresponding to the ground state of the isolated central system. The sectors + and

[3] The situation of time dependent occupations of the electrodes do not conserve the number of electrons and leads to spurious results.

− correspond to the system with an extra electron and an extra hole respectively. If we denote the instant eigenvectors of the central system as $|Q, n(t)\rangle$, the central part Hamiltonian can be approximately diagonalized as

$$\hat{\mathcal{H}}_S(t) \approx \sum_{Q=0,\pm} \sum_{n} E_{Q,n}(t)|Q, n(t)\rangle\langle Q, n(t)|.$$

The tunneling Hamiltonian, $\hat{\mathcal{H}}_T(t)$, represents the coupling between the reservoirs and the central system represented by $\hat{\mathcal{H}}_S$. It changes the number of electrons in the correlated quantum system by one unit to create or annihilate one in the reservoirs:

$$\hat{\mathcal{H}}_T = \sum_{\alpha k\sigma,\mathbf{i}} \left[V_{\alpha k\sigma,\mathbf{i}}(t) c^{\dagger}_{\alpha k\sigma} d_{\mathbf{i}} + V^{*}_{\alpha k\sigma,\mathbf{i}}(t) d^{\dagger}_{\mathbf{i}} c_{\alpha k\sigma} \right] = \hat{\mathcal{V}}^{(-)}(t) + \hat{\mathcal{V}}^{(+)}(t), \tag{2.7}$$

where $d^{\dagger}_{\mathbf{i}}$ creates an electron with quantum numbers $\mathbf{i} = (\ell, \sigma)$ with ℓ the orbital number and σ the spin. The spin conservation imposes that the hopping $V_{\alpha k\sigma,i\sigma'}$ are zero if $\sigma \neq \sigma'$. In Eq. (2.7) we have introduced the operators $\hat{\mathcal{V}}^{(\pm)}$, the tunneling part that increases (+) or decreases (−) the number of electrons in the central region by one unit. Notice that we have a time dependent hopping parameter.

We would like to call the attention on one detail of our system's description. In principle, we have two ways of introducing the effect of the AC voltage discussed in section 1.1: *linear energy shift* or *time-dependent tunneling* $V_{\alpha k,\sigma}$. The first acts on the single-particle energy $\varepsilon_{\ell,\sigma}(t)$ while the second one on the tunneling constant or hopping. Later on this thesis we will conclude from DFT calculations that, for the STM-ESR experiments on MgO, only the time-dependent tunneling can provide a strong enough ESR effect. So, the linear energy shift is discarded. We will talk about this in the next section. We shall start by computing a time-independent cotunneling which will allow us to introduce an effective total Hamiltonian.

The essence of *cotunneling theory* is that the central system is weakly coupled to the reservoirs. Therefore, the transport of the tunneling Hamiltonian can be treated by second order pertubation theory. Furthermore, the average occupation of the charge states $Q = \pm$ remain constant. So we can use degenerate perturbation theory to determine the dynamics of the states acting only on the N_0-charge space, which hereafter we shall refer as *neutral*

charge state. We define the eigenvectos and eigenvalues of the decoupled electrode+central system having N_0 electrons on the central part as $|N\rangle$ and E_N, respectively. We denote by $|M_\pm\rangle$ the corresponding eigenvectors with $N_0 \pm 1$ electron. Hence, we can write the matrix elements between states $|N\rangle$ and $|N'\rangle$ as

$$H^{\text{eff}}_{N,N'} = \sum_M \frac{\langle N|\hat{\mathcal{H}}_T|M\rangle\langle M|\hat{\mathcal{H}}_T|N'\rangle}{E_M - E_0}.$$

E_0 is the ground state energy of the (decoupled) system with N_0 electrons in the central region. Since the tunneling Hamiltonian changes the charge state of the central system by one unit, the matrix elements $\langle N|H_{\text{tun}}|N\rangle$ vanish, so we can write

$$H^{\text{eff}}_{N,N'} = \sum_{M_-} \frac{\langle N|\hat{\mathcal{V}}^+|M_-\rangle\langle M_-|\hat{\mathcal{V}}^-|N'\rangle}{E_{M_-} - E_0} + \sum_{M_+} \frac{\langle N|\hat{\mathcal{V}}^-|M_+\rangle\langle M_+|\hat{\mathcal{V}}^+|N'\rangle}{E_{M_+} - E_0}, \tag{2.8}$$

which is defined in the neutral charge subspace $Q = 0$. We now write the low energy eigenstates of $\hat{\mathcal{H}}_0 = \hat{\mathcal{H}}_S + \hat{\mathcal{H}}_{\text{res}}$. First, let us consider the neutral charge sector states

$$|N\rangle = |n\rangle \otimes |\Psi_f(0)\rangle, \tag{2.9}$$

where $|\Psi_f\rangle$ is a multi electronic Slater describing independent Fermi seas of left and right electrodes and $|n\rangle$ is the eigenvector of the isolated central quantum system. These states can describe both the *ground state* and states with an *electron-hole pair* in the electrodes and an excited state n' in the central system. Notice that the electron-hole pair can be either in one electrode or split in the left and right electrodes. In the second case this excitation contributes to the net current flow. The energy difference $E_{N'}$ and E_N can be arbitrarily small, and definitely much smaller than $E_M - E_N$. From Eq. 2.9, one can separate the neutral charge energies into central system and electrode contributions:

$$E_{N'} - E_N = \epsilon_{\alpha'} - \epsilon_\alpha + E_{n'} - E_n.$$

The excited states $Q = \pm$ read as

$$|M_\pm\rangle = |m_\pm\rangle \otimes |\Psi_{mf}(\mp)\rangle.$$

Here $|\Psi_f(\mp)\rangle$ is a Slater state for the electrodes with one electron more (+) or less (−) than the N manifold. $|m_\pm\rangle$ has a similar meaning to $|n\rangle$, but now for the uncoupled charge excited states. Roughly speaking, the cotunneling approach will remain valid as long as

$$\left|\frac{\langle N|\mathcal{V}^\pm|M_\mp\rangle}{E_{M_\mp}-E_N}\right| \ll 1.$$

So we are now in position of rephrasing the original problem described by the Hamiltonian $\hat{\mathcal{H}}$ in Eq.(2.4) and write an effective Hamiltonian that can be introduced in the Bloch-Redfield master equation. Within the cotunneling theory, it is equivalent to studying the dynamics of the much simpler Hamiltonian

$$\hat{\mathcal{H}}^{\text{eff}} \equiv \hat{\mathcal{H}}_{\text{res}} + \hat{\mathcal{H}}_S + \hat{\mathcal{H}}_T^{\text{eff}} \tag{2.10}$$

where

$$\hat{\mathcal{H}}_T^{\text{eff}} = \sum_M \frac{\hat{\mathcal{H}}_T|M\rangle\langle M|\hat{\mathcal{H}}_T}{E_M-E_0} = \sum_{M_-} \frac{\hat{\mathcal{V}}^+|M_-\rangle\langle M_-|\hat{\mathcal{V}}^-}{E_{M_-}-E_0} + \sum_{M_+} \frac{\hat{\mathcal{V}}^-|M_+\rangle\langle M_+|\hat{\mathcal{V}}^+}{E_{M_+}-E_0}. \tag{2.11}$$

Our final objective is to write the total Hamiltonian as a term corresponding to the reservoirs, which is already $\hat{\mathcal{H}}_{\text{res}}$, a term $\hat{\mathcal{H}}'_C$ that corresponds to the central system defined only on the neutral charge Hilbert space, and a coupling term $\hat{\mathcal{H}}'_{\text{cotun}}$. In addition, these terms should satisfy the following conditions in order to applied the BRF equations:

i) The interaction should have a null average value, i.e, $\text{Tr}_{\text{res}}\left[\hat{\rho}_{\text{res}}\hat{\mathcal{H}}'_{\text{cotun}}\right] = 0$, with $\text{Tr}_{\text{res}}[\cdots]$ indicating the trace over the reservoir degrees of freedom.

ii) The interaction $\hat{\mathcal{H}}'_{\text{cotun}}$ should have the form $\sum_j S^j R^j$, where S^j is some function of system operators and R^j a function of the reservoir operators.

Let us now focus on evaluating the matrix elements in Eq. (2.11). It is convenient to write down the explicit form of the electrodes wavefunctions. If we denote by $|0\rangle$ the ground state of the electrodes in the Fermi sea with no excitations in the neutral charge state, we can write $|\Psi\rangle \equiv c_\eta^\dagger c_\eta|0\rangle$, where we are creating an electron-hole pair with quantum number $\eta = \{\alpha, k, \sigma\}$. For the states with one electron excess (defect) we will have $|\Psi_-\rangle = c_\beta c_\eta^\dagger c_\eta|0\rangle$ and $|\Psi_+\rangle = c_{\beta'}^\dagger c_\eta^\dagger c_\eta|0\rangle$. The zero-temperature occupation of an electrode state η is then given by $n_\eta = \langle\Psi|c_\eta^\dagger c_\eta|\Psi\rangle$, which can only take the values 0 or 1 for electrons.

The matrix element of the electrode operator in Eq. (2.11) selects only one term in the electrode part of the sums $\sum_{M_\pm} = \sum_{m_\pm} \sum_{\Psi_\mp}$. Then one can write

$$\sum_{\Psi_+} \langle \Psi | c_\gamma | \Psi_+ \rangle = (1 - n_\gamma)\delta_{\beta\gamma}, \quad \sum_{\Psi_-} \langle \Psi | c_\gamma^\dagger | \Psi_- \rangle = n_\gamma \delta_{\beta\gamma}.$$

Making the corresponding substitution into Eq. (2.11) we get

$$\sum_{M_-} \frac{\langle N|\hat{\mathcal{V}}^+|M_-\rangle\langle M_-|\hat{\mathcal{V}}^-|N'\rangle}{E_{M_-} - E_0} = \sum_{\eta\eta'} \left(1 - n_\eta\right) \langle n|\hat{T}_-(\eta\eta')|n'\rangle\langle\Psi|c_\eta c_{\eta'}^\dagger|\Psi\rangle, \tag{2.12}$$

and

$$\sum_{M_+} \frac{\langle N|\hat{\mathcal{V}}^-|M_+\rangle\langle M_+|\hat{\mathcal{V}}^+|N'\rangle}{E_{M_+} - E_0} = \sum_{\eta\eta'} n_\eta \langle n|\hat{T}_+(\eta\eta')|n'\rangle\langle\Psi|c_\eta^\dagger c_{\eta'}|\Psi\rangle, \tag{2.13}$$

where we have introduced the transition amplitude operators $\hat{T}_\pm(\eta\eta')$ given by

$$\hat{T}_-(\eta\eta') = \sum_{m_-,\ell\ell'} \frac{V_{\eta,\ell}^* V_{\eta',\ell'}}{E_{m_-} - E_0 + \epsilon_\eta} d_{\ell\sigma}^\dagger |m_-\rangle\langle m_-| d_{\ell'\sigma} \tag{2.14}$$

$$\hat{T}_+(\eta\eta') = \sum_{m_+,\ell\ell'} \frac{V_{\eta,\ell} V_{\eta',\ell'}^*}{E_{m_+} - E_0 - \epsilon_\eta} d_{\ell\sigma} |m_+\rangle\langle m_+| d_{\ell'\sigma}^\dagger. \tag{2.15}$$

$\hat{T}_\pm(\eta\eta')$ correspond to virtual transition operators. The first one acts on the $Q = -$ charge manifold while the second one on the $Q = +$. Equations (2.12,2.13) can be simplified by taking into account that $\sum_{\eta,\eta'} n_\eta \langle\Psi|c_\eta c_{\eta'}^\dagger|\Psi\rangle = \langle\Psi| \sum_{\eta\eta'} c_\eta c_{\eta'}^\dagger|\Psi\rangle$. Hence, when we restrict the reservoir states to single electron-hole pairs $|\Psi\rangle$, we can write

$$\hat{\mathcal{H}}_T^{\text{eff}}(t) \approx \sum_{\eta\eta'} \left[\hat{T}_+(\eta\eta';t) c_\eta^\dagger c_{\eta'} + \hat{T}_-(\eta\eta';t) c_\eta c_{\eta'}^\dagger\right] \tag{2.16}$$

It is convenient to rewrite the effective tunneling Hamiltonian (2.16) using $c_\eta^\dagger c_{\eta'} + c_\eta c_{\eta'}^\dagger = \delta_{\eta,\eta'}$ so that we have

$$\hat{\mathcal{H}}_T^{\text{eff}} \approx \sum_{\eta\eta'} \left[\hat{T}_+(\eta\eta';t) - \hat{T}_-(\eta\eta';t)\right] c_\eta^\dagger c_{\eta'} + \sum_\eta \hat{T}_-(\eta\eta;t)$$

The last term is proportional to the identity in the electrode degrees of freedom so it will renormalize the energy spectra of $\hat{\mathcal{H}}_S$.

Thus, we can define a tunneling Hamiltonian as follows

$$\hat{\mathcal{H}}_{cotun} \approx \sum_{\eta\eta'} \left[\hat{T}_+(\eta\eta') - \hat{T}_-(\eta\eta')\right] c_\eta^\dagger c_{\eta'}. \tag{2.17}$$

$\hat{\mathcal{H}}_{cotun}$ has the desired form of a product between central-system and bath operators (condition ii) above. However, it does not satisfy condition i) since, in general, the trace over the reservoir degrees of freedom of this tunneling Hamiltonian is nonzero. As a consequence, we need to make an additional step in order to apply a Bloch-Redfield (BRF) master equation. We then define the total system electrodes plus central system Hamiltonian as

$$\hat{\mathcal{H}}^{\text{eff}} = \hat{\mathcal{H}}_{res} + \hat{\mathcal{H}}'_S + \hat{\mathcal{H}}'_{cotun}.$$

where

$$\hat{\mathcal{H}}'_S = \hat{\mathcal{H}}_S + \sum_\eta \left[\hat{T}_+(\eta\eta)n_\eta + \hat{T}_-(\eta\eta)(1-n_\eta)\right] \tag{2.18}$$

and

$$\hat{\mathcal{H}}'_{cotun} = \hat{\mathcal{H}}_{cotun} - \sum_\eta \left[\hat{T}_+(\eta\eta) - \hat{T}_-(\eta\eta)\right] n_\eta \tag{2.19}$$

with $n_\eta = 0, 1$ the occupation of the single particle state η. We only subtracted and added the same quantity to the Hamiltonians so that, by construction, $\mathrm{Tr}_{\text{res}}(\hat{\rho}_{\text{res}}\hat{\mathcal{H}}'_{cotunn}) = 0$. This step is necessary since the master equation description for the reduced density matrix requires that the only effect of the reservoir is to produce fluctuations around a zero expectation value of the interaction. Another consideration regarding the validity of Bloch-Redfield master equation that usually is based on the *secular approximation* with respect to the system-environment coupling. The physical condition underlying this approximation is that the systematic evolution of the reduced system is fast, which means that the coherent dynamics goes through many cycles during the typical relaxation time [47].

Within the BRF master equation, the markovian evolution of the reduced density matrix can be written as:

$$\partial_t \rho_{lj}(t) = -i\omega_{lj}\rho_{lj}(t) + \sum_{ll'}{}' \mathcal{R}_{lj,l'j'}\rho_{l'j'}(t), \tag{2.20}$$

where $\omega_{lj} = (E_l - E_j)/\hbar$ and $\mathcal{R}_{lj,l'j'}$ is the Bloch-Redfield tensor, which depends both on the matrix elements of the system operators related to the virtual transitions as well as on the reservoir operator correlator [29]. From the hermiticity of the density matrix, one gets $\mathcal{R}^*_{lj,l'j'} = \mathcal{R}_{lj,l'j'}$. The prime over the sum in Eq. (2.20) implies that only the terms whose energies satisfy $|\omega_{lj} - \omega_{l'j'}| \ll 1/\delta t$ are included, where $\delta t = \hbar/(k_B T)$ is the coarse-grain time scale under which the evolution of the reduced density matrix is described. This is the so called *secular aproximation* [51]. We can distinguish the following processes according to the four indexes of the BRF tensor

1. ll, ll: Negative total transition rate from the l-state to any other possible state of $\hat{\mathcal{H}}'_S$
2. lj, lj: Negative decoherence rate of the coherence ρ_{lj} coherence. It has two contributions: a pure dephasing one and another associated with population scattering.
3. ll, jj: Population transfer: rate of population transfer from state j to state l state ($l \neq j$).
4. $lj, l'j'$: Coherence transfer: rate at which amplitude in an oscillating superposition between two states (l' and j') couples to form oscillating amplitude between two other states (l and j).

The last contribution can be relevant in the case of degenerate energy levels. Otherwise, it is cut out by the secular approximation. The first and the third contributions are computed by the Fermi's golden rule and related to T_1-like processes while the second contribution is related to coherence times [52].

2.2.2 Rabi flop rate from a time dependent cotunneling theory

A two level system approach

As we have seen, the dissipative dynamics of quantum systems weakly coupled to the environment in the absence of a driving field is well described by the perturbative Bloch-Redfield (BRF) master equation. A non-formal approximate evolution of the reduced density matrix $\hat{\rho}(t)$ describing the quantum system in the presence of an AC driving field can be given in the form of a Bloch equation presented in [29, 51]. In this case, $\hat{\rho}(t)$ satisfies

the following Liouville's equation,

$$\frac{d\hat{\rho}(t)}{dt} = -\frac{i}{\hbar}\left[\hat{\mathcal{H}}_S(t), \hat{\rho}(t)\right] + \hat{\mathcal{L}}\hat{\rho}(t), \tag{2.21}$$

where $\hat{\mathcal{L}}$ will take the form of a linear Lindblad super-operator [47]. $\hat{\mathcal{L}}\hat{\rho}(t)$ is responsible for dissipation and thus, decoherence and relaxation. The crucial approximation leading to the Bloch equation is to assume that the Lindblad super-operator is not affected by the driving field, so it is exactly the Bloch-Redfield tensor term of Eq. (2.20). In the case of a TLS, the general form of a system Hamiltonian with driven-transition is

$$\hat{\mathcal{H}}_S^{\mathrm{TLS}}(t) = \begin{pmatrix} E_a & \hbar\Omega\cos(\omega t) \\ \hbar\Omega\cos(\omega t) & E_b \end{pmatrix}, \tag{2.22}$$

where Ω is known as *Rabi frequency* or *Rabi flop rate*. This method will be adequate to describe weak fast-oscillating driving fields [53, 54]. The diagonal terms are the energy levels of the two states, $|a\rangle$ and $|b\rangle$, and the off-diagonal term is the coupling between them. The coupling in a static two-level system is given by the Rabi flop-rate Ω, see for example Ref. [51]. In the present case, the AC driving field leads to a modulation of the coupling with linear frequency $\omega/2\pi$. Defining the lifetime time $T_1 = 1/(\Gamma_{ab} + \Gamma_{ba})$ and the decoherence time $T_2 = 1/\gamma_{ab}$, being the transition and decoherence (lost of coherence) rates Γ_{ab} and γ_{ab} respectively, the dynamical equation of motion for the reduced density matrix of the effective TLS reads as:

$$\dot{\rho}_{aa} = -\dot{\rho}_{bb} = \frac{1}{2T_1}(\rho_{bb} - \rho_{aa} - P_b^{eq} + P_a^{eq}) + i\Omega(\rho_{ab} - \rho_{ba})\cos\omega t \tag{2.23}$$

$$\dot{\rho}_{ab} = \dot{\rho}_{ba}^{*} = -\frac{1}{T_2}\rho_{ab} + i\omega_{ba}\rho_{ab} - i\Omega(\rho_{bb} - \rho_{aa})\cos\omega t. \tag{2.24}$$

Hence, relaxation is associated to the decay of any departure of the diagonal elements (populations) from the equilibrium on a time scale T_1, while the decoherence corresponds to the decay of the off-diagonal terms on a time scale T_2. P_b^{eq} and P_a^{eq} are the equilibrium populations when the Rabi term is zero.

In all STM-ESR experiments [7, 11, 12, 13, 14, 15, 16, 17], the detection frequency bandwidth is around 1 kHz, so the driving AC voltage, modulated on the GHz frequency range, is

averaged out. Thus, the resonant signal is detected only by the magnetoresistive static current. The resulting DC current can be evaluated in terms of the transition rates $\Gamma_{ab}^{\alpha\alpha'}$ ($\alpha \neq \alpha'$) between the α and α' electrodes (T tip and S substrate) and the non-equilibrium occupations $P_n(V,\omega)$:

$$I(V,\omega) = e\sum_{nm} P_n(V,\omega)\left(\Gamma_{n,m}^{T,S} - \Gamma_{n,m}^{S,T}\right). \tag{2.25}$$

Counting n and m for the states $|a\rangle$ and $|b\rangle$. Here, the non-equilibrium occupations $P_n(V,\omega)$ will be the result of a long-time average stationary condition $d\hat{\rho}(t)/dt = 0$ that defines the steady state, and it accounts for the coherence between the $|a\rangle$ and $|b\rangle$ states connected by the ESR signal. In Eq. (2.25) we did not account for the explicit coherences contribution to the DC current since, in general, these terms are much smaller. This will be confirmed later by our Floquet analysis. Although there is not a general analytical expression for $P_n(V,\omega)$, one can find an explicit expression for the TLS solving the steady state version of Eqs. (2.23) and (2.24),

$$\begin{aligned} 0 &= \frac{1}{2T_1}(P_b(V,\omega) - P_a(V,\omega) - P_b^{eq} + P_a^{eq}) + \frac{i}{2}\omega(c - c^*) \\ i\omega c &= -\frac{1}{T_2}c + i\omega_{ba}c - \frac{i}{2}\omega(P_b(V,\omega) - P_a(V,\omega)), \end{aligned}$$

where we have applied the rotating-wave approximation (RWA) to neglect the fast-oscillating exponentials $\exp(\pm 2i\omega t)$. The constant c comes from making $\rho_{ab}(t) = ce^{i\omega t}$. Thus

$$P_b(V,\omega) - P_a(V,\omega) = -\delta P^{eq}\left[1 + \frac{\Omega^2 T_1 T_2}{1 + \Omega^2 T_1 T_2 + (\omega - \omega_{ba})^2 T_2^2}\right], \tag{2.26}$$

where $\delta P^{eq} = \tanh(\hbar\omega_{ba}/2k_BT)$. It is worth noticing that the solution (2.26) can be recasted in the form of the macroscopic Bloch equations describing the evolution of a magnetic moment in the presence of both a static and a driving magnetic field [55]. Equation (2.25) makes explicit the working mechanism of the STM-ESR: the occupations $P_n(V,\omega)$ respond to the driving frequency and the changes are reflected in the DC current $I(V,\omega)$. Notice that the Rabi frequency dictates the response of the system to the driving field and thus, if the system is ESR active. Therefore, the next step would be to evaluate the Rabi frequency predicted by our cotunneling description.

Time dependent cotunneling

Our aim now is to derive the Rabi frequency from a time dependent cotunneling theory. We first remind that the Bloch-Redfield master equation (2.21) assumes that the interaction $\hat{\mathcal{H}}'_{cotun}$ with the reservoirs only induces fluctuations around a zero-average, i.e., $\mathrm{tr}_R[\hat{\rho}_R\hat{\mathcal{H}}'_{cotun}] = 0$. It is precisely this condition that leads to our definition of $\hat{\mathcal{H}}'_{cotun}$ given by Eq. (2.19) and to a *dressed* Hamiltonian (2.18). For notation clarity, we omit the primes and, unless otherwise stated, we will refer to the renormalized Hamiltonians.

To explore the origin of the ESR signal in the experiments, we concentrate on the Rabi frequency. In particular, we focus on the situation where the driving frequency ω is close to the Bohr frequency of the transition between the first excited state, $|b\rangle$, and the ground state, $|a\rangle$, $\omega_{ba} = (E_b - E_a)/\hbar$, while all other transitions are far away.

We follow the same procedure leading to the Bloch equations, but now we consider that the system Hamiltonian $\hat{\mathcal{H}}_S$ has an arbitrary number of states. Hence, we define static and driving parts, $\hat{\mathcal{H}}_S(t) = \hat{\mathcal{H}}_S^0 + \delta\hat{\mathcal{H}}_S\cos(\omega t)$ generalizing the two-level case of Eq. (2.22). Using a similar notation, we write the time-dependent interaction as $\hat{\mathcal{H}}_{cotun}(t) \equiv \hat{\mathcal{H}}^0_{cotun} + \delta\hat{\mathcal{H}}_{cotun}\cos(\omega t)$. Since the Rabi flop-rate is defined by the off-diagonal matrix elements of $\hat{\mathcal{H}}_S(t)$, following Eqs. (2.22) and (2.18), we can write it as

$$\hbar\Omega = \sum_{\eta}\left[\delta\hat{T}^{+}_{ab}(\eta\eta)n_\eta + \delta\hat{T}^{-}_{ab}(\eta\eta)(1-n_\eta)\right] + \langle a|\delta\hat{\mathcal{H}}_S|b\rangle, \tag{2.27}$$

where $\delta\hat{T}^{\pm}_{ab}(\eta\eta) = \langle a|\delta\hat{T}_{\pm}(\eta\eta)|b\rangle$, with the driving part of the virtual transition operators defined as $\delta\hat{T}_{\pm}(\eta\eta)\cos(\omega t) = \delta\hat{T}_{\pm}(\eta\eta;t) - \hat{T}^{(0)}_{\pm}(\eta\eta)$. Notice that we have taken into account that $|a\rangle$ and $|b\rangle$ are eigenvectors of the static part of $\hat{\mathcal{H}}'_S$, see Eq. (2.18).

The driving electric field produced by the AC voltage can be translated, in principle, into two effects. First, a *time dependence of the adatom's energy levels*, similar to a Stark energy shift of the d-shell. These shifts will affect the charging energies appearing in the denominators of the virtual transition operators

$$E_{m_\pm}(t) - E_0(t) \approx E_{m_\pm} - E_0 \mp A\cos(\omega t).$$

where A is proportional to V_{AC}. Since $|E_{m_\pm} - E_0| \gg |eV_{ac}|$, we can use a Taylor expansion of the denominators and write

$$\hat{T}_\pm(\eta\eta;t) \approx \hat{T}_\pm(\eta\eta)\Big|_{V_{ac}=0} + \delta\hat{T}^{\mathrm{S}}_-(\eta\eta)\cos\omega t, \tag{2.28}$$

where $\hat{T}_-(\eta\eta')\Big|_{V_{AC}=0}$ are the virtual transition operators in the absence of the AC field. Here S denotes the modulation of the virtual transition operators by Stark-like shift. Using Eqs. (2.14) and (2.15), the harmonic driving field contributions reads as:

$$\begin{aligned}
\delta\hat{T}^{\mathrm{S}}_-(\eta\eta) &\approx -A\sum_{\mathbf{i}\mathbf{i}',m_-}\frac{V^*_{\eta,\mathbf{i}}V_{\eta,\mathbf{i}'}}{\left(E_{m_-}-E_0+\epsilon_\eta\right)^2}d^\dagger_{\mathbf{i}}|m_-\rangle\langle m_-|d_{\mathbf{i}'}\\
\delta\hat{T}^{\mathrm{S}}_+(\eta\eta) &\approx +A\sum_{m_+,\mathbf{i}\mathbf{i}'}\frac{V_{\eta,\mathbf{i}}V^*_{\eta,\mathbf{i}'}}{\left(E_{m_+}-E_0-\epsilon_\eta\right)^2}d_{\mathbf{i}}|m_+\rangle\langle m_+|d^\dagger_{\mathbf{i}'}.
\end{aligned} \tag{2.29}$$

As we have mentioned before, our density functional theory calculations for the Fe on MgO/Ag(001) system show that the adatom's level shifts are negligible under the typical external electric fields induced at the STM junction, see results section 3.1. Then, we assume that the adatom Hamiltonian is not affected by the AC driving field, leading to $\delta\hat{\mathcal{H}}_S = 0$ and a coefficient $A = 0$ in Eq. (2.29). This implies the prevalence of the second mechanism, the modulation of the tunnel barrier through the matrix elements $V_{\eta,\mathbf{i}}(t)$ [27, 28]. Thus, taking into account that the resulting modulation is also much smaller than the amplitude of these hoppings, we can make a Taylor expansion similar to Eq. (2.28) where the new corrections are given by

$$\begin{aligned}
\delta\hat{T}^{\mathrm{B}}_-(\eta\eta) &\approx -B\sum_{\mathbf{i}\mathbf{i}',m_-}\frac{(\delta V^*_{\eta,\mathbf{i}}V_{\eta,\mathbf{i}'}+)V^*_{\eta,\mathbf{i}}\delta V_{\eta,\mathbf{i}'}}{\left(E_{m_-}-E_0+\epsilon_\eta\right)}d^\dagger_{\mathbf{i}}|m_-\rangle\langle m_-|d_{\mathbf{i}'}\\
\delta\hat{T}^{\mathrm{B}}_+(\eta\eta) &\approx +B\sum_{m_+,\mathbf{i}\mathbf{i}'}\frac{\delta V_{\eta,\mathbf{i}}V^*_{\eta,\mathbf{i}'}+V_{\eta,\mathbf{i}}\delta V^*_{\eta,\mathbf{i}'}}{\left(E_{m_+}-E_0-\epsilon_\eta\right)}d_{\mathbf{i}}|m_+\rangle\langle m_+|d^\dagger_{\mathbf{i}'},
\end{aligned} \tag{2.30}$$

with B proportional to V_{AC} and depends on the elastic barrier transmission. B indicates virtual transitions associated to the barrier modulation.

We model the effect of the AC driving field on the tunneling amplitudes based on the Bardeen analysis. In doing so, we assume that the STM junction can be treated as a square vacuum barrier of length L and energy height E, and that the tip and sample have the

same work functions. The AC applied voltage leads to a time-dependent change of the transmission amplitude which, for small-enough bias, can be approximated as

$$V_{\eta,\mathbf{i}}(t) \approx V^0_{\eta,\mathbf{i}}\left(1 + e\frac{V_{AC}}{|\delta_{ab}|}\cos(\omega t)\right). \tag{2.31}$$

We follow a WKB description introducing the wavenumbers $k = \sqrt{2m^*\epsilon}/\hbar$ and $\kappa = \sqrt{2m^*(E-\epsilon)}/\hbar$, being $\kappa L \gg 1$. Notice that $E - \epsilon_F$ is basically the metal work function. Considering this, one finds [56]

$$\delta^{-1}_{ab} \approx \frac{m^*\left(k_F(1 - L\kappa_F) - iL\kappa_F^2\right)}{\hbar^2\kappa_F^2(k_F + i\kappa_F)}. \tag{2.32}$$

Here we have assumed that k and κ can be approximated by their values at the Fermi level. This is adequate to describe the tunneling current under the experimental low bias conditions. Having already Eqs. (2.31) and (2.32), the next step would be to compute how the virtual transition changes. From Eqs. (2.30) and (2.31) we can write

$$\begin{aligned}
\delta\hat{T}_-(\eta\eta;t) &= \frac{2eV_{ac}}{|\delta_{ab}|}\sum_{m_-,\ell\ell'\sigma}\frac{V^{0*}_{\eta,\ell\sigma}V^0_{\eta,\ell'\sigma}}{\Delta E_{m_-} - \mu_- + \epsilon_\eta}d^\dagger_{\ell\sigma}|m_-\rangle\langle m_-|d_{\ell'\sigma} \\
\delta\hat{T}_+(\eta\eta;t) &= \frac{2eV_{ac}}{|\delta_{ab}|}\sum_{m_+,\ell\ell'\sigma}\frac{V^{0}_{\eta,\ell\sigma}V^{0*}_{\eta,\ell'\sigma}}{\Delta E_{m_+} + \mu_+ - \epsilon_\eta}d_{\ell\sigma}|m_+\rangle\langle m_+|d^\dagger_{\ell'\sigma}.
\end{aligned}$$

where we kept only first order terms in the AC driving voltage. The Rabi flop-rate can be evaluated using these equations and Eq. (2.27). Then we have that

$$\begin{aligned}
\Omega \approx \frac{eV_{AC}}{\hbar|\delta_{ab}|}\sum_\eta\Bigg[&\sum_{m_-,\ell\ell'\sigma}(1 - n_F(\epsilon_\eta))\frac{2V^{0*}_{\eta,\ell\sigma}V^0_{\eta,\ell'\sigma}}{\Delta E_{m_-} - \mu_- + \epsilon_\eta}\gamma^{m^-}_{ab}(\ell\sigma,\ell'\sigma) + \\
&\sum_{m_+,\ell\ell'\sigma} n_F(\epsilon_\eta)\frac{2V^{0}_{\eta,\ell\sigma}V^{0*}_{\eta,\ell'\sigma}}{\Delta E_{m_+} + \mu_+ - \epsilon_\eta}\gamma^{m^+}_{ab}(\ell\sigma,\ell'\sigma)\Bigg],
\end{aligned} \tag{2.33}$$

where we have introduced the excitation energies $\Delta E_{m^\pm} = E_{m^\pm} - E_{0^\pm}$ and the charging energies of the adatom $\mu_+ = E_{0^+} - E_0$ and $\mu_- = E_0 - E_{0^-}$. Moreover, we have defined the Fermi-Dirac distribution

$$n_F(\epsilon) = \frac{1}{e^{(\epsilon - E_{f_\alpha})/k_BT_\alpha} + 1},$$

being E_{f_α} the chemical potential of the α electrode. In addition, we have written the matrix elements $\gamma_{ab}^{m^-}(\ell\sigma,\ell'\sigma) = \langle a|d_{\ell\sigma}^\dagger|m_-\rangle\langle m_-|d_{\ell'\sigma}|b\rangle$ and $\gamma_{ab}^{m^+}(\ell\sigma,\ell'\sigma) = \langle a|d_{\ell\sigma}|m_+\rangle\langle m_+|d_{\ell'\sigma}^\dagger|b\rangle$. Notice that, contrary to what happens in the calculation of transition and decoherence rates [57, 29] where all energy integrals involve the product $n_F(1-n_F)$, here the energies ϵ_η are not limited to a small energy window around the Fermi level. Thus, the evaluation of the Rabi frequency requires a precise knowledge of the hybridization functions $V_{\eta,\ell\sigma}$.

However, there are a few strategies to make the calculation a bit simpler. First, we consider Born-von Karman periodic boundary conditions of length L and we introduce the density of states $\rho_{\alpha\sigma}(\epsilon) = \sum_{\vec{k}} \delta(\epsilon - \epsilon_{\alpha k\sigma})$. Thus, we can write the sum over the electrodes wavenumbers as $\sum_{\vec{k}} \to \frac{L^d}{(2\pi)^d}\int dk^d \equiv \int_{-\infty}^{+\infty} d\epsilon \rho_{\alpha\sigma}(\epsilon)$, where d indicates the dimensions of the electronic problem, which is one for the one impurity problem.

i) The density of states is constant within an energy window $[-E_c, E_c]$ and equal to its value at the Fermi level.

ii) The hybridizations $V_{\eta,\ell} = V_{\alpha,\ell\sigma}$ are constant within the energy cut-off E_c and equal to their value at the Fermi level.

iii) Only the tip is spin polarized, being the spin polarization P_T constant throughout the whole energy range. Thus, we can write (we omit the subindex "F" indicating values taken at the Fermi level): $\Gamma_{\alpha,\ell\ell'\sigma} = 2\pi(1/2 + \sigma P_\alpha)\rho_\alpha V_{\alpha,\ell\sigma}V^*_{\alpha,\ell'\sigma} = (1/2+\sigma P_\alpha)\Gamma'_{\alpha,\ell\ell'\sigma}$, where $\sigma = \pm 1/2$ and $P_\alpha = \delta_{\alpha,T}P_T$.

Taking all these considerations into account, we can write:

$$\Omega \approx \frac{eV_{AC}}{h|\delta_{ab}|}\sum_\alpha \int_{-\infty}^{+\infty} d\epsilon \left[\sum_{m_-}(1-n_F(\epsilon))\frac{\Lambda_{m^-,\alpha}}{\Delta E_{m_-} - \mu_- + \epsilon} + \sum_{m_+} n_F(\epsilon)\frac{\Lambda_{m^+,\alpha}}{\Delta E_{m_+} + \mu_+ - \epsilon}\right], \quad (2.34)$$

where we have defined

$$\Lambda_{m^\pm,\alpha} = \sum_{\ell\ell'\sigma}(1 + 2\sigma P_\alpha)\Gamma'_{\alpha,\ell\ell'\sigma}\gamma_{ab}^{m^\pm}(\ell\sigma,\ell'\sigma), \quad (2.35)$$

Equation (2.34) is the central result of the STM-ESR based on a cotunneling description. It is worth mentioning that the oscillating electric field can induce a variation of the tip-adatom and adatom-surface distances [24], leading to an additional modulation of

the tunnel current. This variation will affect the Rabi frequency through δ_{ab} and, as a consequence, the hybridizations $V_{\eta,\mathrm{i}}$. Since the effect is not distinguishable from the one associated to the barrier height modulation, which already reproduces the order of magnitude of the observed Rabi frequency, we do not include it.

2.3 Floquet theory approach

Floquet theory is the study of the stability of linear periodic systems in continuous time. It can be a really useful tool to study nonequilibrium dynamics and has been proved to have potential uses in ecological and evolutionary models [58]. Futhermore, when it is applied to physical systems with periodic potentials, such as crystals in condensed matter physics, the result is equivalent to the Bloch's theorem [59].

Consider a set of linear, homogeneous, time-periodic differential equations as

$$\dot{x}(t) = A(t)x(t),$$

being x a n-dimensional vector and $A(t)$ a $n \times n$ matrix with some periodic structure, $A(t) = A(T+t)$. Despide it, solutions of $x(t)$ are not typically periodic and its general form is

$$x(t) = \sum_n c_n e^{\mu_n t} y_n(t),$$

where the c_n components are related to the initial conditions of the problem, $y_n(t)$ is a vector of periodic functions with period T, and μ_n are complex numbers called characteristic or Floquet exponents. Therefore, the solution of the system is a sum of periodic function that can grow or decrease exponentially. Floquet exponents can be interpreted as the growth/decay rate of different perturbations averaged over a cycle. The stability of the solution requires that all Floquet exponents have a negative real part. The way of computing these exponents can be really challenging. Fortunately, if we are interested only in the steady state, we do not need to compute Floquet exponents since they only control the transient evolution which vanishes in the steady state. Then, our only concern is to find a periodic state-space change of basis, such that the matrix $A(t)$ is constant. This will clearly simplify the dynamic, and, in particular, the study of its stability properties. This change of basis is always provided by the Floquet theorem, which gives us the important result of transforming a differential periodic system into a linear one of algebraic equations which does not depend on time.

2.3.1 Model Hamiltonian of STM-ESR and Rate equation

In this section we introduce a model which would allow us to describe the STM-ESR experiment using everything we learnt in the last sections. The model will be a quantum dot with orbital structure and total spin S, coupled to two electron reservoirs which could represent the substrate hosting the impurity and the STM tip. A DC and AC bias voltage is applied between both reservoirs. Both systems, dot and electrodes, are connected through a tunneling Hamiltonian. The time dependent part of the ESR will be introduced in the tunneling strength as $w_\alpha(t) = w_\alpha^0(1 + A_\alpha \cos\omega t)$ with $A_\alpha = V_{AC}^\alpha/\delta_{ab}$ just like we showed previously and in [46], with δ_{ab} given by Eq. (2.32). V_{AC}^α is the amplitude of the AC voltage applied at the reservoir α. It modulates the tunneling coupling after a gauge transformation [60])

By using the Green's function technique, the Fourier-Floquet transformation and the master-equation theory, we will be able to write a Floquet time-dependent differential equation for the reduced density matrix of the QD. This will allows us to compute the current and other parameters of interest in order to compare with the experiment.

The total Hamiltonian is the sum of three different contributions: electrodes, tunneling and quantum dot,

$$\hat{\mathcal{H}}(t) = \hat{\mathcal{H}}_{res} + \hat{\mathcal{H}}_T(t) + \hat{\mathcal{H}}_S.$$

The first one is

$$\hat{\mathcal{H}}_{res} = \sum_{\alpha k\sigma}(\varepsilon_{\alpha k} - \mu_\alpha)c_{\alpha k\sigma}^\dagger c_{\alpha k\sigma} = \sum_{\alpha k\sigma}\xi_{\alpha k}c_{\alpha k\sigma}^\dagger c_{\alpha k\sigma}, \tag{2.36}$$

where $\alpha = \mathrm{sub}, \mathrm{tip}$ or L, R identifies the degrees of freedom for the substrate and tip, respectively, while $\sigma = -1/2, 1/2$. So $c_{\alpha k\sigma}$ ($c_{\alpha k\sigma}^\dagger$) annihilate (create) electrons in the corresponding reservoir with a spin projection σ. These two systems have temperatures and chemical potentials T_α, μ_α.

The quantum impurity is modeled by a spin-interacting Hamiltonian, $\hat{\mathcal{H}}_S$, similar to the one found in [61]. From here on $\hat{\mathcal{H}}_S$ will be referred as magnetic-impurity Hamiltonian, central system Hamiltonian or quantum dot (QD) Hamiltonian. For simplicity, we consider a single-orbital degree of freedom for the itinerant electrons, which couples mag-

netically with the other electrons in the impurity represented by the sum of their spins, **S**. Then, the QD Hamiltonian becomes:

$$\hat{\mathcal{H}}_S = \sum_\sigma \varepsilon_\sigma(t) d_\sigma^\dagger d_\sigma + J\hat{\mathbf{s}}\cdot\hat{\mathbf{S}} + U\hat{n}_{d\uparrow}\hat{n}_{d,\downarrow} + D(\hat{S}_z + \hat{s}_z)^2 + g\mu_B\mathbf{B}\cdot(\hat{\mathbf{S}} + \hat{\mathbf{s}}), \tag{2.37}$$

where $\hat{\mathbf{s}}$ is the spin operator for the itinerant electrons when they are on the QD $\hat{s}_j = \sum_{\sigma\sigma'} d_\sigma^\dagger \sigma^j_{\sigma\sigma'} d_{\sigma'}/2$ where $\hat{\sigma}^j$, $j = x, y, z$ are the Pauli matrices. ε_σ is the energy of the conduction electrons when they are on the QD. The presence of the electron on the QD is given by the occupation operator $\hat{n}_{d\sigma} = d_\sigma^\dagger d_\sigma$. J is the magnetic coupling constant, which denotes the strength of the exchange interaction between the effective local spin of the remaining electrons in the QD, $\hat{\mathbf{S}}$, and the itinerant/conduction electron spin *on the QD*, $\hat{\mathbf{s}}$. This interaction mimics the Hund's coupling inside a magnetic atom. The total spin on the QD is then $\hat{\mathbf{S}}_T = \hat{\mathbf{S}} + \hat{\mathbf{s}}$. U is the charging energy of the QD, D is the uniaxial anisotropy parameter and **B** is the external uniform magnetic field applied, acting on the total spin, $\hat{\mathbf{S}}_T$ of the QD. Notice that the spin operator, $\hat{\mathbf{S}}$ will commute with the single-particle creation and annihilation operators, $d_\sigma^{(\dagger)}$, because it acts on a different subspace.

Finally, the tunneling coupling connecting the QD to the two reservoirs is described by the Hamiltonian

$$\hat{\mathcal{H}}_T = \sum_{\alpha k\sigma} \left(w_\alpha(t) c_{\alpha k\sigma}^\dagger d_\sigma + w_\alpha^*(t) d_\sigma^\dagger c_{\alpha k\sigma} \right),$$

where $w_\alpha(t) = w_\alpha^0(1 + A_\alpha \cos\omega t)$ represents the hybridization between the reservoirs and the conduction orbital of the QD.

We will focus on the limit $U \to \infty$, in which case the QD orbital can be only empty or singly occupied. In such a case, it is convenient to introduce the product basis: $|\uparrow, m\rangle$, $|\downarrow, m\rangle$, $|0, m\rangle$[4]. The first quantum number $p = -1/2, 0, 1/2$ refers to the state of the conduction orbital while $m = -S, -S+1, \cdots, S$ correspond to the z-spin projection of the rest of the QD spin, S. The Fock space has dimension $3\times(2S+1)$ and the central-system Hamiltonian

[4]The double occupation state $|\uparrow\downarrow, m\rangle$ is missing from the basis set because of the $U \to \infty$ approximation, which implies that the electron-hole symmetry is lost.

now takes the form:

$$\hat{\mathcal{H}}_S = \sum_{mp} \varepsilon_{pm}(t)|p,m\rangle\langle p,m| + \sum_{m}^{S-1}(J_+|\downarrow, m+1\rangle\langle\uparrow, m| + J_-|\uparrow, m\rangle\langle\downarrow, m+1|) + H_{zeeman},$$

being now $\varepsilon_{pm} = (\varepsilon_\sigma + Jm\sigma + g\mu_B B_z\sigma)\delta_{\sigma p} + g\mu_B B_z m + D(m+\sigma\delta_{p,\sigma})^2$ while J_+ and J_- are equal to $J\sqrt{S(S+1)-m(m+1)}/2$. The corresponding tunneling Hamiltonian expressed in this basis reads as

$$\hat{\mathcal{H}}_T = \sum_{\alpha k\sigma m}\left(w_\alpha(t)c^\dagger_{\alpha k\sigma}|0,m\rangle\langle\sigma,m| + w^*_\alpha(t)|\sigma,m\rangle\langle 0,m|c_{\alpha k\sigma}\right).$$

We proceed similarly to Refs. [62, 63, 64, 65, 66, 67, 68] to derive the quantum master equation by treating the coupling between the impurity and the reservoirs at the lowest order in perturbation theory in the framework of non-equilibrium Green's function formalism. Notice that the chosen basis set includes different number of particles in the QD. Hence, the QD Hamiltonian is block diagonal. To this end, it is convenient to express the Hamiltonian of the impurity and the tunneling coupling in the basis of eigenstates of the impurity Hamiltonian, $|j\rangle$, with $j = 1, ..., 3(2S+1)$, which allows us to write $\hat{\mathcal{H}}'_S = \sum_j E_j|j\rangle\langle j| = \sum_j E_j\hat{\rho}_{jj} = U\hat{\mathcal{H}}_S U^\dagger$. We define the operators $\hat{\rho}_{lj} = |l\rangle\langle j|$ that project onto the basis of the eigenstates of the QD Hamiltonian.[5] The next step is to change the tunneling Hamiltonian using this basis set of eigenstates:

$$\hat{\mathcal{H}}'_T(t) = \sum_{\alpha k\sigma lj}\left(w_\alpha(t)\lambda_{lj\sigma}c^\dagger_{\alpha k\sigma}\hat{\rho}_{lj} + w^*_\alpha(t)\mu_{lj\sigma}\hat{\rho}_{lj}c_{\alpha k\sigma}\right), \tag{2.38}$$

where we have defined

$$\lambda_{lj\sigma} = \langle l|\Pi_\sigma|j\rangle \;\;;\;\; \mu_{lj\sigma} = \langle l|\Pi^\dagger_\sigma|j\rangle = \lambda^\dagger_{jl\sigma} \;\;;\;\; \Pi_\sigma = \sum_m |0,m\rangle\langle\sigma,m|.$$

[5]The step of diagonalizing the central system Hamiltonian is only possible because it is independent of time. If we introduced the time periodic function into the energy of the conduction electrons of the impurity of the down and up states, we would need to build a time-independent Hamiltonian through the Floquet theory first. This would imply to extend the basis by including the Floquet numbers, making everything more challenging. A trick would be to introduce the matrix elements of the reduced density operator in the time-periodic basis called Floquet state. This basis leads to time-independent density matrix elements in steady state. All this is ensured by the Floquet theorem [50].

Here, Π_σ is a Hubbard operator in the original QD basis set describing the charge change of the QD [69].

Since the evolution of any operator can be written in terms of the matrix elements of that operator and the density matrix, our purpose is to derive the equation of motion for the reduced density matrix $\hat{\rho}(t) = \mathrm{Tr}_{\mathrm{res}}[\hat{\rho}_T(t)]$, where the trace is taken over the degrees of freedom of the reservoirs and $\hat{\rho}_T$ is the density matrix of the full system coupled to the reservoirs by $\hat{\mathcal{H}}$. In particular, using the definitions above, we can write the matrix elements of the reduced density matrix in the QD-eigenstate basis set, $\{|j\rangle\}$, as $\rho_{lj}(t) = \mathrm{Tr}[\hat{\rho}_T(t)\hat{\rho}_{jl}]$, where the trace is now over all degrees of freedom and the QD indices are inverted.

Before going further, it is convenient to change to the Heisenberg representation where the density matrix remains constant, i.e., $\hat{\rho}_T^H = \hat{\rho}_0 = \hat{\rho}_{\mathrm{res}} \otimes \hat{\rho}$, being $\hat{\rho}_0$ the initial density matrix when the system is decoupled exactly into the reservoir and the system part, and the operators evolve in time according to $\hat{O}^H(t) = U^\dagger(t)\hat{O}^S(t)\hat{U}(t)$. Here $U(t,t_0) = \hat{T}\left\{e^{-i\int_{t_0}^{t} dt' \hat{\mathcal{H}}(t')/\hbar}\right\}$ is the time evolution operator and $\hat{T}$ the time-order operator. The superindex "H" denotes that we are expressing the operators in the Heisenberg picture. The components of the reduced density matrix can be then written as $\rho_{lj}(t) = \langle \hat{\rho}_{lj}^H(t)\rangle = \mathrm{Tr}\left[\hat{\rho}_0 \hat{\rho}_{jl}^H(t)\right]$, with $\hat{\rho}_{lj}^H(t) = U(t,t_0)\hat{\rho}_{lj}U^\dagger(t,t_0)$. Moreover, for an arbitrary time-dependent operator $\hat{O}(t)$, we have that the expectation value can be obtained as $\langle \hat{O}(t)\rangle = \mathrm{Tr}\left[\hat{\rho}_0 \hat{O}^H(t)\right]$. In the limit of weak coupling strength between the $3(2S+1)$-levels system and the electrodes, the so-called Born approximation, we can assume that the total density matrix can be always factorized as the initial ρ_0 [70]. The emergence of correlations which prohibit the latter are related to memory effects which are linked to non-Markovian behavior. In the weak coupling situation, applying the Heisenberg equation of motion to $\hat{\rho}_{ij}^H(t)$ and taking the mean value with respect $\hat{\rho}_0$ leads to the equation ruling the dynamics of $\rho_{ij}(t)$:

$$\frac{d\rho_{lj}}{dt} = \frac{d\langle \hat{\rho}_{lj}^H\rangle}{dt} = \frac{i}{\hbar}\left\langle \left[\hat{\mathcal{H}}_S'^H, \hat{\rho}_{lj}^H\right]\right\rangle + \frac{i}{\hbar}\left[\sum_{\alpha k\sigma u} w_\alpha \lambda_{ul\sigma}\langle c_{\alpha k\sigma}^{\dagger H}\hat{\rho}_{uj}^H\rangle\right.$$

$$\left. - \sum_{\alpha k\sigma v} w_\alpha \lambda_{jv\sigma}\langle c_{\alpha k\sigma}^{\dagger H}\hat{\rho}_{lv}^H\rangle + \sum_{\alpha k\sigma u} w_\alpha^* \mu_{ul\sigma}\langle \hat{\rho}_{uj}^H c_{\alpha k\sigma}^H\rangle - \sum_{\alpha k\sigma v} w_\alpha^* \mu_{jv\sigma}\langle \hat{\rho}_{lv}^H c_{\alpha k\sigma}^H\rangle\right], \tag{2.39}$$

where we have use the fact[6] that $\hat{\rho}_{uv}\hat{\rho}_{lj} = \hat{\rho}_{uj}\delta_{vl}$. The reader might be suprised by the use of the Heisenberg picture to derive an equation of motion for the density matrix. We emphasize that $\hat{\rho}^H_{ij}(t)$ are not density matrices but similar to creation or annihilation operators, making necessary the use of the Heisenberg picture. From now on, every operator would be in the Heisenberg picture so we will omit all the superindexes "H". The terms that combine the $c_{\alpha k\sigma}$ ($c^\dagger_{\alpha k\sigma}$) and $\hat{\rho}_{lj}$ invite us to define Green's function such as:

$$G^<_{\alpha k\sigma,lj}(t,t') = \pm i\langle\hat{\rho}^\dagger_{jl}(t')c_{\alpha k\sigma}(t)\rangle = \pm i\langle\hat{\rho}_{lj}(t')c_{\alpha k\sigma}(t)\rangle$$

$$G^<_{lj,\alpha k\sigma}(t,t') = \pm i\langle c^\dagger_{\alpha k\sigma}(t')\hat{\rho}_{lj}(t)\rangle$$

$$G^<_{lj,uv}(t,t') = \pm i\langle\hat{\rho}_{uv}(t')\hat{\rho}_{lj}(t)\rangle.$$

$$G^<_{\alpha k\sigma}(t,t') = i\langle c^\dagger_{\alpha k\sigma}(t')c_{\alpha k\sigma}(t)\rangle$$

Here, we are assuming time-ordering along the Schwinger-Keldysh contour [68]. The "+" sign refers to have many-body ket state such that $|l\rangle$, $|j\rangle$ and $|u\rangle$, $|v\rangle$ differ in one or any odd number of particles and then $\hat{\rho}_{lj}$ and $\hat{\rho}_{uv}$ present a fermionic character. Otherwise, if we take the "$-$" sign, these density matrices have a bosonic character. Following this idea, let us divide the space into the two diferent combination of ket states: in the first ones, we have $|j\rangle = \sum_{\sigma m} A_{\sigma m}|\sigma, m\rangle$ with σ being only up and down, therefore $\hat{\rho}^b_{lj} = |l\rangle\langle j| = \sum_{\sigma m\sigma' m'} A_{\sigma m}A^*_{\sigma' m'}|\sigma, m\rangle\langle\sigma', m'|$. To clarify this, if we just focus on the σ spin projection, $m = m' = 0$, we have four possible combination: up-up, up-down, down-up, down-down. These combinations imply a total integer spin, therefore we have a bosonic operator. Contrary we have the situation of a empty state, $\hat{\rho}^f_{lj} = |l\rangle\langle j| = \sum_{m\sigma' m'} A_{0m}A^*_{\sigma' m'}|0, m\rangle\langle\sigma', m'|$. Again, if we focus on the σ parts, we see that the states differ in one particle with half-integer spin, we have a fermionic operator then. These

[6]Notice that we are actually using Hubbard operators here. These operators satisfy a graded Lie algebra: $[\hat{\rho}_{uv}\hat{\rho}_{lj}]_\pm = \hat{\rho}_{uj}\delta_{vl} \pm \hat{\rho}_{lv}\delta_{ju}$, where the plus sign is only for fermions. The absence of a Wick's theorem [71] for these operators is normally overcome by factorizing the fermionic Hubbard operators as a product of canonical creation and annihilation operators. This can be done by representing the empty state by a "slave boson" and the spin by a fermion. By making this, we could apply Wick's theorem to the fermionic operators and use it to compute the mixed Green's functions. The only down side about this is that the Green's function of the isolated impurity Hamiltonian is a bit different from what one could expect.

arguments are also valided for any m and m' values. In any case, from (2.39) one notice that only a Fermion operator could survive because $c_{\alpha k\sigma}$ ($c^\dagger_{\alpha k\sigma}$) needs a empty ket to the right (left). Therefore

$$G^<_{\alpha k\sigma,lj}(t,t') = i\langle \hat{\rho}^f_{lj}(t') c_{\alpha k\sigma}(t)\rangle$$
$$G^<_{lj,\alpha k\sigma}(t,t') = i\langle c^\dagger_{\alpha k\sigma}(t')\hat{\rho}^f_{lj}(t)\rangle.$$

From here on, if nothing is said, $\hat{\rho}_{lj}$ will be a Fermion operator so the "f" superindexes are dropped out.

Our aim now is to compute these mixed Green's functions. Let us calculate the evolution of $c^\dagger_{\alpha k\sigma}$ and $c_{\alpha k\sigma}$ using the Heisenberg equation of motion

$$i\hbar\frac{\partial c^\dagger_{\alpha' k'\sigma'}}{\partial t'} = -[\hat{\mathcal{H}}_{res} + \hat{\mathcal{H}}_T, c^\dagger_{\alpha' k'\sigma'}] = -(\xi_{\alpha' k'} c^\dagger_{\alpha' k'\sigma'} + \sum_{uv} w^*_{\alpha'} \mu_{uv\sigma'}\hat{\rho}_{uv}(t')) \tag{2.40}$$

$$i\hbar\frac{\partial c_{\alpha' k'\sigma'}}{\partial t} = -[\hat{\mathcal{H}}_{res} + \hat{\mathcal{H}}_T, c_{\alpha' k'\sigma'}] = (\xi_{\alpha' k'} c_{\alpha' k'\sigma'} + \sum_{uv} w_{\alpha'} \lambda_{uv\sigma'}\hat{\rho}_{uv}(t)), \tag{2.41}$$

where we have used $\{c^\dagger_{\alpha k\sigma}, c_{\alpha' k'\sigma'}\} = \delta_{\alpha,\alpha'}\delta_{k,k'}\delta_{\sigma,\sigma'}$. Computing the equation of motion of the mixed Green's function [72], we find that

$$G^c_{lj,\alpha' k'\sigma'}(t,t') = \sum_{uv}\int dt_1 G^c_{lj,uv}(t,t_1)\mu_{uv\sigma} t^*_{\alpha' k'}(t_1) g^c_{\alpha' k'\sigma'}(t_1 - t'), \tag{2.42}$$

where $c \equiv r, a, >, <$ indicates the Keldysh contour, see Appendix D. By using the Langreth theorem in the Schwinger-Keldysh contour [73], at the 1st-order of perturbation theory in $w^0_{\alpha k}$, the lesser mix Green's Function can be written as

$$G^<_{lj,\alpha k\sigma}(t,t') \approx \int dt_1 \sum_{uv}\mu_{uv\sigma} t^*_{\alpha k}(t_1)\left[g^r_{lj,uv}(t,t_1) g^<_{\alpha k\sigma}(t_1 - t') + g^<_{lj,uv}(t,t_1) g^a_{\alpha k\sigma}(t_1 - t')\right].$$

In addition we have

$$G^c_{\alpha k\sigma,lj}(t,t') = \sum_{uv}\int dt_1 g^c_{\alpha k\sigma}(t - t_1)\lambda_{uv\sigma} t_{\alpha k}(t_1) G^c_{uv,lj}(t_1,t'), \tag{2.43}$$

whose lesser mix Green's Function up to 1st-order of perturbation theory is

$$G^<_{\alpha k\sigma,lj}(t,t') \approx \int dt_1 \sum_{uv}\lambda_{uv\sigma} t_{\alpha k}(t_1)\left[g^r_{\alpha k\sigma}(t - t_1) g^<_{uv,lj}(t_1,t') + g^<_{\alpha k\sigma}(t - t_1) g^a_{uv,lj}(t_1,t')\right],$$

These mix Green's functions contain the isolated Green's function of the QD Hamiltonian, $g^c_{lj,uv}(t,t')$, and the electrode one, $g^c_{\alpha k\sigma}(t,t')$. This last one is easily computed [74]. We now introduce the lesser and greater Green's functions for these isolated systems,

$$\begin{aligned} g^<_{lj,uv}(t,t') &= i\langle \hat{\rho}_{uv}(t')\hat{\rho}_{lj}(t)\rangle, \\ g^<_{\alpha k\sigma}(t,t') &= i\langle c^\dagger_{\alpha k\sigma}(t')c_{\alpha k\sigma}(t)\rangle, \\ g^>_{lj,uv}(t,t') &= -i\langle \hat{\rho}_{lj}(t)\hat{\rho}_{uv}(t')\rangle, \\ g^>_{\alpha k\sigma}(t,t') &= -i\langle c_{\alpha k\sigma}(t)c^\dagger_{\alpha k\sigma}(t')\rangle. \end{aligned}$$

While the retarded and advanced ones are, respectively,

$$g^r_{\nu,\nu'}(t,t') = \theta(t-t')\left[g^>_{\nu,\nu'}(t,t') - g^<_{\nu,\nu'}(t,t')\right]$$

and

$$g^a_{\nu,\nu'}(t,t') = -\theta(t'-t)\left[g^>_{\nu,\nu'}(t,t') - g^<_{\nu,\nu'}(t,t')\right].$$

If we now substitute the mixed Green's function into the equation of motion and follow the algebra in Appendix E, where we also defined the rates, we get the master equation

$$\hbar\dot{\rho}_{lj}(t) - i\Delta_{lj}\rho_{lj}(t) = \sum_{vu}\left[\Gamma_{vl,ju}(t)\rho_{vu}(t) + \bar{\Gamma}_{vl,uv}(t)\rho_{uj}(t) - \Gamma_{jv,vu}(t)\rho_{lu}(t) - \bar{\Gamma}_{jv,ul}(t)\rho_{uv}(t)\right], \tag{2.44}$$

being $\Delta_{lj} = E_l - E_j$. We calculate the explicit form of the rates in Appendix F, which are

$$\Gamma_{vl,ju}(t) = \frac{1}{2\pi}\left(\sum_{nn'} e^{i(n'-n)\omega t}\sum_{\alpha\sigma}\lambda_{vl\sigma}\mu_{ju\sigma}\int_{-\infty}^{+\infty} d\varepsilon \frac{1}{\varepsilon - \Delta_{ju}/\hbar + i0^+}\Sigma^<_{\alpha\sigma,nn'}(\varepsilon - n\omega) + \right.$$
$$\left.\sum_{nn'} e^{-i(n-n')\omega t}\sum_{\alpha\sigma}\mu_{vl\sigma}\lambda_{ju\sigma}\int_{-\infty}^{+\infty} d\varepsilon\left[2\pi i\delta(\varepsilon - \Delta_{uj}/\hbar)\Sigma^r_{\alpha\sigma,nn'}(\varepsilon - n'\omega) + \frac{\Sigma^<_{\alpha\sigma,nn'}(\varepsilon - n'\omega)}{\varepsilon - \Delta_{uj}/\hbar - i0^+}\right]\right).$$

Here we have introduced the Fourier-Floquet transform of the self-energy

$$\Sigma^c_{\alpha\sigma,nn'}(\varepsilon) = \sum_k |w^0_\alpha|^2\left[\delta_{n,0} + \frac{A_\alpha}{2}(\delta_{n,-1} + \delta_{n,1})\right] g^c_{\alpha k\sigma}(\varepsilon)\left[\delta_{n',0} + \frac{A_\alpha}{2}(\delta_{n',-1} + \delta_{n',1})\right], \tag{2.45}$$

with $c \equiv r, a, >, <$ and $w_{\alpha,n}$ being the coefficient of the time-periodic tunneling term expanded in Fourier series. Making $n'' = n - n'$ while we take out n' in the first term and

n in the second and then changing $n' = n$ in the second term and $n'' = n'$ in both terms we have

$$\Gamma_{vl,ju}(t) = \frac{1}{2\pi}\sum_{n'} e^{-in'\omega t}\left(\sum_{n}\sum_{\alpha\sigma}\lambda_{vl\sigma}\mu_{ju\sigma}\int_{-\infty}^{+\infty} d\varepsilon \frac{1}{\varepsilon - \Delta_{ju}/\hbar + i0^{+}}\Sigma^{<}_{\alpha\sigma,nn-n'}(\varepsilon - n\omega) + \right.$$
$$\left.\sum_{n}\sum_{\alpha\sigma}\mu_{vl\sigma}\lambda_{ju\sigma}\int_{-\infty}^{+\infty} d\varepsilon\left[2\pi i\delta(\varepsilon - \Delta_{uj}/\hbar)\Sigma^{r}_{\alpha\sigma,n'+nn}(\varepsilon - n\omega) + \frac{\Sigma^{<}_{\alpha\sigma,n'+nn}(\varepsilon - n\omega)}{\varepsilon - \Delta_{uj}/\hbar - i0^{+}}\right]\right),$$

which has a natural form of a periodic function of period $T = 2\pi/\omega$ for a fixed angular frequency ω:

$$\Gamma_{vl,ju}(t) = \sum_{n'} e^{-in'\omega t}\Gamma_{vl,ju;n'}(\omega), \tag{2.46}$$

being the Fourier-Floquet components equal to

$$\Gamma_{vl,ju;n'}(\omega) = \frac{1}{2\pi}\left(\sum_{n\alpha\sigma}\lambda_{vl\sigma}\mu_{ju\sigma}\int_{-\infty}^{+\infty} d\varepsilon \frac{1}{\varepsilon - \Delta_{ju}/\hbar + i0^{+}}\Sigma^{<}_{\alpha\sigma,nn-n'}(\varepsilon - n\omega) + \right.$$
$$\left.\sum_{n\alpha\sigma}\mu_{vl\sigma}\lambda_{ju\sigma}\int_{-\infty}^{+\infty} d\varepsilon\left[2\pi i\delta(\varepsilon - \Delta_{uj}/\hbar)\Sigma^{r}_{\alpha\sigma,n+n'n}(\varepsilon - n\omega) + \frac{\Sigma^{<}_{\alpha\sigma,n+n'n}(\varepsilon - n\omega)}{\varepsilon - \Delta_{uj}/\hbar - i0^{+}}\right)\right]. \tag{2.47}$$

Assuming that the imaginary part of the rates can be treated as a renormalization term and using the results of Appendix F we have

$$\Gamma_{vl,ju;n'}(\omega) = \frac{1}{2}\sum_{n\alpha\sigma}\left(\lambda_{vl\sigma}\mu_{ju\sigma}\Gamma_{\alpha\sigma}n_F(\Delta_{ju} - n\omega)\left[\delta_{n,n'} + \frac{A_\alpha}{2}\left(\delta_{n,n'+1} + \delta_{n,n'-1}\right)\right] - \right.$$
$$\left.\mu_{vl\sigma}\lambda_{ju\sigma}\Gamma_{\alpha\sigma}(n_F(\Delta_{uj} - n\omega) - 1)\left[\delta_{n,-n'} + \frac{A_\alpha}{2}\left(\delta_{n,-n'+1} + \delta_{n,-n'-1}\right)\right]\right)\left[\delta_{n,0} + \frac{A_\alpha}{2}\left(\delta_{n,1} + \delta_{n,-1}\right)\right]. \tag{2.48}$$

Similarly, we have that

$$\bar{\Gamma}_{jv,ul}(t) = \sum_{n'} e^{-in'\omega t}\bar{\Gamma}_{jv,ul;n'}(\omega), \tag{2.49}$$

where now

$$\bar{\Gamma}_{jv,ul;n'}(\omega) = \frac{1}{2\pi}\left(\sum_{n\alpha\sigma}\mu_{jv\sigma}\lambda_{ul\sigma}\int_{-\infty}^{+\infty} d\varepsilon\Sigma^{<}_{\alpha\sigma,n+n'n}(\varepsilon - n\omega)\frac{1}{\varepsilon - \Delta_{lu}/\hbar - i0^{+}} + \right.$$
$$\left.\sum_{n\alpha\sigma}\lambda_{jv\sigma}\mu_{ul\sigma}\int_{-\infty}^{+\infty} d\varepsilon\left[\frac{\Sigma^{<}_{\alpha\sigma,nn-n'}(\varepsilon - n\omega)}{\varepsilon - \Delta_{ul}/\hbar + i0^{+}} + 2\pi i\delta(\varepsilon - \Delta_{ul}/\hbar)\Sigma^{a}_{\alpha\sigma,nn-n'}(\varepsilon - n\omega)\right]\right). \tag{2.50}$$

From Appendix F one can write:

$$\bar{\Gamma}_{jv,ul;n'}(\omega) = -\frac{1}{2}\sum_{n\alpha\sigma}\left(\mu_{jv\sigma}\lambda_{ul\sigma}\Gamma_{\alpha\sigma}n_F(\Delta_{lu}-n\omega)\left[\delta_{n,-n'}+\frac{A_\alpha}{2}\left(\delta_{n,-n'+1}+\delta_{n,-n'-1}\right)\right]-\right.$$

$$\left.\lambda_{jv\sigma}\mu_{ul\sigma}\Gamma_{\alpha\sigma}(n_F(\Delta_{ul}-n\omega)-1)\left[\delta_{n,n'}+\frac{A_\alpha}{2}\left(\delta_{n,n'+1}+\delta_{n,n'-1}\right)\right]\right)\left[\delta_{n,0}+\frac{A_\alpha}{2}\left(\delta_{n,1}+\delta_{n,-1}\right)\right]. \quad (2.51)$$

It is important to note that the rates equations (2.48) and (2.51) follow the relation $\Gamma_{ijvu}(t) = -\bar{\Gamma}_{jiuv}(t)$. Since the rates are periodic functions, the master equation is a Floquet differential equation of the form $\dot{\rho}(t) = \Gamma(t)\rho(t)$, being $\rho(t)$ a vector that contains all density matrix elements and $\Gamma(t)$ a matrix that contains the rates. The general solution of such system is

$$\rho(t) = \sum_i c_i e^{\mu_i t} p_i(t),$$

where c_i components are related to the initial conditions of the problem, $p_i(t)$ is a function vector with period $T = 2\pi/\omega$ for a fixed frequency and μ_i are called characteristic or Floquet exponents. We are interested in the solution for large times, the steady state, so we can omitt all solutions with $\Re(\mu_i) < 0$, which decay to zero in this time limit and are of no further interest. From the general properties of a density matrix, it follows that solutions with $\Re(\mu_i) > 0$ are impossible. So we are left with discussing solutions with $\Re(\mu_i) = 0$. For the trace of the density matrix to be 1, i.e. time-independent and nonzero, there must be a solution with $\mu_i = 0$. Thus the stationary solution for the density matrix elements equal to

$$\rho_{lj}(t) = \sum_n e^{-in\omega t}\rho_{lj;n}$$

with

$$\rho_{lj;n} = \frac{\omega}{2\pi}\int_0^{2\pi/\omega}\rho_{lj}(t)e^{in\omega t}.$$

This solution of the master equation corresponds to the "long-time" limit where the transient processes vanish after switching on the tunneling contact.

We can transform the differential Eq. (2.44) into a algebraic one by making use of the Fourier-Floquet components of the rates and density matrix elements:

$$\sum_n n\omega e^{-in\omega t}\rho_{lj;n} + \frac{1}{\hbar}\sum_n (E_l - E_j)e^{-in\omega t}\rho_{lj;n} =$$

$$\frac{i}{\hbar}\sum_{vu}\sum_{nn'} e^{-i(n'+n)\omega t}\left[\Gamma_{vl,ju;n'}\rho_{vu;n} + \bar{\Gamma}_{vl,uv;n'}\rho_{uj;n} - \Gamma_{jv,vu;n'}\rho_{lu;n} - \bar{\Gamma}_{jv,ul;n'}\rho_{uv;n}\right].$$

If we make $n' + n = n$ in the second term, multiply the equation by $e^{in''t}$ and integrate everything over t, we get kronecker deltas of type $\delta_{n,n''}$ which leads us to the equation

$$(E_l - E_j)\rho_{lj;n} + n\hbar\omega\rho_{lj;n} = i\sum_{vu;n'}\left[\Gamma_{vl,ju;n'}\rho_{vu;n-n'} + \bar{\Gamma}_{vl,uv;n'}\rho_{uj;n-n'} - \Gamma_{jv,vu;n'}\rho_{lu;n-n'} - \bar{\Gamma}_{jv,ul;n'}\rho_{uv;n-n'}\right]. \tag{2.52}$$

In order to make the system of equation finite and solve it, we need to truncate it at a given Floquet number n. Importantly, all the information on the temperature and chemical potential of a given reservoir is only encoded in the Fermi distribution functions

$$n_F(\epsilon) = \frac{1}{e^{(\epsilon - E_{f_\alpha})/k_B T_\alpha} + 1},$$

where E_{f_α} is the Fermi energy and T_α the temperature. Moreover, the polarization is introduced in $\Gamma_{\alpha\sigma}$ by changing it to $\Gamma_{\alpha\sigma} = (1/2 - \sigma P_\alpha)\Gamma'_\alpha$, similar to what we did in the cotunneling section. P_α is the polarization of the electrode α. As we will see in the Rabi frequency section, the polarization is essential to induced and measure resonance peaks. Finally, the only thing left is to add the normalization condition or detailed balance in order to break the linear dependence that appears in the system of equations (2.52). Since $\sum_l \rho_{ll} = 1 \implies \sum_{ln} e^{-in\omega t}\rho_{ll;n} = 1$, if we multiply by $e^{in''\omega t}$ and integrate over t, we obtain $\sum_l \rho_{ll;n} = \delta_{n,0}$.

2.3.2 Current through the central system Hamiltonian

One interesting observable is the current that goes through the central system Hamiltonian when contacted by two metallic leads. We obtain the time-dependent current going out of a lead by calculating the expectation value of the time derivative of the number operator of the lead, $N_\alpha = \sum_{k\sigma} c^\dagger_{\alpha k\sigma} c_{\alpha k\sigma}$,

$$I_\alpha = -e\frac{d\langle N_\alpha\rangle}{dt} = \frac{ie}{\hbar}\langle[N_\alpha, \hat{\mathcal{H}}]\rangle = \frac{ie}{\hbar}\sum_{\substack{\alpha' k'\sigma' \\ k\sigma lj}}\left\langle\left[c^\dagger_{\alpha k\sigma}c_{\alpha k\sigma}, \left(t_{\alpha'}\lambda_{ljo'}c^\dagger_{\alpha' k'\sigma'}\hat{\rho}_{lj} + t^*_{\alpha'}\mu_{ljo'}\hat{\rho}_{lj}c_{\alpha' k'\sigma'}\right)\right]\right\rangle =$$

$$\frac{ie}{\hbar}\sum_{k\sigma lj}\left(t_\alpha\lambda_{lj\sigma}\langle c^\dagger_{\alpha k\sigma}\hat{\rho}_{lj}\rangle - t^*_\alpha\mu_{lj\sigma}\langle\hat{\rho}_{lj}c_{\alpha k\sigma}\rangle\right) = \frac{e}{\hbar}\sum_{k\sigma lj}\left(t_\alpha\lambda_{lj\sigma}G^<_{lj,\alpha k\sigma}(t,t) - t^*_\alpha\mu_{lj\sigma}G^<_{\alpha k\sigma,lj}(t,t)\right).$$

Taking into account Eqs. (E.2), (E.3), (E.14) and (E.17), we have:

$$I_\alpha(t) = \frac{e}{\hbar}\sum_{\sigma lj}\left(\lambda_{lj\sigma}\Lambda_{lj,\alpha\sigma}(t) - \mu_{lj\sigma}\bar{\Lambda}_{\alpha\sigma,lj}(t)\right)$$

$$\implies I_\alpha(t) = \frac{e}{\hbar}\sum_{\sigma lj}\left[\lambda_{lj\sigma}\left(\sum_v \rho_{lv}(t)\eta_{jv,\alpha\sigma}(t) + \sum_u \rho_{uj}(t)\eta'_{ul,\alpha\sigma}(t)\right) - \right.$$

$$\left.\mu_{lj\sigma}\left(\sum_u \rho_{uj}(t)\gamma_{\alpha\sigma,ul}(t) + \sum_v \rho_{lv}(t)\gamma'_{\alpha\sigma,jv}(t)\right)\right].$$

Changing the v index by u and using the definition $\Gamma_{lj,ju,\alpha}(t) = \sum_\sigma(\lambda_{lj\sigma}\eta_{ju,\alpha\sigma}(t) - \mu_{lj\sigma}\gamma'_{\alpha\sigma,ju}(t))$ and $\bar{\Gamma}_{lj,ul,\alpha}(t) = \sum_\sigma(\mu_{lj\sigma}\gamma_{\alpha\sigma,ul}(t) - \lambda_{lj\sigma}\eta'_{ul,\alpha\sigma}(t))$ we can write

$$I_\alpha(t) = \frac{e}{\hbar}\sum_{lju}\left[\rho_{lu}(t)\Gamma_{lj,ju,\alpha}(t) - \rho_{uj}(t)\bar{\Gamma}_{lj,ul,\alpha}(t)\right].$$

Notice the change of one sign in the rate's definitions with respect the one we apply in Appendix E, which was used to write Eqs. (2.47) and (2.50). The minus sign in the middle comes out naturally and it ensures that $I_L + I_R = 0$. The last equation for the current can be rewritten using the Fourier-Floquet components of the reduced matrix density and the new rates, which are still periodic for a fixed frequency,

$$I_\alpha(t) = \frac{e}{\hbar}\sum_{lju}\sum_{nn'} e^{-in\omega t}\left[\rho_{lu;n-n'}\Gamma_{lj,ju,\alpha;n'}(\omega) - \rho_{uj;n-n'}\bar{\Gamma}_{lj,ul,\alpha;n'}(\omega)\right] = \sum_n e^{-in\omega t}I_{\alpha;n}(\omega). \tag{2.53}$$

So, computing the rates and the Floquet density matrix elements allows us to calculate the current. From Eqs. (2.48) and 2.51) one notices that n' can only take the values $-2, -1, 0, 1, 2$. So, Eq. (2.53) can be simplified even further using the fact that $\Gamma_{ljju} = -\bar{\Gamma}_{jluj}$ and changing the sum indexes accordingly

$$I_\alpha(t) = \frac{2e}{\hbar} \sum_{lju} \sum_{nn'} e^{-in\omega t} \left[\mathfrak{R}(\rho_{lu;n-n'}) \Gamma_{lj,ju,\alpha;n'}(\omega) \right]. \tag{2.54}$$

While the DC current, $n = 0$ term, is

$$I_\alpha^{DC} = \frac{2e}{\hbar} \sum_{lju} \sum_{n'} \mathfrak{R}(\rho_{lu;-n'}) \Gamma_{lj,ju,\alpha;n'}(\omega). \tag{2.55}$$

If we are in a high voltage situation, $|eV_{DC}| = |E_{f_L} - E_{f_R}| \gg \hbar\omega$, or in a large energy difference between electronic states, $\Delta_{lj} \gg \hbar\omega$ with one state being empty and the other one filled, ω becomes irrelevant in Eqs. (2.48) and 2.51) and we can write down a couple of relations between the Fourier-Floquet components of the rates for different Floquet numbers:

$$\Gamma_{lj,ju,\alpha;\pm1} = \Gamma_{lj,ju,\alpha;0} \frac{A_\alpha}{1 + A_\alpha^2/2}$$

$$\Gamma_{lj,ju,\alpha;\pm2} = \Gamma_{lj,ju,\alpha;0} \frac{A_\alpha^2/4}{1 + A_\alpha^2/2}.$$

Also, notice that Eq. (2.52) tell us $\rho_{lj;n} = \rho^*_{jl;-n}$, so

$$I_\alpha^{DC} = \frac{2e}{\hbar} \sum_{lju} \left[\mathfrak{R}(\rho_{lu;0}) + \mathfrak{R}(\rho_{lu;1}) \frac{2A_\alpha}{1 + A_\alpha^2/2} + \mathfrak{R}(\rho_{lu;2}) \frac{A_\alpha^2/2}{1 + A_\alpha^2/2} \right] \Gamma_{lj,ju,\alpha;0}. \tag{2.56}$$

This simplified version of the current, and the fact that the rates does not depend on the frequency in this regime, allow us to reduced the computational time of the program by a lot.

2.3.3 Lifetime and decoherence time

Here we aim to obtain the lifetime and decoherence time of our system by comparing with the Bloch theory for the two level system (TLS). Lifetime is the characteristic exponential decay time toward the stationary situation. In order to make everything simpler, let us use spin zero case, so $S_T = s = 1/2$, and make the driving zero, $A_\alpha = 0$. In this simplest case we have three states: down $|1\rangle$, up $|2\rangle$ and empty $|3\rangle$ with $m = 0$. Notice that states up and down will be mixed if a transverse magnetic field is applied. If there is no polarization, see Appendix F, the rate equation for a down state is

$$\hbar\dot{\rho}_{11}(t) = \gamma_{31,13;0}\rho_{33}(t) - \gamma_{13,31;0}\rho_{11}(t), \tag{2.57}$$

while the up one is

$$\hbar\dot{\rho}_{22}(t) = \gamma_{32,23;0}\rho_{33}(t) - \gamma_{23,32;0}\rho_{22}(t), \tag{2.58}$$

where $\gamma_{3j,j3}(t) = \Gamma_{3j,j3}(t) - \bar{\Gamma}_{j3,3j}(t)$, being $j = 1, 2$. Equation (2.57) is a TLS with states $|1\rangle$ and $|3\rangle$. So, we can compare our rate equation with the one of a TLS in the Bloch-Redfield theory in order to extract a lifetime, T_1. In the steady state, Eq. (2.57) can be written as

$$\gamma_{31,13;0}\rho_{33;0} - \gamma_{13,31;0}\rho_{11;0} = 0 \implies \frac{\rho_{33;0}}{\rho_{11;0}} = \frac{\gamma_{13,31;0}}{\gamma_{31,13;0}},$$

This last equation invite us to define a lifetime of $\hbar/T_1^{13} = \gamma_{31,13;0} + \gamma_{13,31;0}$ just by comparison with the TLS previously presented in section 2.2.2. This leads to

$$\dot{\rho}_{11}(t) = \frac{1}{T_1^{13}(\rho_{11;0} + \rho_{33;0})}\left(\rho_{11;0}\rho_{33}(t) - \rho_{33;0}\rho_{11}(t)\right)$$

since $\rho_{11;0} + \rho_{33;0} \neq 1$ we cannot fully recover the TLS equation but at least we could extract a T_1 definition. The usual TLS result between states $|1\rangle$ and $|2\rangle$ is recovered when the population of the empty state is negligible, $\rho_{33}(t) \to 0$. The same procedure can be done for Eq. (2.58) obtaining another lifetime of $T_1^{23} = \hbar/(\gamma_{32,23;0} + \gamma_{23,32;0})$. Increasing the localized spin, S, will provide more complex lifetimes, making everything less intuitive: we have more empty states and each down and up states are connected because of the magnetic field and the spin interaction J. Let us see the $S = 1/2$ ($S_T = 1$), in the absence

of driving, $A_\alpha = 0$. We have 6 states: 4 filled states, $|1\rangle$, $|2\rangle$, $|4\rangle$, $|5\rangle$, and two empty ones, $|3\rangle$, $|6\rangle$. The rate equation for the state $|1\rangle$ is

$$\hbar\dot{\rho}_{11}(t) = \gamma_{31,13;0}\rho_{33}(t) - \gamma_{13,31;0}\rho_{11}(t) + \gamma_{61,16;0}\rho_{66}(t) - \gamma_{16,61;0}\rho_{11}(t).$$

We see that the only difference with respect to the $S = 0$ case is a new empty state connected to $|1\rangle$. The rate equations for different filled states are similar. So, in general, we write

$$\frac{1}{T_1} = \frac{1}{T_1^{13}} + \frac{1}{T_1^{16}} = \frac{1}{\hbar}\sum_{j=3,6}(\gamma_{j1,1j;0} + \gamma_{1j,j1;0}).$$

Thus, for any spin S and filled state we have a lifetime:

$$\frac{1}{T_1} = \sum_j \frac{1}{T_1^{lj}} = \frac{1}{\hbar}\sum_j(\gamma_{jl,lj;0} + \gamma_{lj,jl;0}). \tag{2.59}$$

Being l a filled state and j an empty one. This time depends on the state l we choose.

Much simpler is to compute the decoherence time, T_2. The loss of quantum coherence is related to the relaxation of the off-diagonal elements of the reduced density matrix. Again, it is instructive to limit ourselves to the spin zero case, $S_T = 1/2$, with $A_\alpha = 0$ and zero polarization such that,

$$\hbar\dot{\rho}_{12}(t) - i\Delta_{12}\rho_{12}(t) = (\bar{\Gamma}_{31,13;0} - \Gamma_{23,32;0})\rho_{12}(t).$$

By direct comparison with the TLS, one obtains a decoherence time of

$$T_2^{12} = \frac{\hbar}{\Gamma_{23,32;0} - \bar{\Gamma}_{31,13;0}}. \tag{2.60}$$

If we increase the dimension to the case $S = 1/2$, we have

$$\hbar\dot{\rho}_{12}(t) = i\Delta_{12}\rho_{12}(t) + \sum_{v=3,6}(\bar{\Gamma}_{v1,1v;0} - \Gamma_{2v,v2;0})\rho_{12}(t).$$

Where we see that we just need to sum over the empty states to get the decoherence time between states $|1\rangle$ and $|2\rangle$. Therefore, in general, for any pair of filled states

$$T_2^{lj} = \sum_v \frac{\hbar}{\Gamma_{jv,vj;0} - \bar{\Gamma}_{vl,lv;0}}. \tag{2.61}$$

where v shall be an empty state. Notice that we could have decoherence times of pair of empty states through a filled one that is connected to both states.

2.3.4 Rabi frequency

The Rabi frequency is the transfer rate of the population of one state towards the other state when the system is driven periodically. It is a term proportional to the off-diagonal matrix elements of the TLS effective Hamiltonian. Three conditions have to be fulfilled in order to have a finite Rabi frequency:

- A magnetic field must be applied to lift the energy degeneracy and to mix the different states. A transverse magnetic field is always necessary in this regard. If $J = 0$ when $S \neq 0$, the spins s and S are not connected, which leads to the $S_T = 1/2$ case always. Therefore, the magnetic coupling constant J is essential to simulate cases with $S \neq 0$.
- There must be a net current passing through the QD and the spin-polarized electrode must be below the Fermi level.[7]
- At least three Floquet numbers are needed, $n = 0, -1, 1$. Otherwise the rate equation does not depend on the frequency.

The reason why these three conditions are needed is to allow the terms Γ_{ijli} (and similar) being different from zero. For the rate wrote, state i could be an empty state while j and l are any different pair of filled states. Basically we need to have rates that combine three states, being one of them an empty one. In order to emphasize this idea, let us write the evolution of any filled state for a driving, A_α, and polarization, P_α, different from zero

$$\hbar\dot{\rho}_{ll}(t) = \sum_{vu} \left[\Gamma_{vl,lu}(t)\rho_{vu}(t) + \bar{\Gamma}_{vl,uv}(t)\rho_{ul}(t) - \Gamma_{lv,vu}(t)\rho_{lu}(t) - \bar{\Gamma}_{lv,ul}(t)\rho_{uv}(t)\right],$$

which can be rewritten as populations terms plus coherence ones

$$\hbar\dot{\rho}_{ll}(t) = \sum_{v} \left[\Gamma_{vl,lv}(t)\rho_{vv}(t) - \bar{\Gamma}_{lv,vl}(t)\rho_{vv}(t) + \bar{\Gamma}_{vl,lv}(t)\rho_{ll}(t) - \Gamma_{lv,vl}(t)\rho_{ll}(t)\right] +$$

$$\sum_{vu;v\neq u} \left[\Gamma_{vl,lu}(t)\rho_{vu}(t) - \bar{\Gamma}_{lv,ul}(t)\rho_{uv}(t)\right] - \sum_{vu;l\neq u} \left[\Gamma_{lv,vu}(t)\rho_{lu}(t) - \bar{\Gamma}_{vl,uv}(t)\rho_{ul}(t)\right].$$

[7] If we polarize an electrode above the Fermi level, the Rabi terms disappear in the population rate equation for a filled state. This left-right asymmetry is probably due to breaking the electron-hole symmetry by making $U \to \infty$.

The simplest case, $S = 0 \implies S_T = 1/2$, has three states: down $|1\rangle$, up $|2\rangle$, empty $|3\rangle$ with $m = 0$. So, the previous equation turns out to be:

$$\hbar\dot{\rho}_{11}(t) = \left[\Gamma_{31,13}(t)\rho_{33}(t) - \bar{\Gamma}_{13,31}(t)\rho_{33}(t) + \bar{\Gamma}_{31,13}(t)\rho_{11}(t) - \Gamma_{13,31}(t)\rho_{11}(t)\right] -$$

$$\left[\Gamma_{13,32}(t)\rho_{12}(t) - \bar{\Gamma}_{31,23}(t)\rho_{21}(t)\right]. \tag{2.62}$$

Redefining the rate proportional to the coherences as a frequency, a transition rate amplitude, and using the results of the rates found in Appendix F

$$\Omega^3_{12}(t) = 2\Gamma_{13,32}(t)/\hbar = -2\bar{\Gamma}_{31,23}(t)/\hbar =$$

$$\sum_{n'} e^{-in'\omega t}\left(\frac{1}{\hbar}\sum_{n\alpha\sigma}\left(\lambda_{13\sigma}\mu_{32\sigma}\frac{\Gamma'_\alpha}{2}(1+2\sigma P_\alpha)n_F(\Delta_{32}-n\omega)\left[\delta_{n,n'} + \frac{A_\alpha}{2}\left(\delta_{n,n'+1}+\delta_{n,n'-1}\right)\right] -\right.\right.$$

$$\left.\mu_{13\sigma}\lambda_{32\sigma}\frac{\Gamma'_\alpha}{2}(1+2\sigma P_\alpha)(n_F(\Delta_{23}-n\omega)-1)\left[\delta_{n,-n'} + \frac{A_\alpha}{2}\left(\delta_{n,1-n'}+\delta_{n,-n'-1}\right)\right]\right)\cdot$$

$$\left.\left[\delta_{n,0} + \frac{A_\alpha}{2}\left(\delta_{n,1}+\delta_{n,-1}\right)\right]\right).$$

The notation of Ω indicates we induced a rate between states $|1\rangle$ and $|2\rangle$ connected by the empty state $|3\rangle$. As a side note, we could have also rates between empty states by an up or down one that shares it both. Γ'_α is the full-polarized coupling constant and $P_\alpha = \delta_{\alpha,R}P_R$. Since $|3\rangle$ is an empty state we have that

$$\hbar\Omega^3_{12}(t) = \hbar\sum_{n'} e^{-in'\omega t}\Omega^3_{12;n'} = \sum_{n'} e^{-in'\omega t}\sum_{n\alpha\sigma}\mu_{13\sigma}\lambda_{32\sigma}\frac{\Gamma'_\alpha}{2}(1+2\sigma P_\alpha)(n_F(\Delta_{23}-n\omega)-1)$$

$$\cdot\left[\delta_{n,-n'} + \frac{A_\alpha}{2}\left(\delta_{n,-n'+1}+\delta_{n,-n'-1}\right)\right]\left[\delta_{n,0} + \frac{A_\alpha}{2}\left(\delta_{n,1}+\delta_{n,-1}\right)\right].$$

We can extract what we need in order to identify the Rabi frequency following the results of Bloch-Redfield theory for two level system, Eq. 2.23. Hence, we are looking for the term proportional to $\cos\omega t$. Taking the $n' = 1, -1$ terms in equation

$$\hbar\Omega^3_{12}(t) = \hbar\sum_{n'=0,-2,2} e^{-in'\omega t}\Omega^3_{12;n'} + \hbar e^{i\omega t}\Omega^3_{12;-1} + \hbar e^{-i\omega t}\Omega^3_{12;1},$$

we have

$$\hbar\Omega^3_{12;1} = \sum_{\alpha\sigma} \frac{A_\alpha}{2}\mu_{13\sigma}\lambda_{32\sigma}\frac{\Gamma'_\alpha}{2}(1+2\sigma P_\alpha)(\Delta_{23})\left[(n_F(\Delta_{23}+\omega)-1)+(n_F(\Delta_{23})-1)\right]$$

$$\hbar\Omega^3_{12;-1} = \sum_{\alpha\sigma} \frac{A_\alpha}{2}\mu_{13\sigma}\lambda_{32\sigma}\frac{\Gamma'_\alpha}{2}(1+2\sigma P_\alpha)(\Delta_{23})\left[(n_F(\Delta_{23}-\omega)-1)+(n_F(\Delta_{23})-1)\right].$$

If the terms $n' = -1, 1$ are equal, we can build a $\cos\omega t$. The condition for them to be equal can be satisfied by making the $E_{f_R} \gg \hbar\omega$ or, alternatively, if $\Delta_{23} \gg \hbar\omega$. In these two situations, the frequency is irrelavant in the Fermi functions so $\Omega^3_{12;1} = \Omega^3_{12;-1}$. Taking this into account, the Rabi frequency for a spin zero system is:

$$\hbar\Omega = \hbar\Omega^3_{12;1} = \sum_{\alpha\sigma} A_\alpha\mu_{13\sigma}\lambda_{32\sigma}\frac{\Gamma'_\alpha}{2}(1+2\sigma P_\alpha)(n_F(\Delta_{23})-1). \tag{2.63}$$

In addition to this, we could actually write

$$\Omega^3_{12}(t) = \sum_{n'} e^{-in'\omega t}\Omega^3_{12;n'} = \Omega^3_{12;0} + 2\Omega^3_{12;1}\cos\omega t + 2\Omega^3_{12;2}\cos 2\omega t.$$

Thus, we find the following evolution equation

$$\hbar\dot{\rho}_{11}(t) = \left[\Gamma_{31,13}(t)\rho_{33}(t) - \bar{\Gamma}_{13,31}(t)\rho_{33}(t) + \bar{\Gamma}_{31,13}(t)\rho_{11}(t) - \Gamma_{13,31}(t)\rho_{11}(t)\right] -$$

$$\hbar\left[\frac{\Omega^3_{12;0}}{2} + \Omega^3_{12;1}\cos\omega t + \Omega^3_{12;2}\cos 2\omega t\right](\rho_{12}(t)+\rho_{21}(t)).$$

For any spin S, we note that

$$\hbar\dot{\rho}_{ll}(t) = \sum_v \left[\Gamma_{vl,lv}(t)\rho_{vv}(t) - \bar{\Gamma}_{lv,vl}(t)\rho_{vv}(t) + \bar{\Gamma}_{vl,lv}(t)\rho^0_{ll}(t) - \Gamma_{lv,vl}(t)\rho^0_{ll}(t)\right] +$$

$$\sum_{vu;v\neq u}\frac{\hbar\Omega^l_{vu}(t)}{2}(\rho_{vu}(t)+\rho_{uv}(t)) - \sum_{vu;l\neq u}\frac{\hbar\Omega^v_{lu}(t)}{2}(\rho_{lu}(t)+\rho_{ul}(t)). \tag{2.64}$$

So we have a Rabi frequency transition for each coherence terms in Eq. (2.64). Also, notice that the second order terms in frequency $\Omega^3_{12;2}$ are proportional to A^2_α and they could create second order resonances if the driving is high enough. The zero order terms $\Omega^3_{12;0}$ exist at zero driving and they can be thought as energy renormalization terms.

Chapter 3

Results

This chapter encompasses all the results of the three methods explained in the theory. Firstly we check out what DFT provides about the system. Later we have the Multiplet results. Most of this work has been already published in [46, 75]. Finally we introduce the ESR Floquet simulations.

3.1 Density Functional Theory calculations

Here we introduce the DFT results. The calculations were performed using the pseudo potential method and plane-waves implemented in VASP. All pseudopotentials use the PAW_PBE parametrization for the exchange and correlation potential. The cut-offs for the expansion of the plane waves and charge density were chosen according to the pseudopotential verification database. Firstly, we focus on the bulk systems, follow by results on the MgO/Ag(001) slab. After that we present the calculations when we place the Fe impurity, computing the planar average potential for different electric force fields. Finally we compare the electric field response of MgO/Ag slab with Cu_2N/Cu and CuCl/Cu ones.

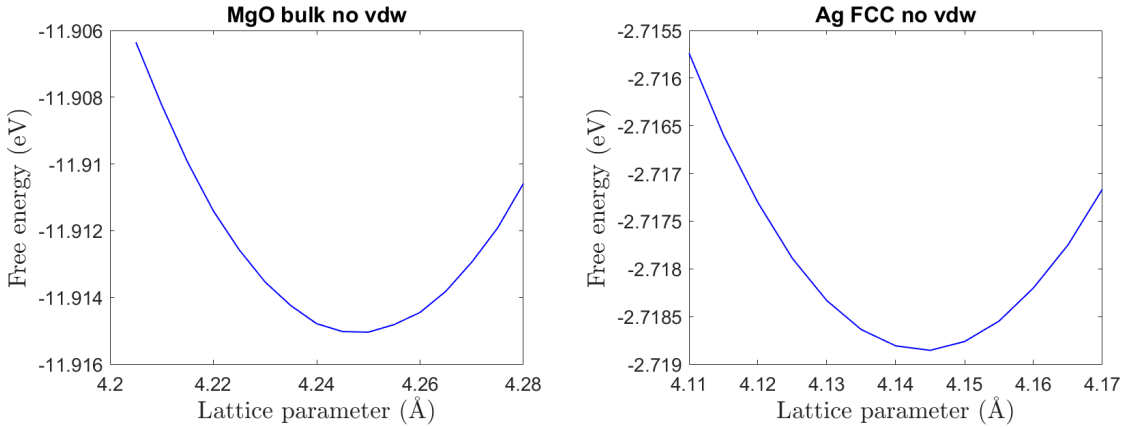

Figure 3.1: Free energy vs lattice parameter for Halite FCC MgO (left) and FCC Ag (right) using cut-off of the PAW_PBE pseudo potential, K-Points (Monkhorst Pack) grid of 11x11x11 and no Van der Waals corrections for both cases. For MgO one find a lattice parameter of 4.25 Å while in the Ag case we have 4.145 Å which results in a lattice mismatch of about 2.5% (experimental value: 2.9%).

3.1.1 Bulk systems

Since we are using pseudopotentials, it is more precise to make use of the lattice parameters that the simulation gives rather than taking the experimental values. Therefore, we calculate the bulk lattice parameters before we build any slab.

We introduce a cut-off energy and K-Points (Monkhorst Pack) appropriate and we look for the free energy as we change the lattice parameter obtaining Fig. 3.1 and 3.2. The first two plots are computed without the Van der Waals corrections while the second one add it. Clearly the Van der Waals force become essential to reach lattice parameter values closer to the experimental ones. In addition to this, the Van der Waals correction also helps to reproduce more precise results on work function, adhesion energies and interatomic distances for the slab systems.

3.1.2 Fe on MgO/Ag surface

Let us focus first on the surface system without the magnetic atom. With the information of the bulk, we are able to generate the slab structure with different number MgO layers.

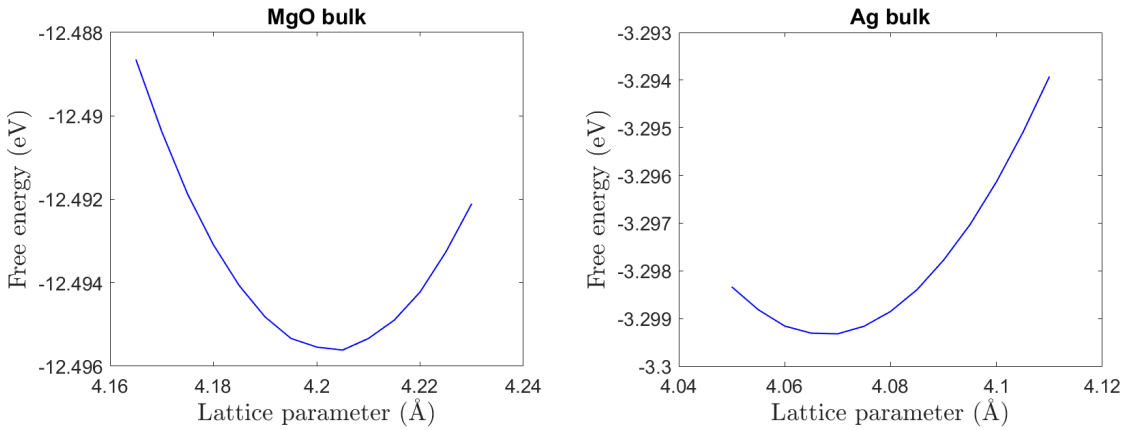

Figure 3.2: Free energy vs lattice parameter for Halite FCC MgO (left) and FCC Ag (right) using cut-off of the PAW_PBE pseudo potential, K-Points (Monkhorst Pack) grid of 11x11x11 and Van der Waals corrections for both cases. For MgO one find a lattice parameter of 4.205 Å while in the Ag case we have 4.075 Å which results in a lattice mismatch of about 3% (experimental value: 2.9%). Furthermore, the individual values of the lattice constants are closer to the experimental ones if the Van der Waals corrections are applied since experimentally $a_{MgO} = 4.212$Å and $a_{Ag} = 4.079$Å.

We chose the lattice constant of the silver because, in addition to correspond to the bulk Ag underneath, it is the lowest and ensures a better stability of the system. The unit cell is chosen to be 4 layers of Ag (001) plane with 8 atoms for each monolayer. In contrast, the MgO monolayers will have 16 atoms: 8 of Mg plus 8 of O and (001) plane is taken to match the Ag surface. Since the oxygen is more electronegative, we will place them over the silver atoms. The system is padded by ≈ 20Å of vacuum in the z-direction and a dipole correction was applied to decouple the slab from its periodic images and counterbalance its error. This is made by writing IDIPOL=3 and LDIPOL=.TRUE. in the INCAR file. The grid of K-points is decreased to 5x5x1 with respect to the bulk cases.

Once we built the surface, we relax the structure but maintaining the two bottom Ag monolayers frozen since they should not move a measurable quantity. After this, we added the magnetic impurity magnetic Fe atoms and performed a couple more relaxations while introducing an on–site Coulomb repulsion $U = 3.2$ eV and SPIN= 2 in the INCAR file. Only the d shell contribute to the magnetization. Fig. 3.3 shows how the final relaxed

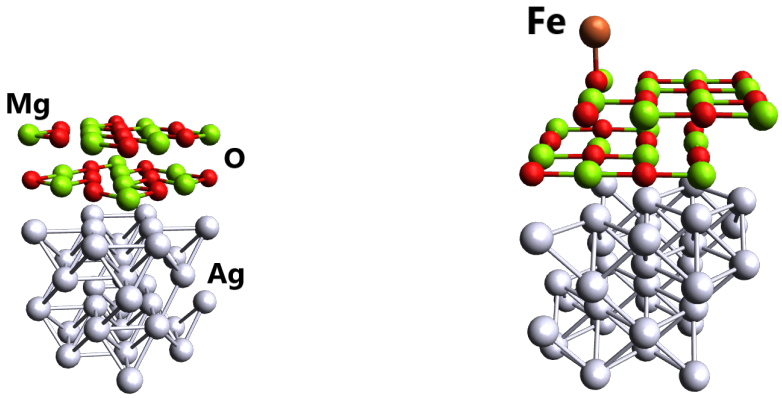

Figure 3.3: Relaxed surfaces with two MgO monolayers with (right) and without (left) the impurity atom. It can be noticed that the MgO/Ag(001) substrate without the magnetic impurity has really flat monolayers, the atoms fall in a plane. However, once we place the iron atom, the plane is a bit deformed and the oxygen underneath the iron is pulled up. This makes the pair $\mathrm{Fe} - \mathrm{O}$ hybridize.

structures look like for the two MgO monolayer case. We performed DFT calculations for one to four MgO monolayers in order to compute the adhesion energy for every case.

We define the adhesion energy as the energy required to break the Ag-MgO interface into isolated Ag and MgO (001) slabs. Therefore, the larger adhesion energy indicates the stronger binding of the interface:

$$E^{adh}_{interface} = E^{tot}_{Ag-Surf.} + E^{tot}_{MgO-Surf.} - E^{tot}_{MgO/Ag}. \tag{3.1}$$

Or, what is the same:

$$E^{adh}_{interface} = E^{tot}_{(MgO-1)/Ag} + E^{tot}_{MonoMgO-Surf.} - E^{tot}_{MgO/Ag}, \tag{3.2}$$

which basically tell us the adhesion energy is the energy of a MgO/Ag surface with one less MgO monolayer plus the energy of that isolated monolayer minus the energy of the total slab, respectively. Table 3.1 summarizes the adhesion energy results. The one ML MgO/Ag (001) shows the weakest binding of the interface, probably due to the dominant Pauli repulsive interaction between the Ag film and the MgO substrate [76]. Interestingly, 2 ML of MgO provides a close enough to saturation adhesion energy, which warranties a

	Without Fe			With Fe	
	E^{tot}_{slab} (eV)	$E^{adh}_{interface}$ (eV)	WF (eV)	d_{Fe-O} (Å)	Mag (μ_B)
MgO monolayer	-90.10	-	4.90	-	-
Ag 4 layers	-93.81	-	4.10	-	-
MgO(1L)/Ag(001)	-188.58	4.67	3.16	1.926	3.922
MgO(2L)/Ag(001)	-287.64	8.96	2.82	1.930	3.936
MgO(3L)/Ag(001)	-387.19	9.44	2.79	1.968	3.974
MgO(4L)/Ag(001)	-486.77	9.48	2.81	1.973	3.984

Table 3.1: Summary of the results for the different slabs with and without the magnetic atom. The adhesion energies seem to saturate as the MgO monolayers grow, being 2 ML rather enough to reach the saturation. Clearly the work function data reach also a stable behaviour as the number of MgO layers increase. Results on work functions and adhesion energy in agreement with [78] and [43]. The distances $\mathrm{Fe}-\mathrm{O}$ increase with the number of MgO monolayers (biggest jump from 2 to 3 ML). Same for the magnetization which is close to $4\mu_B$ for every case.

stable substrate. The table mentioned also provides results on the work function which are calculated by plotting the Planar Average-Potential vs Planar Distance and looking at the difference between the energy in the vacuum and the Fermi one. Additionally, we computed the $\mathrm{Fe}-\mathrm{O}$ distances and magnetization for each MgO monolayer.

The distances of the dimer $\mathrm{Fe}-\mathrm{O}$ increases with the number of MgO monolayers which could imply that the magnetic atom become less attached to the surface as the ML grows. The magnetization also increases and it is close to $4\mu_B$, $S = 2$, for every case. This was expected since we must recover the isolated value of the magnetization for magnetic Fe atom because MgO constitutes a very good insulator with an energy band gap of 7.2 eV [77]. Therefore, increasing the ML will lead to a effective isolated Fe.

After this analysis, we implement the electric field into our calculations. The VASP code gives us this option through the command EFIELD, which controls the magnitude of the applied electric field (eV/Å). Experimentally, the AC voltage goes from 10 to 60 meV. If we supposed that the STM tip is around 3-10 Å above the MgO substrate, we have an electric

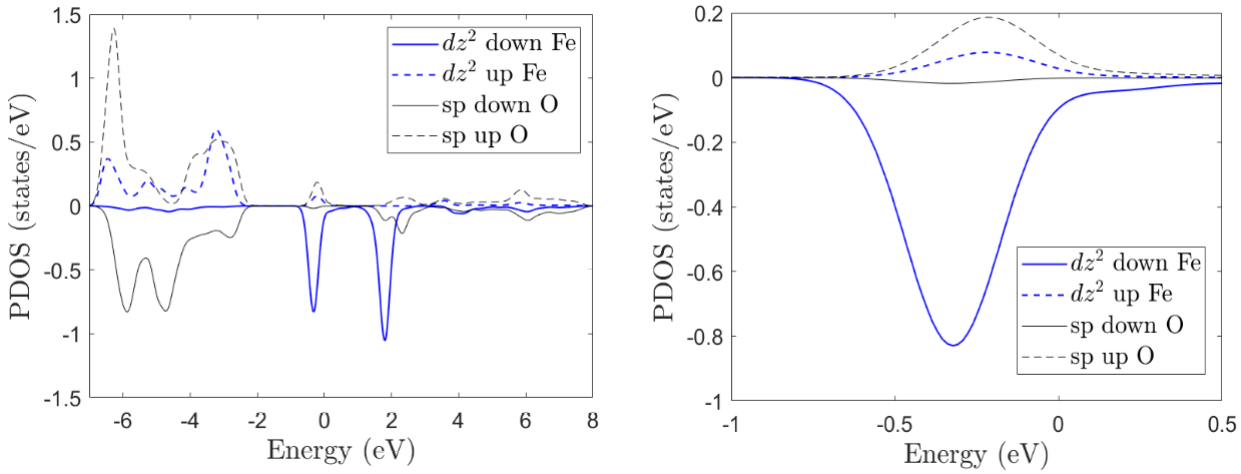

Figure 3.4: PDOS vs the energy for the d_{z^2} Fe orbital and the sp of the oxygen underneath it. The zoom plot (right) shows clearly the hybridization between both orbitals. Other d-orbital are much further from the Fermi level, $E_F = 0$, such that they cannot contribute to any excitation.

field of $F_E = 1 - 20$ meV/Å. With this information, we applied four electric-field values: $\{-0.002,\ -0.02,\ 0.02,\ 0.002\}$ eV/Å, and we look at the planar average potential and PDOS for the iron since they are likely to show an electric-field dependence. Particularly, we focus on the orbital d_{z^2} of the Fe because it is closer to the Fermi level, which is chosen to be zero. Other d-orbitals do not offer any relevant information. Fig. 3.4 shows the projected density of states for the Fe and O underneath. From the plot, since the d_{z^2} orbital hybridizes with the oxygen underneath, it can undergo a Stark effect. This property is characteristic of the s and p orbitals and implies a linear dependence on the electric field. Therefore, at first glance, an electric field could move the d_{z^2} density of states up or down in energy changing the effective configuration of the magnetic impurity ($d^6 \rightarrow d^7$ or d^5). This implies a change of the tunneling amplitudes which translates into an effective Rabi term and the consequent resonance peak in the current spectrum. However, from Fig. 3.5, one sees that the adatom-level shifts are negligible under the applied external electric fields.

The planar average potential (PAP) results on Fig. 3.6 provides a measurable change on the electric field. There we plot the PAP with respect to the zero-field case and it can

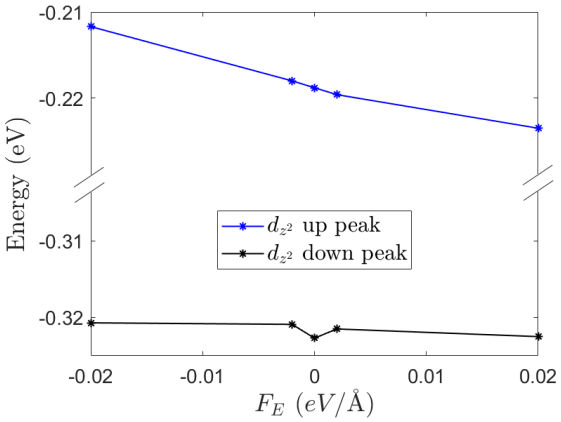

Figure 3.5: Energy peak position near the Fermi level for Fe vs the electric field. The energy shifts are negligible for the experimental values of the electric field.

be noticed a maximum difference in the PAP of 0.7 eV in the vacuum region. As we get closer to the substrate, each line converges to zero, which means that the electric field is being screened. This is due to MgO being a polar insulator with a very large dielectric constant. However, notice that at the Fe's position there is still an electric force remaining which could move the magnetic impurity. In any case, the large change in the potential barrier implies the prevalence of the modulation of the tunnel barrier, similar to the case of inelastic tunneling spectroscopy (IETS). This modulation could provide the existence of Rabi terms and, therefore, ESR peaks in the current spectra. In section 3.2 we apply this idea while using a cotunneling/multiplet approach to the problem.

3.1.3 Cu_2N and CuCl comparison

Since many works have been published using Cu_2N substrate [79, 80] and the system CuCl could provide better ESR signals, we wanted to see how these surfaces are affected by an electric field. We computed the Cu lattice constant looking at the minimum free energy in the bulk system and followed relaxation steps similar to the one we made in the MgO/Ag(001) case. Fig. 3.7 shows the relaxed structures.

A rather simple calculation was made to compare the responses of each slabs. We applied four electric-field values: $\{-0.002,\ -0.02,\ 0.02,\ 0.002\}$ eV/Å and looked at the total force

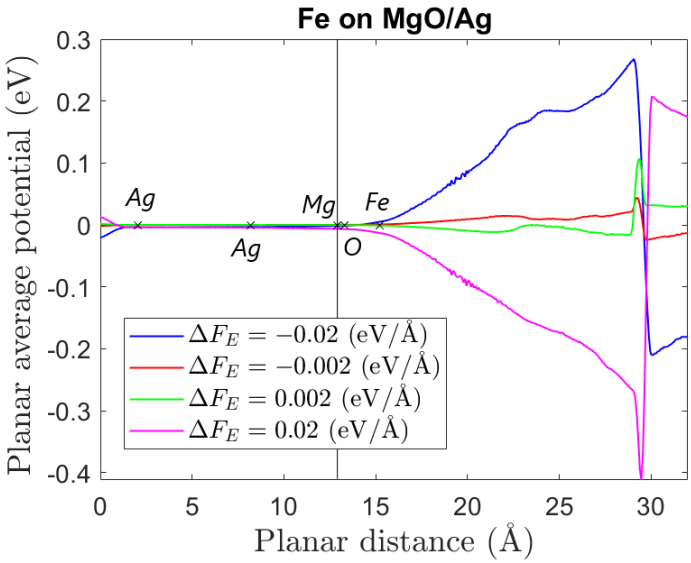

Figure 3.6: Planar average potential (PAP) with respect to the zero-electric-field case vs planar distance. $\Delta F_E = F_E - F_{E_0}$ where F_{E_0} refers to the PAP with zero-field applied. Clearly the electric field shifts the potential in the vacuum region, which translates into a large modulation of the tunneling barrier (assuming that the tip position is ~ 10 Å above the insulator). At a larger distance, we have a plane of dipoles added in the vacuum region needed to have an increasing potential due to a constant external electric field in the unit cell of the calculation (from the dipole correction VASP implementation IDIPOL=3). The $\times$ marks indicate the atom and plane position of the slab. The magnetic impurity, Fe, is at 15.2 Å while the O underneath is at 13.27 Å. This atom has been pulled out of the second MgO layer, at 12.89 Å, due to the interaction with the Fe. We also place the first and last Ag layers at 8.16 Å and 2.03 Å, respectively. The vertical line at 12.91 Å marks the position of the second MgO plane before we place the magnetic impurity. Therefore, Mg atoms in the surface do not feel as much change as the O underneath the magnetic atom.

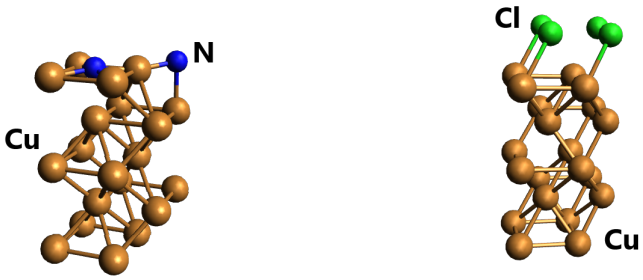

Figure 3.7: Relaxed structures for the Cu_2N/Cu(001), left, and CuCl/Cu(001), right.

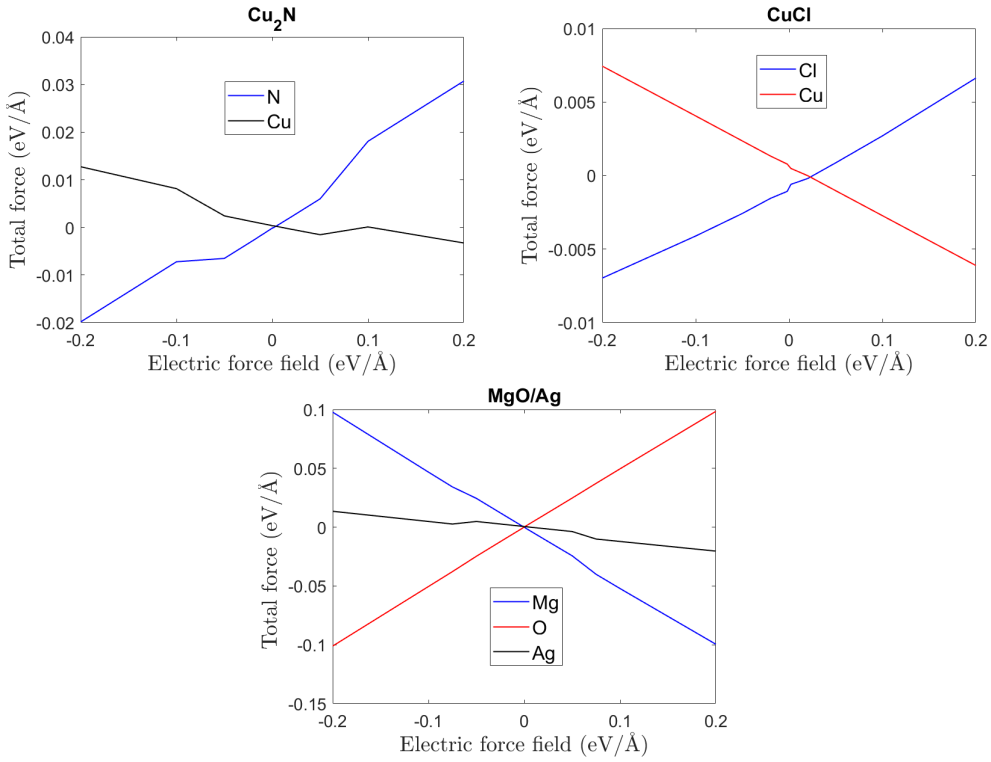

Figure 3.8: Total force vs the electric field for every substrate discussed. For each species we took the atom in the most top layer. All the atoms of one species in the same layer feel the same total force. One can notice that the MgO layer feels a force that is one order of magnitude larger than the Cu_2N and CuCl surfaces.

that every atom felt without making a relaxation procedure. Fig. 3.8 provides the results. Although these calculations are performed at a precision lower than the above results, it provides enough inside of the surfaces. They show an order-of-magnitude less in the force exerted by the external field on the surface atoms for the Cu_2N and CuCl in comparison with the MgO/Ag slab. This implies a smaller piezoelectric effect for the above to surfaces as compared to the MgO-based system. Therefore, in order to have a strong ESR signal, a MgO/Ag substrate is preferable.

3.1.4 Conclusions of the section

We have built our slab system using the lattice parameters that minimize the free energy of the bulk systems, together with other considerations such as the number of k-points or the values of the cut-off energies. We have shown that as more MgO monolayers are added to the Ag surface, the system becomes more stable. However, two MgO layers already provide a large enough adhesion energy and stability to be grown easily, in agreement with experiments [7, 11, 12, 13, 14, 15, 16, 17].

Then, we have placed the magnetic impurity Fe above one of the top O and computed the PDOS for both atoms. The results clearly show a hybridization of the d_{z^2} orbital with the sp one of the O. Since the sp orbitals feel the presence of an electric field by the linear Stark effect, we performed calculations on the substrate for different electric fields. Even though there are Fe levels close to the Fermi level, a static electric field cannot change the electronic configuration of the magnetic atom. However, it greatly modifies the tunneling barrier. Hence, we can conclude that the electric field is strongly modulating the tunneling barrier .

This modulation is also reflected in the total force that each atom feels. One can notice that the MgO layer feels a force that is one order of magnitude larger than the Cu_2N and CuCl cases, which could be the reason why the latter systems do not display ESR signals, at least for the time being.

3.2 Time-dependent cotunneling results

Here, we present the results of the time-dependent cotunneling approach. We mainly focus on the current and Rabi frequency. We shall show that our description leads to a considerable agreement with the experimental results despite some assumptions. All the results in this section are computed using a Multiplet calculation to solve a many-body Hamiltonian, more details can be found in Appendix A. Although the code can use Maximally Localized Wannier Functions [75], in this section we keep the simpler description of the crystal field based on a point-charge model [81]. Despite the quantitative limitations of these models, they provide a good picture of the symmetry of the system, so they are very often used to describe ESR spectra [55].

In our modelling, Sec. 2.2.2, the consequence of the AC driving voltage is summarized in the non-equilibrium occupations $P_a(V, \omega)$ but, more explicitly, on the Rabi frequency or flop rate Ω, given by Eq.(2.34). We underline that, in order to arrive to this expression, we made the assumption of considering constant density of states and hybridization with the leads. As a consequence, we need to introduce an energy cut-off E_c to have definite integrals. These raw approximations will enable us to estimate the Rabi flop-rate and the ESR current response easily. Moreover, the predicted behavior of the results are in qualitative agreement with the experimental ones. On the down side, our approach overestimate the Rabi frequency by one order of magnitude as we will see.

We first introduce the current detection mechanism emulating experimental conditions for a TLS. Then we illustrate the main results for two cases: a *single orbital Anderson Hamiltonian* and the *multiorbital case* describing the Fe on MgO/Ag(001) surface. In the former, the only ingredients are the charging energy of the adatom and the induced Zeeman splitting. In the second case, we describe the magnetic adatom by a multiorbital Hubbard model that includes the Coulomb repulsion between the impurity d-electrons, the crystal field calculated by a point-charge model [81], the spin-orbit coupling and the Zeeman term [57, 82]. In doing so, we will assume hydrogenic-like wavefunctions for the Fe orbitals. The Coulomb interaction is parametrized by a single parameter, the average on-site repulsion U. The resulting crystal field depends on two parameters: the expectation values $\langle r^2 \rangle$ and

$\langle r^4 \rangle$ [81], while the spin-orbit coupling will be defined by its strength ξ_{SO}. Specific details about the used parameters can be found in the Appendix Sec. A.2 and Table A.1.

Current detection of the STM-ESR

In Sec. 2.2.2 we have sketched the cotunneling mechanism leading to the STM-ESR. Equation (2.25) makes explicit the working mechanism of the experiment: the occupations $P_a(V, \omega)$ respond to the driving frequency and the changes are reflected in the DC current $I(V, \omega)$. The consequences on the current and occupations can be seen in Fig. 3.9. This figure illustrates the magnetoresistive detection mechanism. Here we have used a two-level description where the steady-state density matrix population is given by Eq. (2.26).

We have used the parameters extracted from Baumann *et al.*: [7] $T_1 \approx 88$ μs, $T_2 \approx 200$ ns, $\Omega \approx 2.6$ rad/μs. In addition, we take a set-point current of $I = 0.56$ pA at $V_{DC} = 5$ mV, while we assume a tip polarization $P_T = 0.33$ that is close to the one experimentally estimated [14]. The finite tip polarization leads to a magnetoresistive response: the electrons tunneling rates depend on the relative orientation between the local spin and the tip magnetization, together with the sign of the applied bias [83, 84].

Furthermore, close to the resonant frequency, the occupations of the two low-energy states tend to balance, as observed in the right inset of Fig. 3.9. This change of $P_m(V, \omega)$ is then reflected as a change in the DC current detected by the STM.

3.2.1 Single-orbital Anderson model

A single-orbital $S = 1/2$ spin model

We start discussing the simplest model for a magnetic impurity: the single-orbital Anderson model. This model, which was introduced to describe magnetic impurities on a non-magnetic metal host [85], is equivalent to a single $S = 1/2$ spin exchange coupled to conduction electrons [86]. Then, it may be used as an idealization of the STM-ESR experiments on hydrogenated Ti atoms on MgO/Ag(001) [15, 16]. The $S = 1/2$ spin is isotropic, and the matrix elements $\gamma_{ab}^{m^\pm}(\sigma\sigma)$ can be evaluated analytically, with $\gamma_{ab}^{m^\pm}(\uparrow\uparrow) = -\gamma_{ab}^{m^\pm}(\downarrow\downarrow)$.

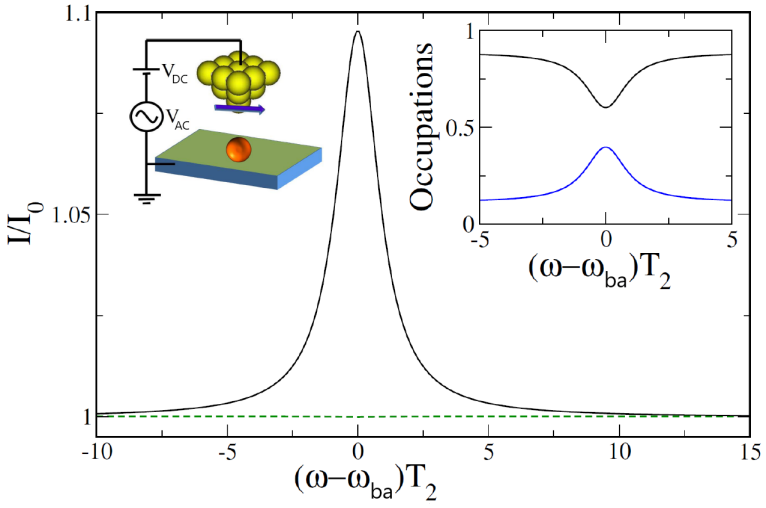

Figure 3.9: Current detection of STM-ESR. Variation of the DC current as a function of the detuning $\omega - \omega_{ba}$ in units of $1/T_2$, with $\omega_{ba} = (E_b - E_a)/\hbar$ for $P_T = 0.33$ (black) and $P_T = 0$ (green dashed line). The current is given in terms I_0, the DC current far from resonance. In the left inset we have the scheme of the STM-ESR setup: a radio-frequency bias voltage is applied in addition to the DC voltage between the spin-polarized tip and the surface. On the right inset we find the variation of the occupation of the ground state, $|a\rangle$, (black) and first excited state, $|b\rangle$, (blue) with detuning. The different parameters are chosen to match the conditions of Fig. 3(C) in Baumann *et al.* [7] with $V_{AC} = 8$ mV.

Let us consider that the system is under the influence of a static magnetic field B_x, so that $|a\rangle$ and $|b\rangle$ are eigenvectors of the spin operator $\hat{S}_x$ and $g\mu_B B_x = \hbar\omega_0$ is the Zeeman splitting. Then, assuming that only the tip is spin polarized and using the same notation as in Eq. (2.34), one gets that $\Lambda_{m_-,\alpha} + \Lambda_{m_+,\alpha} \propto V_T^2 P_T \delta_{\alpha,T}$, where V_T is the hopping between the single level and the tip. In other words, only coupling with a spin-polarized electrode gives a finite contribution to Ω. When the value of the hybridization function $\Gamma'_T = 2\pi\rho_T V_T^2$ is much larger than the thermal energy $k_B T$, where T is temperature and k_B is the Boltzmann constant, one can approximate the Rabi frequency by

$$\Omega \approx \frac{e\Gamma'_T\,|V_{AC}P_T|}{h|\delta_{ab}|}\left|\mathcal{I}^-(\mu_-, E_c, eV) - \mathcal{I}^+(\mu_+, E_c, eV)\right|, \tag{3.3}$$

where the functions $\mathcal{I}^{\pm}(\mu_{\pm}, E_c, eV)$ are defined in Appendix B.

Crucially, the result above relies on the fact that the tip polarization is normal to the magnetic field producing the Zeeman splitting, leading to a finite mixing between the eigenvectors $|a\rangle$ and $|b\rangle$. This should not be surprising since in the standard ESR protocols [55], the AC magnetic field is applied perpendicular to a large static field. In our case, the AC electric field yields an effective oscillating magnetic field along the tip polarization direction z, which is on resonance with the Zeeman splitting produced by the applied static magnetic field B_x.

The result (3.3) has a different reading: the proposed mechanism does not need any particular anisotropy. The key ingredient is thus the effective magnetic field created by the spin-polarized tip, $B^{\text{eff}} = 2\hbar\Omega/g\mu_B$, which is oriented along the tip-polarization direction. In order to have an active ESR signal, this effective field must have a component perpendicular to the field inducing the Zeeman splitting.

A single-orbital multispin model

In general, transition metal adatoms entails $S \geq 1/2$ spins, and thus, they are also subjected to magnetic anisotropy. The dominant interaction with their surroundings takes the form of an exchange coupling [87, 88], which determines the IETS, and the spin relaxation and decoherence [29]. Hence, the total spin, given by the sum of the local spin and scattering electrons spin, is conserved. Thus, we can model this interaction in the cotunneling

context by considering the scattering of the itinerant electrons with a localized magnetic impurity described by a single-orbital state, with a spin $S > 1/2$ (multiplicity $(2S+1)$) in its N_0 electrons state, and isotropic spins $S_{m_+} = S + (-1)^{c_+}/2$ and $S_{m_-} = S - (-1)^{c_-}/2$ in the charge states M_+ and M_-, which implies that the sum over m_- and m_+ in Eq. (2.35) vanishes. Constants c_+ and c_- can take the values 0 or 1 depending on the total spin total of the charge states.

The model sketched above allows us us to describe the effective exchange interaction $J_{\eta\eta'}$ in terms of the transition amplitude operators $\hat{T}_{\pm}(\eta\eta')$. In addition, it permits relating the Rabi flop rate, Eq. (2.34), with the local spin S. While the energy dependency is the same that appears in the single Anderson model, the crucial differences are associated to $\sum_{m_\pm,\sigma} \Lambda_{m_\pm,\alpha}$, see Eq. (2.35). Using the result of Appendix C, one can arrive to [89]

$$\Lambda_{m_-,\alpha} + \Lambda_{m_+,\alpha} \propto \Gamma'_T P_T \delta_{\alpha,T} \langle a|S_x|b\rangle \left(\frac{(-1)^{c_-}}{2S+1+(-1)^{c_-}} + \frac{(-1)^{c_+}}{2S+1} \right).$$

Therefore, we have the following expression of the Rabi frequency

$$\Omega \approx \frac{2e\Gamma_T\,|V_{AC}P_T|}{h|\delta_{ab}|} \langle a|S_x|b\rangle \left(\frac{(-1)^{c_-}}{2S+1+(-1)^{c_-}} + \frac{(-1)^{c_+}}{2S+1} \right) \left| \mathcal{I}^-(\mu_-, E_c, eV) - \mathcal{I}^+(\mu_+, E_c, eV) \right|. \tag{3.4}$$

Thus, our model predicts a weak dependence with the atomic spin, in good agreement with the observation of STM-ESR weak dependence on the atomic species [7, 11, 12, 13, 14, 15, 16, 17].

An important detail of our results is that the Rabi flop rate is proportional to the tip polarization and the hybridization, $P_T\Gamma_T$. Hence, it leads to $\Omega \propto I$, which is in apparent contradiction with the experimental observation of a Rabi flop independent of the DC current for the Fe on MgO/Ag(001) [14]. With this in mind, we examine below the corresponding results based on a multiorbital Hubbard model within the cotunneling description.

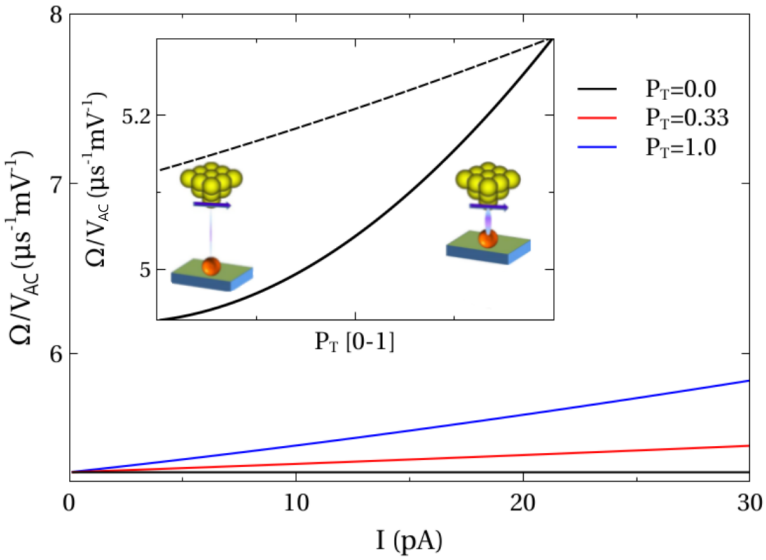

Figure 3.10: Estimation of Ω/V_{AC} for the Fe on MgO/Ag(001) substrate versus the DC current for a constant applied bias voltage $V_{DC} = 60$ mV. Each curve corresponds to a different tip polarization P_T. The inset shows the dependence with the tip polarization for the *high* (thick solid line) and *low* (thin dashed-line) DC voltages.

3.2.2 The Fe on MgO/Ag(001) surface

Although STM-ESR has been demonstrated on a variety of magnetic adatoms [7, 11, 12, 13, 14, 15, 16, 17], the most studied system is Fe on MgO/Ag(001) [7, 11, 12, 14]. As we mentioned, we are going to apply a simple point-charge model since it offers qualitative agreement results with the experimetal ones [90]. For the Ag(001) surface we have [59] that $m^* = 0.99m_e$ and $k_F \approx \kappa_F \approx 1.1$ Å^{-1}. Typical tunneling current measurements are given in a range where $\kappa L \sim 3 - 20$, which translates into $|\delta_{ab}^{-1}| \sim (0.3 - 2.1) \times 10^{-3}$ meV^{-1}. For simplicity, we assume that all Fe-d orbitals are equally coupled to the substrate, with an energy broadening $\Gamma_S \equiv 2\pi\rho_S|V_S|^2$. In the case of coupling to the tip, we assume that only the d_{z^2} is actually coupled, since it points towards the tip, with an induced energy broadening $\Gamma_T \propto I$.

To check our model, we first take $\Gamma_S = 2.314$ eV to fit the decoherence time, obtaining $T_2 = 210$ ns for the conditions of Fig. 3C of Ref. [7] at a driving voltage of 8 mV. Our cotunneling description then predicts a relaxation time T_1 of the Zeeman-excited state

of $T_1 = 8.72$ ms, to be compared with the experimentally determined $T_1^{Exp} = 88$ μs. The disagreement between both values can have two origins. On one side, we have the limitations due to the oversimplified point-charge model, together with the critical and different dependences of T_1 and T_2 on the magnetic anisotropy parameters. On the other side, this transition may also be mediated by the spin-phonon coupling [10]. Fortunately, our STM-ESR mechanism does not strongly depend on T_1.

We now turn our attention to the Rabi flop-rate, evaluated according to Eq. (2.34). The energy integration is done as in Eq. (3.3), and the only difference comes from the matrix elements $\Lambda_{m^\pm,\alpha}$. In this case, the sums over $m^\pm$ are extended over all states needed to guarantee the convergence. Figure 3.10 shows the DC current dependence at $V_{DC} = 60$ mV of the Rabi flop-rate for three different tip-polarizations: $P_T = 0,\ 0.33$ and 1, the ideal half-metal case. As observed, especially for intermediate polarizations, Ω is barely affected by the current. This striking result is in agreement with the experimental findings that shows a current-independent Rabi flop rate for currents between 10 pA and 30 pA, [14] where authors found that $\Omega/V_{AC} \approx 0.375$ rad.μs^{-1}.

The result above points out to a crucial ingredient that is not accounted for in the single-orbital Anderson model: the complex orbital structure of the adatom. According to Eq. (2.35), electrons tunneling into different orbitals ℓ of the adatom will lead to unequal contributions to the Rabi flop-rate. The direct consequence is that, contrary to the single-orbital case, the spin averages $\sum_{m_\pm,\sigma} \Lambda_{m^\pm,\eta\sigma}$ remains finite, which translates into a finite Rabi flop rate at zero current polarization, see inset of Fig. 3.11. The weak current dependence appears then as a direct consequence: Ω contains a fix contribution associated to hybridization with the surface, proportional to Γ_S, and another one of the tip, proportional to Γ_T ($\propto I$). Since $\Gamma_S \gtrsim \Gamma_T$ except for high conductances [10], the current independent contribution generally dominates. Comparing the polarization dependence for *low voltage*, with a current set-point of 0.56 pA at $V_{DC} = 5$ mV, and *high voltage*, with a current of 30 pA at $V_{DC} = 60$ mV, we notice that the Rabi frequency is not strongly affected by the dynamics of the excited spin states, see Fig. 3.10. A key issue is the apparent contradiction of our finite Rabi flop-rate for zero-polarization with the observation of the STM-ESR signal only when a spin-polarized tip is used. The solution to this apparent discrepancy is in the

detection mechanism of the ESR: current magnetoresistance. This is illustrated in Fig. 3.9, where we have added the frequency response when a spin-averaging tip is used, assuming exactly the same Rabi flop rate. The resulting steady state current is independent of the frequency and thus, there is not STM-ESR signal.

Willke *et al.* analyzed in detail the role of the different parameters that controls the STM-ESR [14]. In particular, they observed that the resonant peak current saturates with the radio frequency voltage V_{AC}, both for small and large set-point currents. In fact, they found that the ratio $I_{peak}/I_{sat} = \psi(V_{AC})$, which they called *drive function*, was given by $\zeta^2/(1+\zeta^2)$ with $\zeta = V_{AC}/V_{1/2}$, where $V_{1/2} = (T_1T_2)^{-1/2}V_{AC}/\Omega$ is defined as the half-saturation voltage. The relevance of this drive function is that, the larger the drive function, the larger the ESR signal, making the detection more efficient. Thus, we show in Fig. 3.11a) the drive function obtained from our model, which should be compared with Fig. S2C of Ref.[14]. Our theory correctly reproduce the general trend with the tunnel current. However, due to the overestimation of T_1 and Ω, our estimated driving function saturates at lower AC bias voltages.

Finally, we would like to call the attention on one point. The experimental observation of the STM-ESR signal requires a finite in-plane magnetic field B_x. In Ref. [7], authors argue that this field introduces a mixing between the states a and b, the same argument that we exploited in our $S = 1/2$ spin model of Sec. 3.2.1. From our expression of the Rabi flop-rate, Eq. (2.27), we see that its effect is the same as the one produced by a transversal AC magnetic field $B_\perp^{\text{eff}} = 2\hbar\Omega/g\mu_B$ on a $S = 1/2$ spin system under the action of an static field $B_\parallel^{\text{eff}} = \hbar\omega_{ba}/g\mu_B$. Hence, the application of a static field that mixes the zero-field states $|a^0\rangle$ and $|b^0\rangle$, as it is the case of the Fe/MgO [7], and the coupling term $\text{Tr}_R[\delta\hat{\mathcal{H}}_{cotun}]$, leads to the same consequence: a mixing of the low energy states $|a\rangle$ and $|b\rangle$, and thus, to a larger Rabi flop-rate. This is illustrated in Fig. 3.11b) where we show how Ω changes with a transversal magnetic field. From the experimental point of view, the static transversal field B_x is also required in order to have a finite tip polarization.

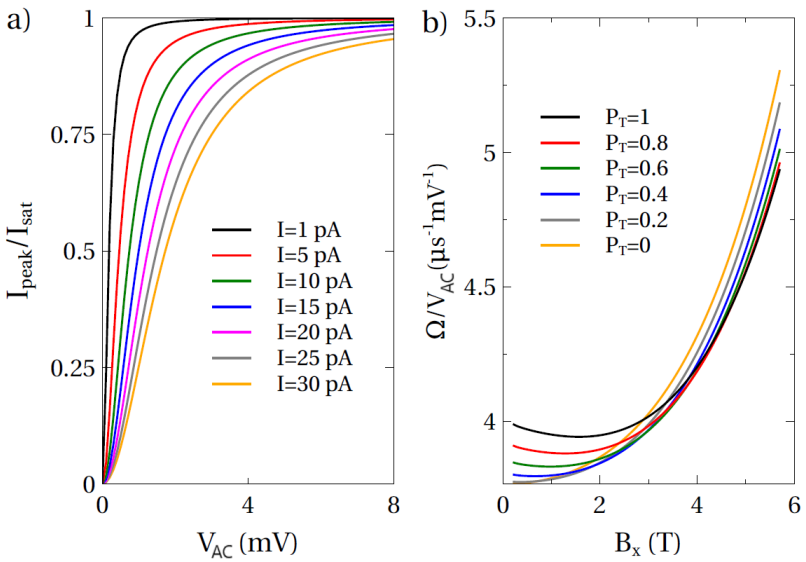

Figure 3.11: a) Predicted driving function I_{peak}/I_{sat} for the Fe/MgO/Ag(100) system for different currents, to be compared with Ref. [14]. b) Variation of the Rabi flop-rate, Ω, with the external in-plane field B_x for different values of tip polarization. The field is applied forming an angle $\theta = 3.51 \times 10^{-2}$ with the surface plane, with $B_z = 0.2$ T, while $I = 30$ pA and $V_{DC} = 60$ mV.

3.2.3 Conclusions of the section

We have analyzed the effect of an applied radiofrequency bias voltage on the DC tunneling current through a magnetic adatom. Our basic assumption is that this driving voltage leads to a modulation of the tunnel junction transmission with the time-dependent external electric field. In other words, the hopping tunneling amplitudes are modulated, giving place to an off-diagonal time-dependent term in the adatom's Hamiltonian which takes the form of the Rabi flop rate. This contribution mixes the stationary states.

The amplitude of the modulation was estimated using Bardeen transfer Hamiltonian theory to describe the tunneling current [26] which provide results in quantitative agreement [91]. A clear improvement over this simple description would be in the form of the Tersoff-Hamann description of tunnel between a surface and a probe tip [92].

The effect of the driving field is summarized in the single parameter called Rabi frequency or flop-rate, Ω. Thus, all our efforts in this section have been oriented to estimate Ω. In doing so, we keep a second-order description of the interaction of the quantum system (the adatom) with the electronic baths (surface and tip electrons), using the Bloch-Redfield approach to treat open quantum system [47]. In addition, we assume that the small and fast-oscillating driving field does not modified the dissipative dynamics [51].

This theory have been applied on two different models to simulate the STM-ESR mechanism. In first place, to a single-orbital Anderson model, which reveals that isotropic $S = 1/2$ systems can be ESR active with a Rabi flop rate proportional to the tip polarization. Thus, the proposed mechanism does not rely on a particular symmetry of the adsorbed adatom, neither on the adatom magnetic anisotropy or total spin. This ubiquity is in agreement with the experimental observation of STM-ESR for a variety of adatoms adsorbed on MgO, [7, 11, 12, 13, 14, 15, 16, 17] including the Ti-H complex behaving as a $S = 1/2$ spin [12, 15, 16]. The resulting Rabi flop-rate depends on off-diagonal matrix elements mixing the two states connected by the ESR, and thus, it can be described as an effective AC magnetic field $B_{\perp}^{\text{eff}} = 2\hbar\Omega/g\mu_B$, whose orientation is parallel to the tip-polarization. This is similar to the usual ESR where the AC field is perpendicular to the field creating the Zeeman splitting, and explains the need of an in-plane magnetic field in

the experiments of Baumann *et al* [7].

Since Ω is directly proportional to the tip polarization, a null contribution of the spin-unpolarized surface to the Rabi flop rate, which in turn leads to a linear dependence on current. Although a current dependence for $S = 1/2$ systems has not been reported to the best of our knowledge, this result is in contrast with the observation of a current-independent Rabi flop rate for Fe/MgO [14]. Hence, we employed a more sophisticated description of the adatom in terms of a multiorbital Anderson Hamiltonian derived from a multiplet calculation. This model already pointed to an important result: when the orbital degrees of freedom of the adatom are accounted for, the modulation of the tunnel barrier by the AC electric field generates a finite Rabi flop rate even in the absence of current polarization. Due to the usually dominant contribution of scattering with surface electrons, the contribution associated to the surface overshadow the (current-dependent) tip part. This result is thus in agreement with the observed weak current dependence [14].

Finally, despite the limitations of the approximations we performed, the Rabi flop-rates are high enough to explain the observation of ESR signals, but the values are off the experimental ones by a factor 10-20 [14]. In order to improve these results in the cotunneling scheme, we can use Wannier representation to compute the hybridization functions $V_{k;\ell}$, together with the PDOS $\rho(\epsilon)$ on the whole energy interval [75]. It is worthy to mention that an accurate description of the ESR-lineshape also involves the relaxation T_1 and decoherence T_2 times of the atomic spin. Therefore, a better knowledge of these parameters can also improve the results. Our modelling of the ESR experiments using Floquet theory provides this information naturally as we saw in Sec. 2.3.3.

3.3 ESR Floquet simulations

In the theory section 2.3.1, we presented a simple model to reproduce the experimental situation often found in ESR-STM. In ESR-STM, the tip and the substrate are biased with a constant plus an alternating voltages. The tip is spin polarized, and an external magnetic field is applied. Our model consists of a single active electronic level of an atom, molecule or quantum dot (QD) that is coupled to two electrodes representing tip and substrate. In order to capture the complexity of the system while keeping the electronic description simple, we have the single electronic level interacting via an exchange interaction (with coupling J) between the level spin, $\mathbf{s}$, and the rest of the electrons, represented by a local spin $\mathbf{S}$. Our QD is then a system of total spin $\mathbf{S}_T = \mathbf{S} + \mathbf{s}$. In order to approximate the experimental situation, we further include a spin-Hamiltonian by means of magnetic anisotropy on the total spin, as well as an external magnetic field, $\mathbf{B}$. This simple model can actually reproduce the main features of ESR of most atoms experimentally analyzed, thus giving us a way to peer into the intricate spin dynamics of ESR-STM.

ESR Floquet theory can provide really complicated results as the size of the local spin, S, increases. In order to make everything more transparent to the reader, we restrict ourself to two cases: (i) $S = 0$, which implies a total $S_T = S + s = 1/2$, and (ii) $S = 1/2$, with a spectrum given by two total spins, $S_T = 0$ and $S_T = 1$, by choosing the exchange coupling, J, we can explore the ESR transitions of the $S_T = 1$ system or of the more complex situation with both spins.

In (i), due to our approximation of large charging energy, the QD can only have three many-body states, corresponding to two occupied levels (spin up and down) and an empty level, see the scheme of Fig. 3.12. The QD Hamiltonian, Eq. (2.37), is given by the energy of the conduction electrons of the impurity of the down and up states plus the external magnetic field. The magnetic anisotropy, D, and the exchange coupling, J, can be set to zero because $S = 0$. Only the magnetic field is able to break the degeneracy of the down and up spins. It will also provide the resonance energy or Larmor frequency equal to the Zeeman energy difference between spins up and down. The total dimension of the Floquet problem is then 3 times the Floquet numbers.

The (ii) case presents some interesting scenarios. On one hand, it can reproduce the experimental situation of two coupled half-integer spins [93] and [15]. On the other hand, it can provide the situation of a total spin 1. The J value compared to other energy parameters will lead to the first or second case. It will be discussed later. The total dimension of the Floquet problem in this case is the size of the QD basis set, given by the three possible states of the electronic level times the multiplicity of the local spin, *i.e.* $3 \times (2S + 1) = 6$, times the Floquet numbers.

3.3.1 One-half total spin, $S_T = \frac{1}{2}$, or zero local spin, $S = 0$, case

Scheme and outline of the simulations

Figure 3.12 shows an energy-level scheme of the local-spin zero system when the energy of the occupied electronic levels of the impurity ε_σ are negative. This scheme shows the theoretical model for the case of local spin $S = 0$, which reduces to the single electronic level in the impurity. This is effectively a one-half total spin system if the average occupation of the impurity is close to one. To render this occupation possible, ε_σ are taken spin independent, negative and larger than the level broadening due to the hybridization with the electrodes, $\Gamma_{L,R}$.

Figure 3.12 a) and b) show the one-electron energy diagram giving the parameters that would control transport in a one-electron process. However, the large charging energy of the QD ($U \to +\infty$) only permits occupation below or equal to one electron, creating the scenario of many-body electron process. The corresponding cotunneling events can be considered by studying the many-body configurations of the QD in comparison with the applied bias. To simplify we assume large bias and a symmetrical drop such that the QD empty state, resonant to the zero-temperature Fermi energies, is always at the midpoint between Fermi energy levels as the bias increases. Figure 3.12 c) shows the three possible energy states of the QD. State $|1\rangle$ corresponds to a spin down in the QD, assuming a magnetic field such that the spin down is aligned with it, the level is the lowest one. State $|2\rangle$ is the spin up separated in energy from state $|1\rangle$ by the Zeeman energy. The empty state is state $|3\rangle$.

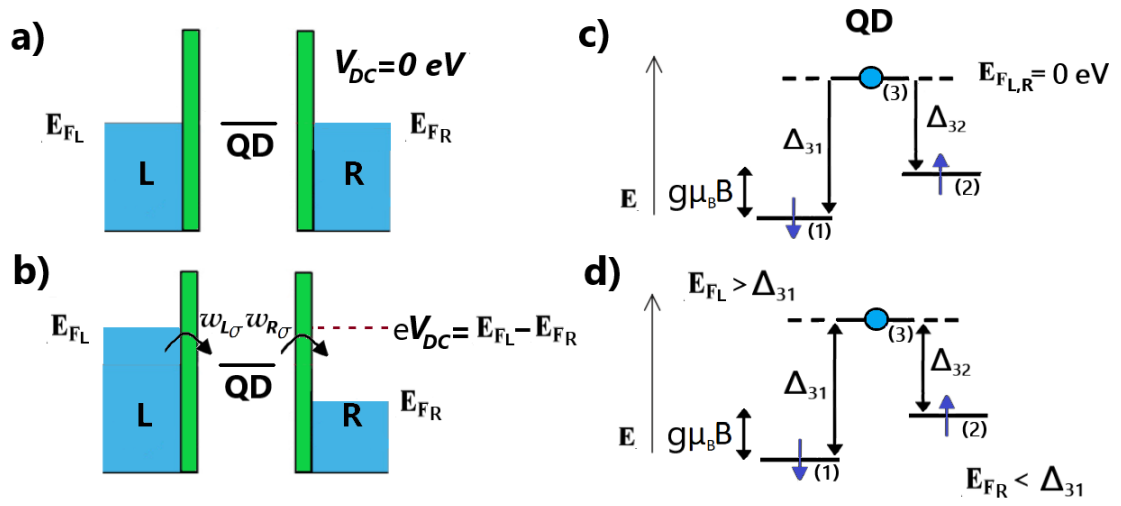

Figure 3.12: Static energy scheme of the $S_T = 1/2$ QD Hamiltonian (right) and the cotunneling configurations (left). Plots a) and b) are one-electron energy schemes representing a double-barrier QD system at zero and finite bias. Plots c) and d) show the many-body energies of the states involved in the cotunneling process at zero and finite bias respectively. At zero-bias, a) and c) pictures, no net current is passing from one reservoir to another, the Fermi energies of the electrodes are taken as the reference of electronic energy, $E_{f_{L,R}} = 0$. In the QD configurations, if the magnetic field is zero, the QD is in state $|1\rangle$ that we take as a pure down state, $\sigma = -1/2$, while state $|2\rangle$ is an up one, $\sigma = 1/2$. State $|3\rangle$ is the empty state that connects both filled states when the QD is coupled to the electrodes, because the QD needs to empty in order to change its spin. We take degenerate $\varepsilon_\sigma < 0$ such that the up and down states are energetically below the empty one if the magnetic field, B, is not strong enough. At zero temperature, the empty state is aligned with the two Fermi energy levels of the electrodes. In order to induce a current through the QD and arrive to pictures b) and d), we apply a DC bias voltage such that $eV_{DC} = E_{f_L} - E_{f_R} > 0$, by decreasing E_{f_R} while, symmetrically, increasing E_{f_L} until the absolute value of the right Fermi energy level is larger than the difference $\Delta_{31} = -\varepsilon_\downarrow - g\mu_B|\mathbf{B}|/2$. Similarly, $\Delta_{32} = -E_2 = -\varepsilon_\uparrow + g\mu_B|\mathbf{B}|/2$.

The Floquet theory presented before depends on the difference in energy $\Delta_{ij} = E_i - E_j$ for states i and j with respect to the position of the Fermi levels. In c) we keep the Fermi levels at zero in order to reproduce an equilibrium situation where the chemical potential is well defined and there is no electronic current. In d) we apply the symmetrical bias drop such that the left chemical potential is above $\Delta_{31} = -\varepsilon_\downarrow - g\mu_B|\mathbf{B}|/2$, so a down electron can enter into the QD. At the same time, the right chemical potential is below Δ_{31}, so the electron can leave the QD, by returning the QD to state $|3\rangle$. The transfer process couples states $|1\rangle$ and $|3\rangle$. State $|2\rangle$ can undergo the same process, coupling states $|2\rangle$ and $|3\rangle$. As a consequence, states $|1\rangle$ and $|2\rangle$ can couple mediated by state $|3\rangle$. This spin-flip process is thus of higher order than a single-electron one because it involves twice the empty state, state $|3\rangle$. The coherent superposition of spin-flip processes leads to the appearance of Kondo physics that unfortunately cannot be treated by our Floquet theory due to the perturbative character of the electronic self-energies. Nevertheless, this description of the cotunneling process is tantamount to the physics entailed in the Schrieffer-Wolff transformation [86] that defines an effective exchange interaction between a magnetic impurity and an itinerant electron that interacts with the impurity via the hybridization or hopping terms, w_α.

The opposite limit would correspond to the low-charging energy limit. In this case, the impurity would be able to become doubly charged, transmitting electrons without need of involving the empty state, state $|3\rangle$. As a consequence, spin-flip processes become inefficient and cannot take place. This is of great importance for ESR, because for a spin-1/2 impurity, ESR processes cannot occur if spin-flip processes are absent. This is clearly seen studying the ESR signal as a function of the mangetic field direction.

In addition to these, we have several other control parameters such as the Floquet number n, the electronic-level broadenings due to the hybridization of the QD with the electrodes, the spin polarization, P_α, of electrode α that allows us to define a new broadening function that includes the spin polarization, $\Gamma_{\alpha\sigma} = (1/2 - \sigma P_\alpha)\Gamma'_\alpha$, and the driving strengh A_α, where α is the electrode index L or R.

The Floquet number controls the convergence of our results. For $n = 5$ the trace of the

reduced-density matrix is converged to better that 0.0001%, which suffices our purposes.

The spin polarization, P_α, can take values between -1 and 1. A zero value indicates no polarization. The electronic spin will then be polarized along an axis given by the magnetization of the STM tip. Here, we will assume that this axis is always the z-axis and the external magnetic field together with the surface anisotropy will be referred to this z axis.

The driving force A_α is equal to $V^\alpha_{AC}/|\delta_{ab}|$, as we established in [46]. Based on DFT calculations, we showed that the tip-substrate electric field induced by the applied bias leads to a change in the electronic barrier that the electrons have to tunnel. This variation of the barrier follows the AC field, leading to the driving mechanism assumed in the present theory, namely the modulation of the hybridization or hopping terms, $w_{L,R}$. In [46], we followed a WKB description to estimate the change in the tunnel barrier [56]

$$\delta^{-1}_{ab} \approx \frac{m^* \left(k_F(1 - L\kappa_F) - iL\kappa_F^2\right)}{\hbar^2\kappa_F^2(k_F + i\kappa_F)}.$$

In this expression, $|\delta^{-1}_{ab}| \sim (0.3 - 2.1) \times 10^{-3}$ meV^{-1} and, since $V^\alpha_{AC} \sim (10 - 60)$ mV, [14], we have $A_\alpha \sim (3 - 126) \times 10^{-3}$. We emphasize that due to the perturbative character of our theory on the hybridization or hopping terms, the driving cannot be very large. Furthermore, our simplified expression for the current, Eq. (2.56), shows that the driving does not make sense if it is larger than 50% the static hybridization or hopping terms, w^0_α. The broadening due to these hopping terms, $\Gamma_{\alpha\sigma}$, needs to be quite small in order to apreciate the resonance peak on the driving frequency, since they are the only contribution to decoherence in our theory. Moreover, we choose it to be symmetric so $\Gamma_{L\sigma} = \Gamma_{R\sigma}$ when $P_\alpha = 0$, consistently with the symmetric bias drop. The current is always calculated on the left electrode.

Starting set of parameters

The *starting set of parameters* that we will use are:

- The magnetic field is fixed to $\mathbf{B} = (5, 0, 0.2)T$, where the tip's spin polarization fixes the z axis.

- The driving and coupling constant are symmetric and equal to 5% and $50\,\mu$eV respetively. We assume a driving term from each electrode and consider them acting on phase.
- The tip is the right electrode and it is spin polarized with $P_R = 0.35$.
- The electronic level is set to $\epsilon_\downarrow = \epsilon_\uparrow = -1$ meV, fixing the energy difference between electronic states to $\Delta_{31} = 1.29$ meV and $\Delta_{32} = 0.71$ meV.
- The temperature is fixed at one Kelvin.

Current dependence on applied DC voltage

Using the above system, we are going to fix the ESR-STM simulation parameters for the present case of spin $1/2$, and explore them routinely to understand their effect on the ESR-STM spectra. We start by studying the effect of the DC bias in the tunneling current followed by the effect of modulating the hopping term with a cosine function at a fixed frequency.

As we pointed out in Fig. 3.12, we start with both electrodes at zero energy $E_{f_\alpha} = 0$ eV. Then, we lower the right electrode Fermi energy while, symmetrically, we increase the left one. The resulting population of state $|1\rangle$, ρ_{11} is plotted as a function of the applied bias (no AC component) in Fig. 3.13 (left). At low bias, the state is completely populated because the above starting conditions makes it the ground-state of the QD. When the bias matches $2\Delta_{31}$, state $|1\rangle$ becomes resonant with empty states of the R-electrode. As a consequence, the three states of the QD become equally populated under our above starting conditions and the population stabilizes to $1/3$, together with the populations of states $|2\rangle$ and $|3\rangle$, *i.e.* the QD can be equally found with its spin down, up or positively charged (empty). A similar behavior is revealed in the coherence ρ_{12}, Fig. 3.13 (right). Only when the empty level corresponding to state $|3\rangle$ is available, states $|1\rangle$ and $|2\rangle$ become coupled. Under the polarization of the R-electrode they build a non-zero coherence. We see that the imaginary part of the coherence is larger than the real part revealing the dissipative character of the electronic transport process with the inelastic effect associated to opening the channel represented by state $|2\rangle$. Indeed, this is just the signature in the reduced-matrix density of

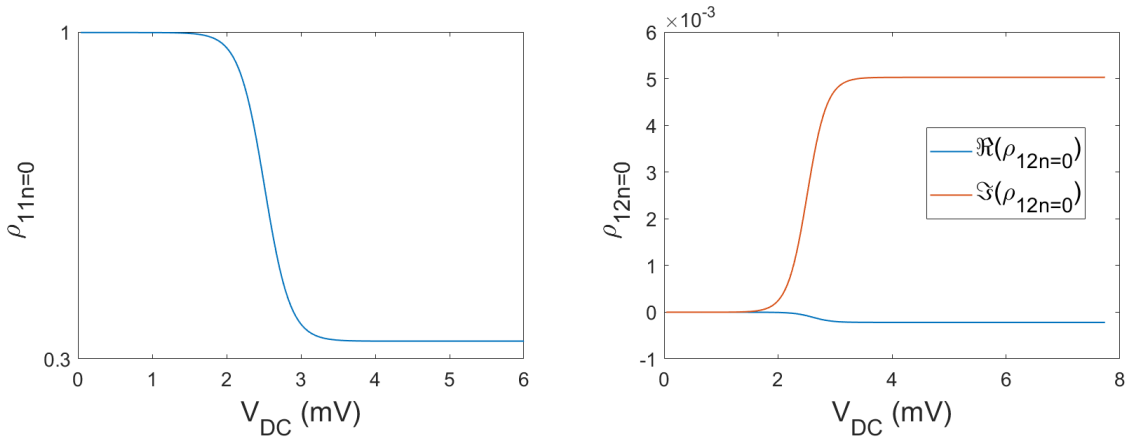

Figure 3.13: Evolution of the population of state $|1\rangle$ corresponding to the lowest level (right) and the coherence (left) between states $|1\rangle$ and $|2\rangle$ with DC voltage using the starting set of parameters in 3.3.1. Since these calculations are computed for zero frequency, the only Floquet components of the steady density matrix that survives are the ones with $n = 0$, so $\rho_{ij} = \rho_{ij;0}$. Initially all the population is concentrated into $|1\rangle$ because it is energetically favorable. As we increase the voltage, and because the coupling is symmetric, a steady state of $1/3$ weight for each state is achieved. Moreover, the coherence starts to be different from zero when a transition from state $|1\rangle$ to state $|2\rangle$ is made possible by the DC bias. The transition occurs at $eV_{DC} = 2\Delta_{31}$. There is no transition at $eV_{DC} = 2\Delta_{32}$ because the population is "trapped" in the lowest energy state.

the inelastic electron tunneling spectra (IETS) when there is a magnetic excitation in the QD. There should be a second inelastic threshold at $eV_{DC} = 2\Delta_{32}$, that is absent because of the spin polarization of the R-electrode, changing the sign of the bias drop makes it appear.

Figure 3.14 (left) shows the electronic current in the system. At low bias, the system is basically in equilibrium with a non-evolving population of state $|1\rangle$, Fig. 3.13 (left). The electronic level is well below both Fermi energies and the broadenings due to the hopping terms are very small. Only does the low-bias current become finite. The differential conductance is plotted on the right pannel, showing a peak at the threshold bias $eV_{DC} = 2\Delta_{31}$. Due to have a peak in the conductance, we can ensure that we are in sequential tunneling regime. Although the experiments are normally set in the cotunneling regime, we chose

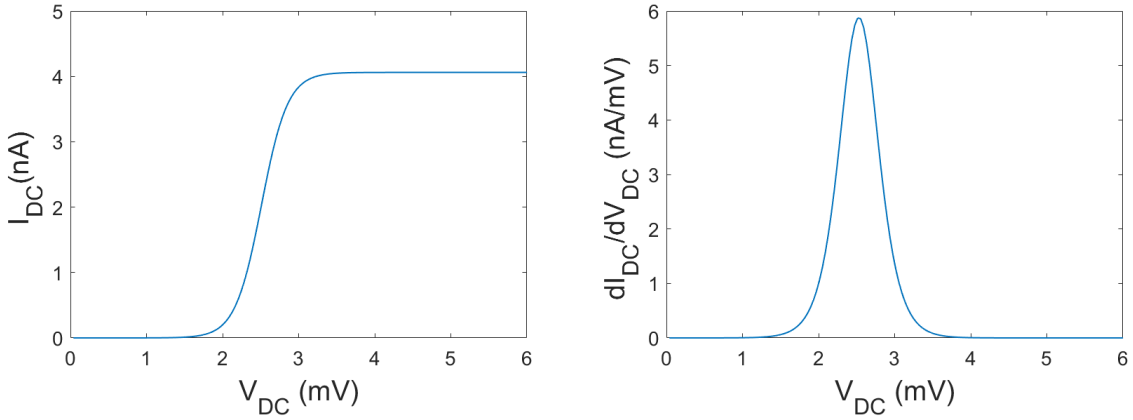

Figure 3.14: Static current (left) and conductance (right) vs voltage. After the connection between states $|1\rangle$ and $|3\rangle$ happens, a current different from zero raises reflecting the opening of an inelastic channel. It saturates at higher bias when all channels are fully open. The conductance peak matches the transition at which $eV_{DC} = 2\Delta_{31}$ showing that we are in the sequential tunneling regime. The conductance peak width is related to the temperature and to the coupling to the electrodes. At $T = 1\,K$ the $FHWM = 0.53$ meV showing that the intrinsic broadening due to the coupling to the electrodes is negligible at our chosen *starting* set up.

the sequential one since, later on, it makes simpler to understand the frequency spectra. At these low values of electronic hopping, the width is controlled by the temperature, at one Kelvin it becomes $FHWM = 0.53$ meV, as expected from the temperature smearing of the Fermi occupation factors.

Long-time averaged current dependence on driving frequency

We prove that the modulation of the tunnel barrier is driving the Rabi oscillations of the spin-1/2 in the QD. Using the *starting* 3.3.1 values that we wrote above, we obtain that this is indeed the case. Using a constant hopping term plus a small fraction (5%) of the hopping term following the AC bias, we obtain clear ESR peaks in the long-time averaged current together with a characteristic dynamical behavior of the reduced-density matrix that allows us to unambiguously conclude that Rabi oscillations are being excited.

The long-time averaged current is the Floquet $n = 0$ component of the current. This is easily proven by averaging the current over a period once the steady state is reached. It corresponds to the measured DC current. The long-time averaged current, I_{DC}, as a function of driving frequency, f, shows characteristic peaks that coincide with the Bloch description of the two-level system [29]. The current decreases at the Larmor frequency, the width of the peak is largely controlled by the decoherence time, T_2, and the peak height is proportional to the Rabi frequency.

Following the published experimental literature, we will not show the total long-time averaged current, $I_{DC}(f)$, but rather its deviation from the background current. We define it by

$$\Delta I_{DC}(f) = I_{DC}(f \to \infty) - I_{DC}(f), \tag{3.5}$$

where $I_{DC}(f \to \infty)$ is the current far from resonance satisfying two conditions: i it is much larger or smaller than the Larmor frequency but ii it is much smaller than the applied DC bias voltage in the corresponding units.

Figure 3.15 shows $\Delta I_{DC}(f)$ for the frequency f going from zero to 1500 GHz (corresponds to 6.2 meV) when the applied bias is 7.7 mV. Below 500 GHz one peak clearly dominates the spectra. Above 500 GHz several threshold mark steps in the current. These steps

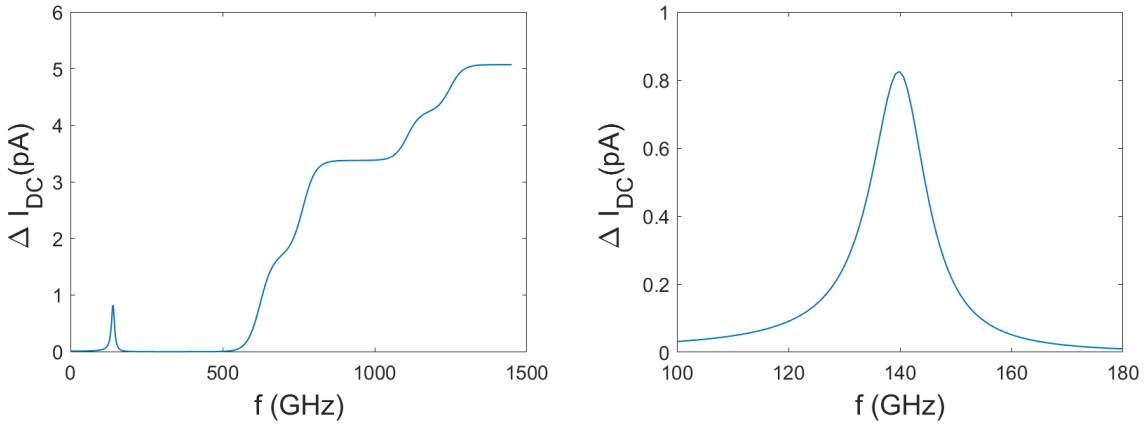

Figure 3.15: Change in the current vs frequency for a fixed DC bias voltage of 7.7 mV. $E_{f_L} = -E_{f_R} = 3.85$ meV. $\Delta I_{DC} = I_{DC}(\omega \to \infty) - I_{DC}$, $I_{DC}(\omega \to \infty)$ is the current far from resonance but evaluated at an angular frequency ω that is still much smaller than the applied bias, *e.g.* $10\hbar\omega < eV_{DC}$ so the frequency does not alter the Fermi occupations, see Eqs (2.48) and (2.51). The whole spectrum is on the left picture while a zoom of the resonance peak is plotted on the right one. The resonance peak position coincides with the energy difference between states $|1\rangle$ and $|2\rangle$ which is $g\mu_B|\mathbf{B}| \approx 5.79 \times 10^{-1}$ meV= 140 GHz. The rest of the spectrum comes from partially closing some transitions by increasing ω. Therefore, the jumps in the current coincides with $f_1 = (\Delta_{13} - E_{f_R})/h = 619$ GHz, $f_2 = (\Delta_{23} - E_{f_R})/h = 759$ GHz, $f_3 = (\Delta_{32} + E_{f_L})/h = 1103$ GHz and $f_4 = (\Delta_{31} + E_{f_L})/h = 1243$ GHz. After that the current saturates.

show a strong dependence on the temperature, while the low-frequency peak is largely independent. The origin of the steps is clearly related to inelastic thresholds that are satisfied by the driving frequency and the shape of the steps to the Fermi occupation factors as the temperature dependence shows. Indeed, the steps coincide with $f_1 = (\Delta_{13} - E_{f_R})/h = 619$ GHz, $f_2 = (\Delta_{23} - E_{f_R})/h = 759$ GHz, $f_3 = (\Delta_{32} + E_{f_L})/h = 1103$ GHz and $f_4 = (\Delta_{31} + E_{f_L})/h = 1243$ GHz. At larger frequencies all transitions are possible and the current saturates.

The right pannel of Fig. 3.15 shows the low-frequency peak. This is clearly an ESR peak due to the Rabi oscillations between states $|1\rangle$ and $|2\rangle$. The oscillation is a spin-flip transition that reflects the Zeeman lifting of the spin degeneracy in the applied magnetic

field as we mentioned above in the *starting* conditions. The Larmor frequency due to the Zeeman splitting is $g\mu_B|\mathbf{B}|/h \approx 5.79 \times 10^{-1}/h$ meV= 140 GHz in excellent agreement with the frequency that maximizes ΔI_{DC}. The resonance peak has some asymmetric lineshape which can be enhanced by making the left broadening larger. Then, a Lorentzian profiles emerges which indicates the results of the Bloch theory are oversimplications [29].

The hallmark of ESR transitions is revealed in the reduced-density matrix dynamical behavior. Figure 3.16 shows the population of the lower energy state, state $|1\rangle$, as the driving frequency is rammed up. As expected the $n = 0$ Floquet contribution (left pannel) presents a peak at the Larmor frequency showing that the Rabi oscillation involves state $|1\rangle$. At larger frequencies, the inelastic transitions made possible by the driving appear, giving rise to the clear steps in the current, Fig. 3.15. These transitions are not Rabi oscillations and are then absent from the $n = 1$ and $n = 2$ contributions. However, Fano profiles show the dynamical behavior of the Rabi oscillations in these two contributions, clearly proving that the reduction of DC current at 140 GHz is an ESR transition. Furthermore, $n = 2$ involves a second-order harmonic, giving one more Fano profile at half the Larmor frequency, 70 GHz.

Rabi oscillations involve quantum coherence between the states involved in the transition. This is better seen by studying the non-diagonal elements of the reduced-density matrix, also known as coherences. Figure 3.17 shows the real and imaginary part of the coherences between states $|1\rangle$ and $|2\rangle$, that are the ones involved in the Rabi oscillation. Clearly the Larmor frequency centers Fano profiles for all these values. As in the case of the population, the $n = 2$ Floquet component of the coherence presents two resonance frequencies due to the possibility of having the second-harmonic oscillation.

The behavior of the reduced-density matrix inequivocally proves that the peak in the long-time averaged current at 140 GHz signals a Rabi oscillation. As a consequence, we have proven that the modulation of the tunel barrier by an oscillating electric field is able to induce ESR.

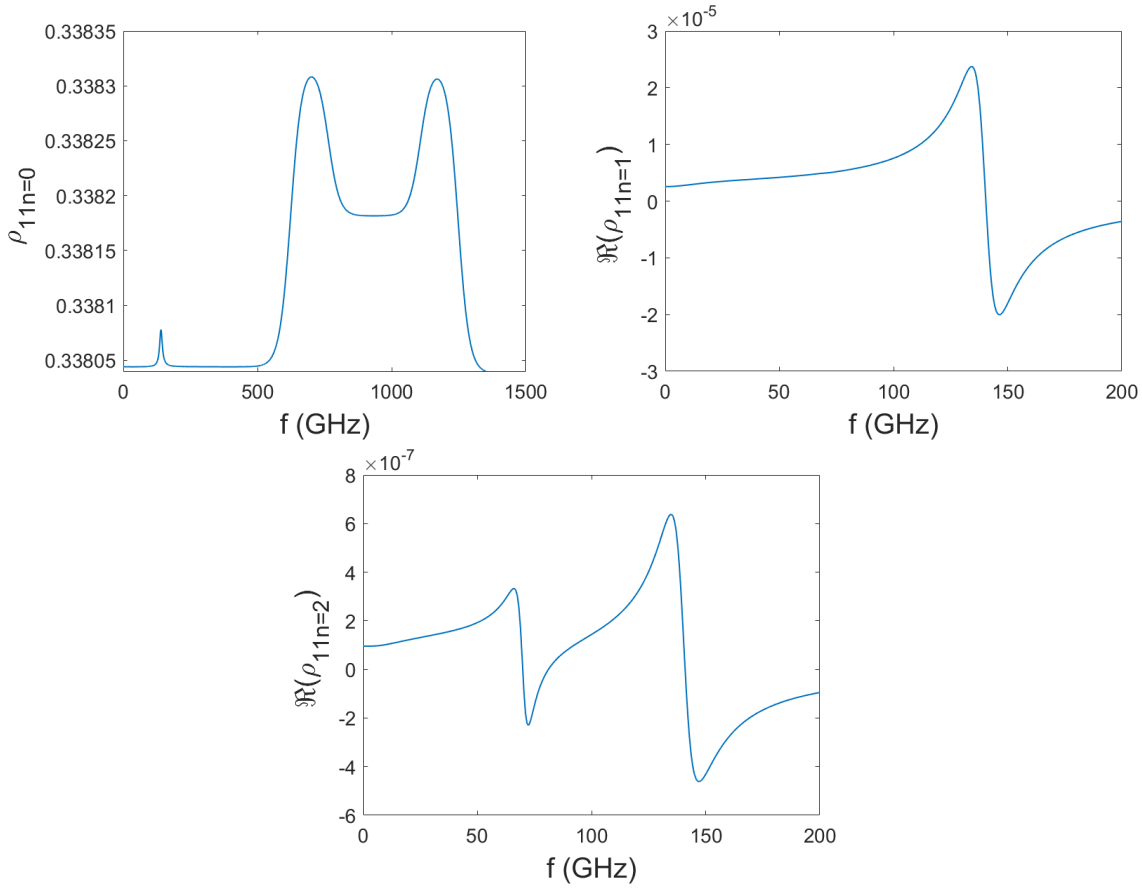

Figure 3.16: Population of the lowest state, state $|1\rangle$, for different Floquet numbers vs frequency. The applied bias is $V_{DC} = 7.7$ mV. The resonance peak is found for $n = 0$ at 140 GHz. At larger frequencies, the population changes because of the frequency dependence of the Fermi function found in the state transition rates, eqs (F.2) and F.4. These equations reflects the behavior found in the current beyond 500 GHz, Fig. 3.15. When all transitions become possible, the population changes to the initial one. The Floquet components $n = 1, 2$ of the population of state 1 slightly changes at high frequency. They, however, present Fano profiles at the Larmor frequency. While $n = 1$ only presents one resonance, $n = 2$ shows a second order transition at half the Larmor frequency, 70 GHz. This harmonic transition reflects the $n = 2$ dependence on the frequency, giving a sizeable contribution to the current at half the Larmor frequency. Increasing the driving enhances this second harmonic resonance, following eq (2.56).

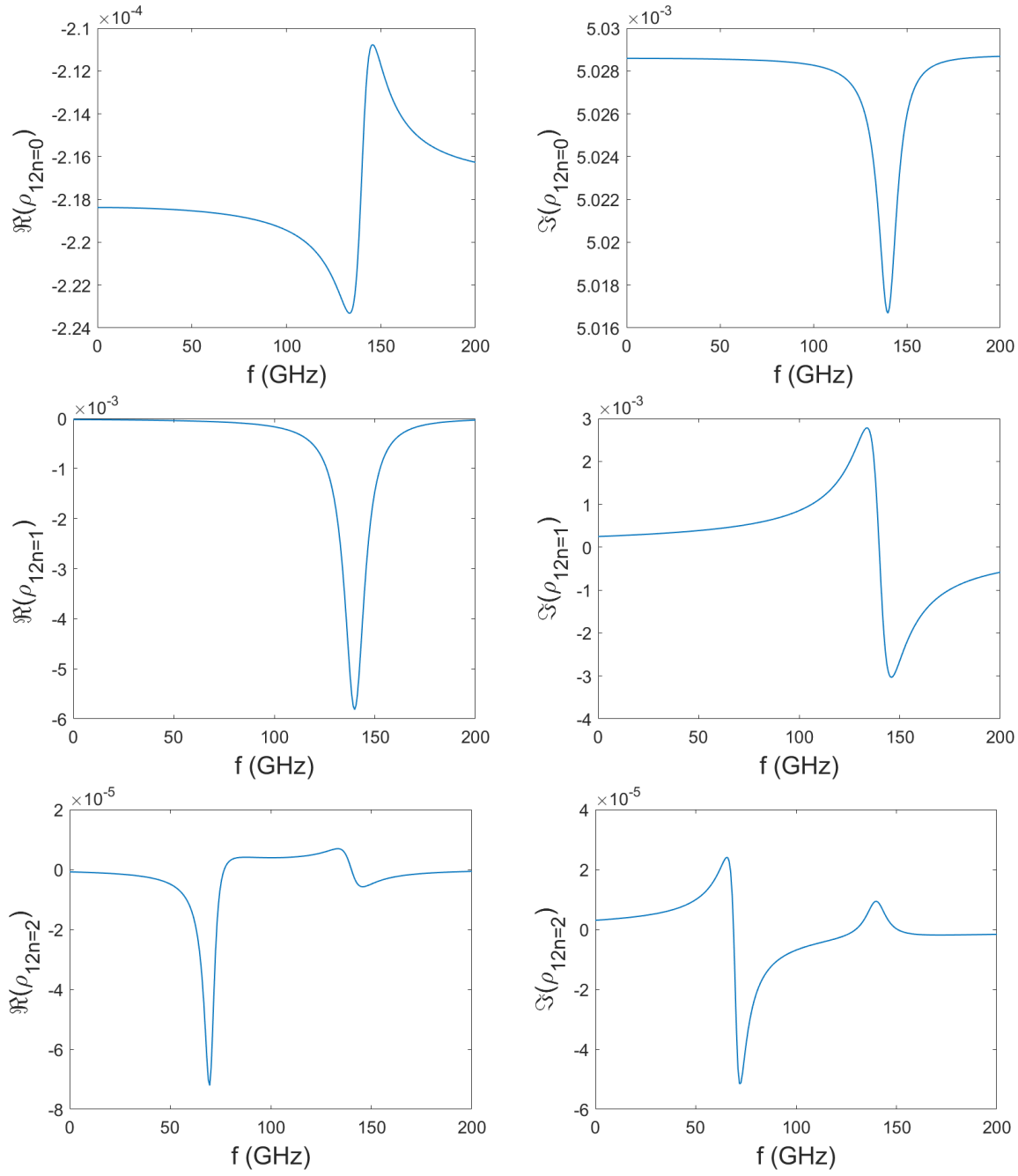

Figure 3.17: Real and imaginary parts of the coherence vs the frequency for three different Floquet numbers, $n = 0, 1$ and 2. Resonance peaks are found at the Larmor frequency for the Floquet numbers $n = 0, 1$ while, for $n = 2$, a second order transition also emerges at half the Larmor frequency.

Electrode spin polarization

After studying the general starting case, let us fix every parameter except the electrode spin polarization. We applied 4 different polarization values: $P_R = -0.35,\ 0,\ 0.35,\ 0.7,\ 1$. Negative values of the polarization do not provide any difference respect to positive ones except for a π-dephase change in the coherence which does not affect the current or population. However, if we increase S, we will see that we have more resonance peaks and the sign of the polarization can change the peak height of them. Negative polarizations mean that we are pointing it out contrary to the z component of the magnetive field applied. Or, equivalently, we are applying a negative magnetic field and a positive polarization. Fig. 3.18 shows the results. As it was expected, zero polarization leads to zero coherence since we have the Rabi frequency equal to zero, $\Gamma_{1332;1} = 0$, and, therefore, no resonance peak emerges. The only way to make the Rabi terms different from zero is by adding some spin polarization, having a maximum Rabi frequency, or maximum peak height, at full polarization of the electrode. In fact, one can notice that the resonance peak height goes as $\Delta I_{DC}^{peak} \propto P_R$, at least in the regime we are. This actually matches what it was found in [14] about the peak height. They infered that it is proportional to the square of the Rabi frequency. In our case, from eq 2.63, the Rabi frequency is

$$\hbar\Omega = -\sum_{\sigma} A_R \mu_{13\sigma} \lambda_{32\sigma} \Gamma'_R (1/2 - \sigma P_R) = A_R \mu_{13\uparrow} \lambda_{32\uparrow} \Gamma'_R P_R, \tag{3.6}$$

where we used $\mu_{13\downarrow}\lambda_{32\downarrow} = -\mu_{13\uparrow}\lambda_{32\uparrow}$. Hence, it is exactly proportional to the polarization and, since the change in the current is proportional to the square of P_R and only the Rabi frequency depends stronly on it, we can conclude that $\Delta I_{DC}(f) \propto \Omega^2$. The exact function is a bit challenging to compute since it implies calculating the Floquet density matrix elements.

Equation (3.6) makes clear how fundamental the electrode spin polarization is to the feature of ESR. First, because without polarization the ESR signal is strictly zero since we have no Rabi term. Second, because it gives an intrinsic axis of quantization of the spin that is going to determine the role of the external magnetic field and the substrate anisotropy. Indeed, the directions of these three axis have to be considered in order to understand the degree of spin mixing and existance of ESR signals in any possible system.

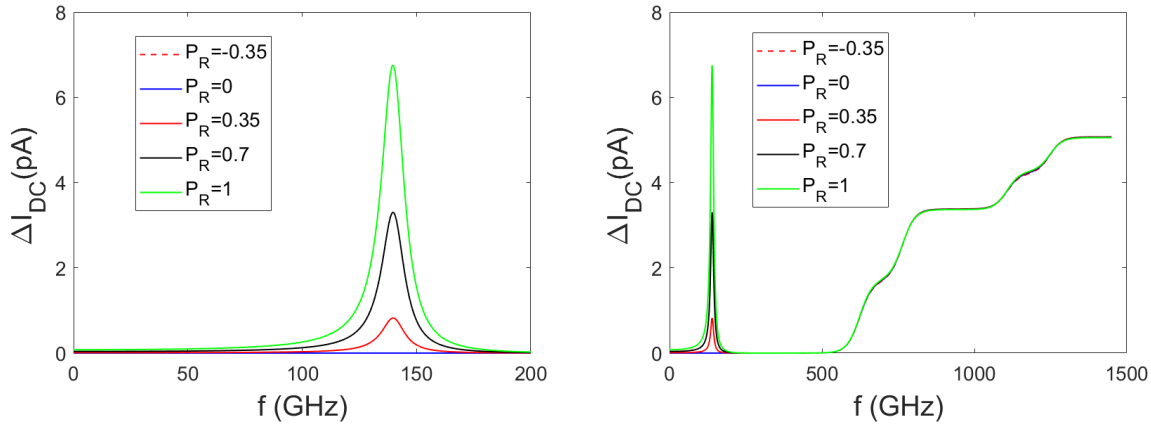

Figure 3.18: Change in current vs frequency. The whole spectra are on the left picture while a zoom of the resonance peak is plotted on the right one. The spectra at high frequency are independent on the spin polarization, but the resonance peak height grows with the polarization. Therefore, the peak height increases with the Rabi frequency. The negative value of the polarization provides the same spectra as the positive one.

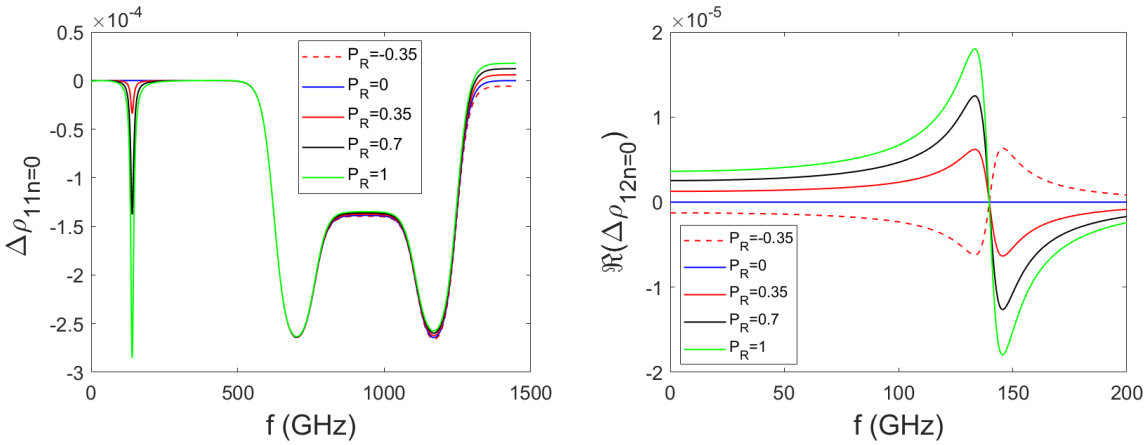

Figure 3.19: Change in the population of the lowest states and coherence. As we increase the polarization, the peak at the Larmor frequency grows, showing again its ESR character clearly in the coherence. As it was mentioned, negative polarizations only cause a π-dephase. Here, we notice that the polatization determines the value of the population change at high frequencies. This happens because we are not permiting some transitions so we cannot recover the initial change in population. Plus, the rates depends on the polarization.

Let us delve now in the implications of spin polarization to have an ESR signal. We will study the direction of an applied magnetic field in the next section. In the absence of spin polarization, the impurity's spin will not precess. This comes out from our calculation because the coherences are zero. Figure 3.19 clearly shows this. The left panel depicts the total populations, we see that only the populations at the Larmor frequency increase with spin polarization due to its Rabi character. The coherences are plotted on the right pannel, showing a characteristic Fano profile centered at the Larmor frequency when the spin polarization is different from zero. Again, the increase of the values of the coherences with polarization proves that the peak at the Larmor frequency is indeed an ESR peak.

We can qualitativily understand the need of spin polarization to have any Rabi oscillation also in a more physical meaning, not just mathematically. In the absence of spin polarization, the higher-order spin-flip transitions will become inefficient/null in front of the lower-order transition that is the direct transfer of an electron from electrode L into R through either state $|1\rangle$ or state $|2\rangle$. This happens because the upcoming electron can freely move through the states, it can choose any path from L to R electrode and the average current by spin-flip vanishes. In the presence of spin polarization, say 100% spin-down polarized R electrode, the electrons cannot equally go to this R electrode by being previously in state $|1\rangle$ or $|2\rangle$ (and then returning to $|3\rangle$). Instead, there is "preferable" path to choose. In this case, only spin-down electrons can reach the R electrode and therefore, all spin-up electron need to spin-flip to contribute to the current which makes spin-flip current dominant and the Rabi oscillation possible.

Magnetic field direction

The perpendicular magnetic field, B_x, is essential to have any sort of coherence since it allows having states $|1\rangle$ and $|2\rangle$ with mixed character which is necessary to have an ESR-active system. As we did in the polarization section, we fix all the parameter but B_x to the starting case. Fig. 3.20 shows the results for the current. At zero transverse field, no resonance peak appears. As B_x increases from zero, a resonance peak appears and increases. The height of the peak is related to the strength of the state mixing. We have shown in the polarization section 3.3.1 that for the three-level case of $S = 0$, the Rabi

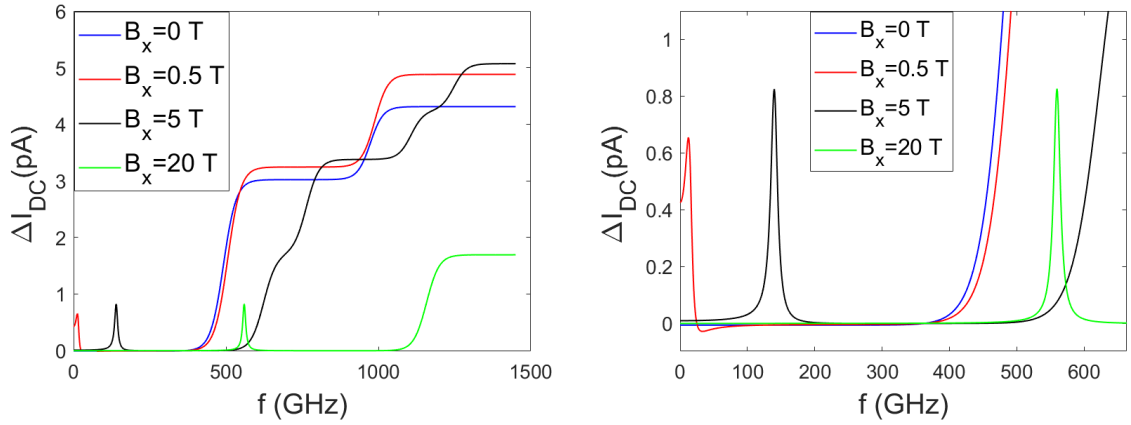

Figure 3.20: Current vs frequency for different magnetic fields. Left plot shows the whole spectrum while the right one just zooms in the resonance peaks. Increasing the transverse magnetic field leads to a bigger mixture of the states $|1\rangle$ and $|2\rangle$ which rapidly saturate (same for the resonance peaks height). The high-frequency spectrum is just displaced.

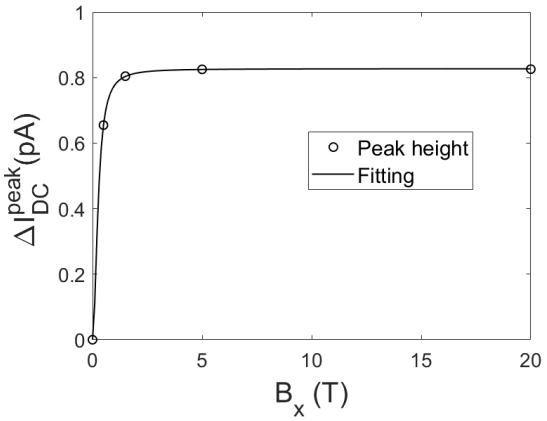

Figure 3.21: Height of the current peak vs transverse magnetic field. Two Teslas are enough to saturate the peak height. Since an analytical expression is cumbersome, we fitted the curve, following the result of the eigenvectors projection, by a rational function, given by $(aB_x^2)/(B_x^2 + b)$ where $a = 0.8269\ pA$, $b = 0.0655\ T^2$ and R-square is equal to 1. Notice that we added a transverse magnetic field of $1.5\ T$ to provide a better fitting.

frequency is proportional to $\mu_{13\sigma}\lambda_{32\sigma}$. The eigenvectors of the QD Hamiltonian are:

$$v_1 = \frac{B_x}{2B}\frac{1}{B+B_z}(-B-B_z, B_x, 0) \;\; ; \;\; v_2 = \frac{B_x}{2B}\frac{1}{B-B_z}(B-B_z, B_x, 0) \;\; ; \;\; v_3 = (0,0,1).$$

Here we are using a basis such that, when the Hamiltonian is diagonal, the empty state or state $|3\rangle$ is $(0,0,1)$ while the spin down and up states are respectively $(1,0,0)$ and $(0,1,0)$. Hence, v_3 is the eigenstate of state $|3\rangle$ that contains an empty electronic level, and v_1 and v_2 are the eigenstates for states $|1\rangle$ and $|2\rangle$. Here, we have defined $B = \sqrt{B_z^2 + B_x^2}$. These results show that if $B_x \neq 0$, v_1 and v_2 contain both spin up and spin down components, but if $B_x = 0$, v_1 and v_2 only contain spin down and up components and Rabi oscillations are not possible[1].

Using these eigenstates, we can calculate the projections entering into the Rabi frequency expression. Then, we get that $\sum_\sigma \mu_{13\sigma}\lambda_{32\sigma}\Gamma_{R,\sigma} = -B_x^2 P_R/4B^2$, which reaches a constant value as we increase B_x. This is shown in Fig. 3.21, where we see how the peak height rapidly saturates as the magnetic field B_x increases. Notice that in this case, two teslas are enough to achieve saturation.

Finally, Fig. 3.22 allows us to check that the population behaves accordingly as we decrease the energy difference between states $|1\rangle$ and $|2\rangle$. At $B_x = 0$, a population close to 0.5 for both filled states is achieved. Moreover, the population at $eV_{DC} > 2\Delta_{31}$ depends on the energy difference.

Driving

The driving term is obviously essential to have any resonance signal. Using the parameters of the starting case, see Section 3.3.1, but changing the driving, A_α, leads to Fig. 3.23, 3.24 and 3.25. Clearly, zero driving implies no resonance while increasing the driving provides a higher peak. One can notice in Fig. 3.24 that the dependence on the driving is not linear but quadratic, which is not a surprise looking at Eq. (2.56). The exact dependence on the driving is hiden in the Floquet density matrix elements which are connected to four Floquet numbers ± 2 as we mentioned in the theory. Therefore, even if Eq. (2.56) is not a quadratic function of the driving at first glance, the density matrix elements are. However,

[1]The limit $B_x \to 0$ has to be taken with care, but confirms the above explanation.

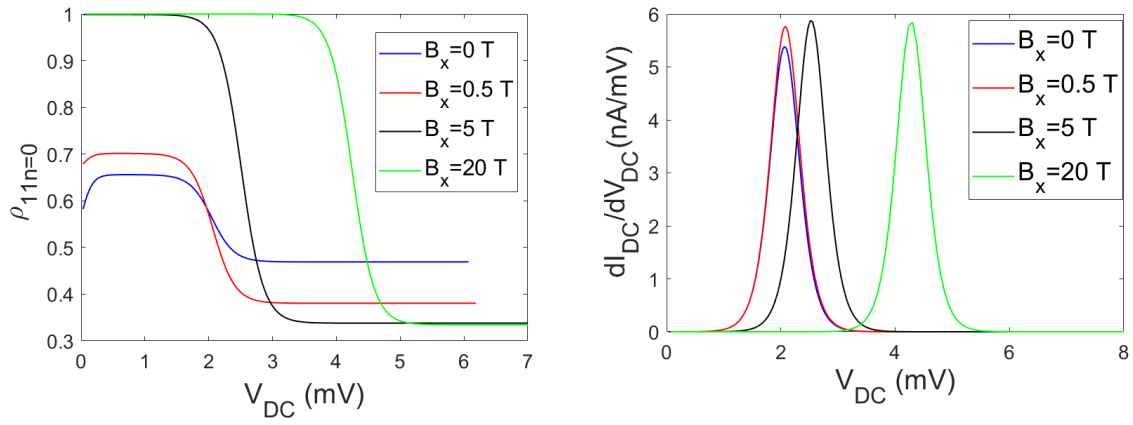

Figure 3.22: Population of the lowest levels (left) and conductance (right) vs DC voltage for different transverse magnetic field using the starting set of parameter in previously in 3.3.1. As we reduce B_x, we get closer to the degenerate case where states $|1\rangle$ and $|2\rangle$ are 50% populated. It cannot be exactly 50% because $B_z \neq 0$. A larger B_x increases the gap between states $|1\rangle$ and $|2\rangle$ leading to a displacement of the conductance peaks.

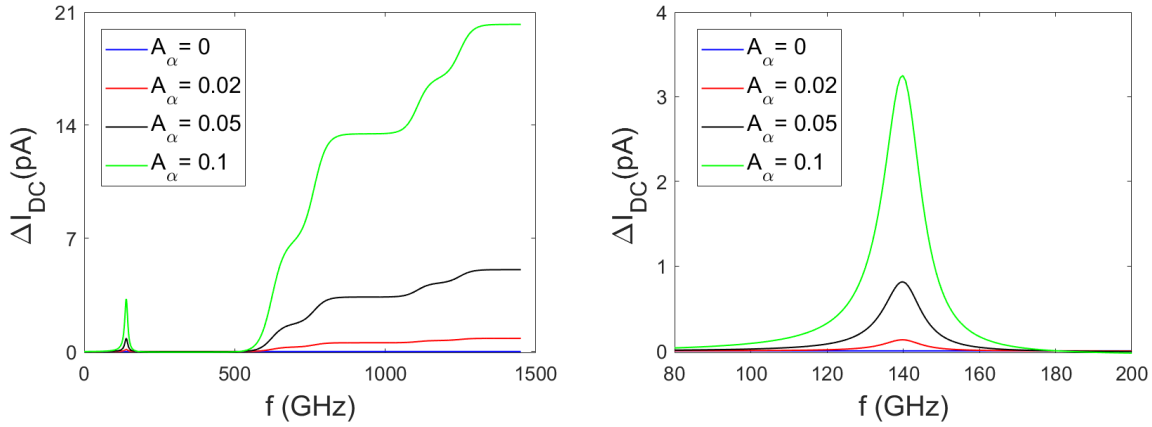

Figure 3.23: Current vs frequency for different driving parameters. Left plot shows the whole spectrum while the right one just a zoom of the resonance peak. Increasing the driving leads to higher resonance peaks while so happen to the high frequency regime.

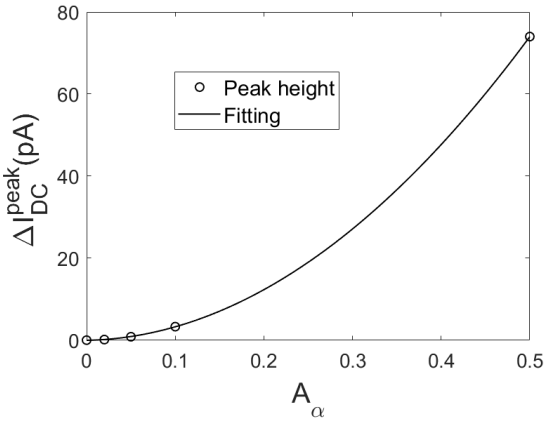

Figure 3.24: Height of the current peak vs driving. Here we added the result for $A_\alpha = 0.5$ to emphasize the quadratic dependence on the driving. The fitted curve is a quadratic function $aA_\alpha^2 + bA_\alpha + c$ with $a = 287.8\ pA$, $b = 4.162\ pA$, $c = -0.04373\ pA$ and a R-square of 1.

in order to make the quadratic part relevant we need to go to unrealistically large drivings. $A_\alpha = 0.5$ means $V_{AC} \sim 240$ mV for our present starting case, which is a very large AC coltage, above the achieved experimental values. And finally, but not less important, our theory works in a low tunneling/coupling case. If we increase A_α, we are also making the tunneling bigger, which implies leaving the regime of applicability of our theory.

Larger drivings also lead to high-harmonic signals in the ESR spectra. This is clearly seen by the coherence ρ_{12}, which is peaked in $n = 2$ Floquet components. Figure 3.25 shows the behavior of the coherences as a function of the driving frequency for various Floquet numbers, n. For the Floquet number $n = 2$ a clear peak appears at half the Larmor frequency, representative of the higher-harmonic contribution, $n = 2$. Despite the fact that this peak is visible in the coherence for $n = 2$, its contribution to the electronic current is still negligible for the present set of parameters.

We have assumed symmetric on-phase drivings for both electrodes. This means that the hopping amplitude with each electrode was modulated following the exact same equation with time. Interestingly, asymmetric drivings provide a reduction of the current at low frequencies, which increses the current change, being the π-dephased case ($A_L = -A_R$), the one in which the current decreases more, Fig. 3.26.

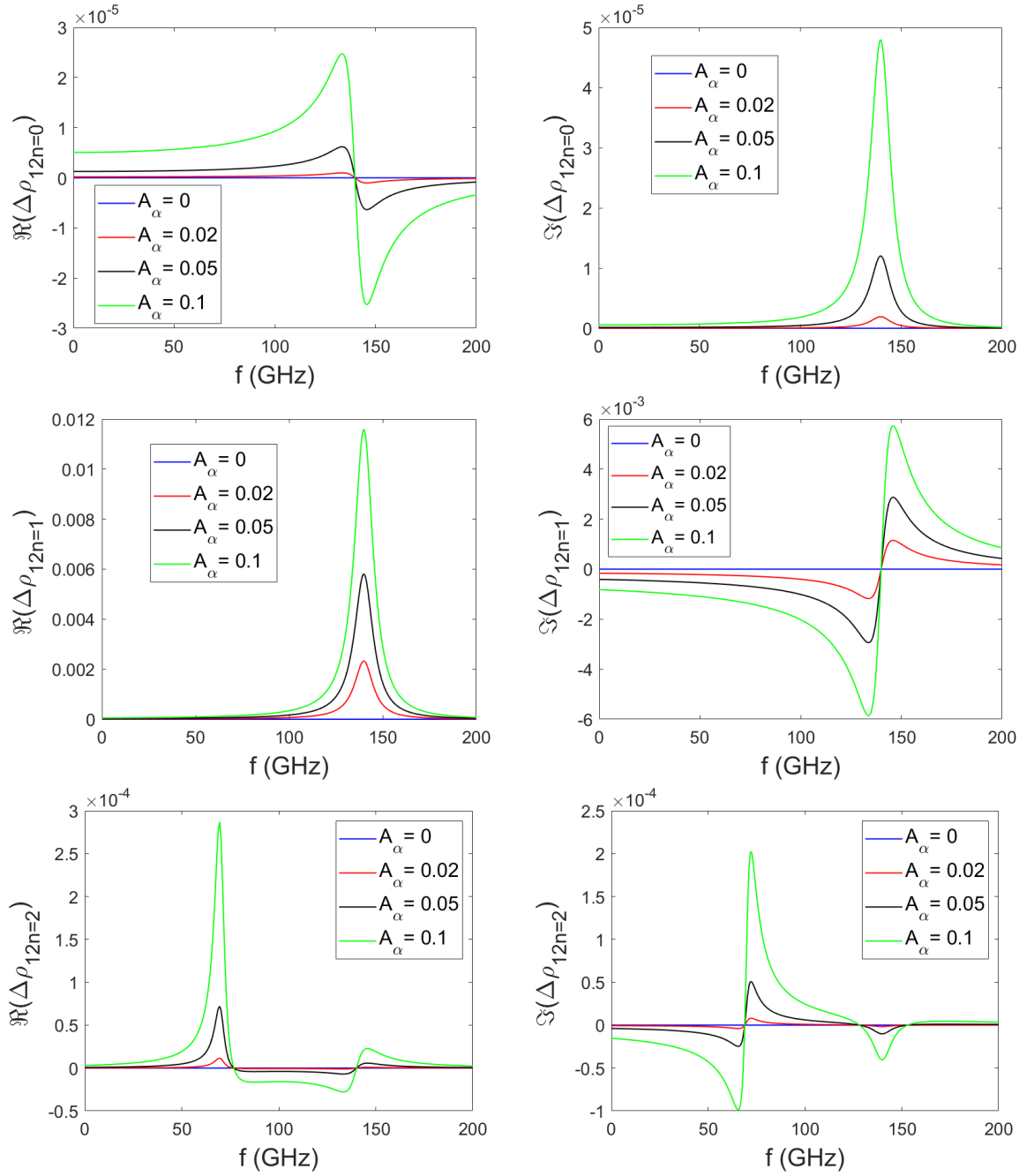

Figure 3.25: Real (left) and imaginary (right) parts of the coherence vs the frequency for four driving parameters. As we increase the driving, the coherence features at the Larmor frequency also becomes bigger. The resonance peak in the current is mainly controlled by $\mathfrak{R}(\rho_{12;1})$ but at larger drivings, $\mathfrak{R}(\rho_{12;2})$ becomes dominant.

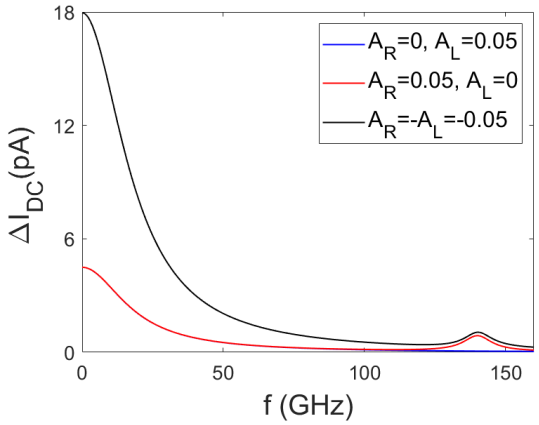

Figure 3.26: Current vs frequency for three different combinations of driving parameters, A_α. Only the low frequency regime is modified respect to Fig. 3.23. When $A_R = 0$, the resonance disappears because the R-electrode is the only one that is spin polarized.

Temperature

The main temperature effect on the ESR resonance at large DC bias voltage is to enhance the decoherence rate. However, changing the temperature from $0.1\,K$ to $10\,K$ leads to minor changes in the ΔI_{DC} line resonance profile, Fig. 3.28. Only when $100\,K$ are applied we notice a huge reduction in the ESR peak. Since the displayed three first cases correspond to $|eV_{DC}| \gg k_B T,\ \Delta_{21}$, both the non-adiabatic decoherence (also known as population scattering) and the adiabatic one (or pure dephasing) are controlled by the bias voltage, and not by the thermal broadening [29]. In addition, the chosen parameters leads to $T_1 T_2 \Omega^2 \ll 1$, in which case the Full Width at Half Maximum (FWHM) of the resonant peak is $\propto 1/T_2$ [7].

Another source of differences with temperature that we have not considered here is the variation of the tip-polarization with the temperature [15, 93]. This could be easily implemented to compare with the experimental results at various temperatures, but we do not include this effect that clearly goes beyond the scope of the present work.

What the temperature clearly modifies is the applied DC voltage profiles. Increasing the temperature lead to larger FWHM since the broadening of the Γ'_α gets bigger, Fig. 3.27. The temperature also smoothens the high frequency curves for the same reason, Fig. 3.28.

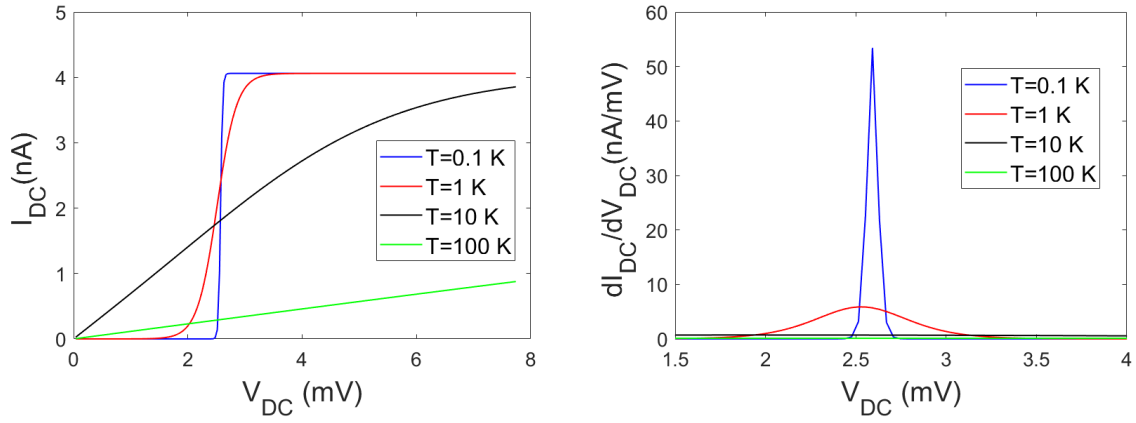

Figure 3.27: Current and conductance vs DC voltage for different temperatures. One notice that increasing the temperature leads to bigger FWHM. From $T = 0.1\ K$ to $T = 1\ K$ the FWHM changes from 0.07 meV to 0.53 meV. At 100 K, the temperature domians so the current do not vary a lot with the voltage compare to other cases.

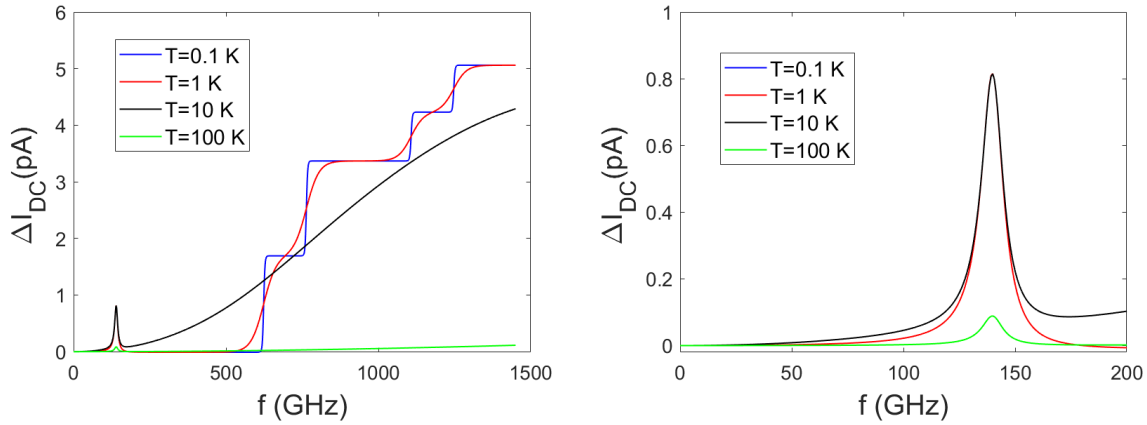

Figure 3.28: Current vs frequency for three temperatures. Left plot shows the whole spectrum while the right one just a zoom of the resonance peaks. Increasing the temperature smoothens the curves but it does not affect the peak at the Larmor frequency unless we go to really high temperatures. At 100 K, the coherence is no longer control only by the voltage. Hence, the temperature affects the coherence, reducing the width and height of the resonance peak. So, it changes the Rabi term and the coherence time.

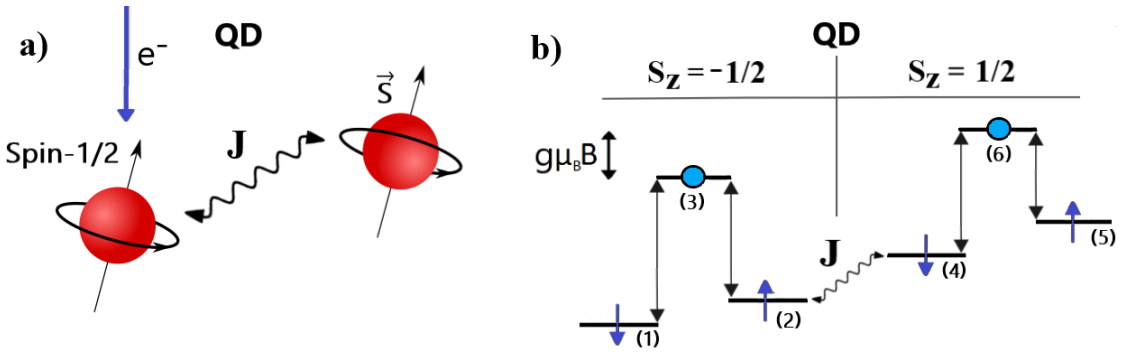

Figure 3.29: Scheme for the $S = 1/2$ case coupling with the incoming electron from the electrodes. a) shows both systems coupling through J. Three triplet states would be form plus a singlet following the formal theory of Angular-Momentum addition, [89]. b) shows a simplification of the energy level scheme similar to Fig. 3.12. The scheme is made again for negative ε_σ, zero frequency and anisotropic and coupling parameters, D and J, similar and negative. The magnetic field is parallel to the z direction. Due to J, both S_z subspaces are able to interact and a perpendicular magnetic field can mix the filled states and both empty ones.

3.3.2 Two coupled spin-1/2

Scheme and outline of the simulations

Following the interesting experimental data of Refs. [15, 93], we use our method to study the ESR-STM signals. To do this, we considered an external $S = 1/2$ that is coupled via an exchange interaction with the electronic level that transfers electrons between the two biased electrodes. The electronic level thus acts as a spin-1/2 system (see previous section) coupled to another spin-1/2. It is simple to devise a minimum basis set that describes this new QD of two spins. The basis set is given by the tensorial product of the three states of the electronic level (down, up, empty) times the two states of the coupled spin-1/2 (down and up).

Figure 3.12 shows a scheme of two spin-1/2 system with exchange coupling J. As we just explained, this coupling duplicates the Hibert space of the QD Hamiltonian, having now 6 states. The exchange coupling, J, determines whether the spins are in a coupled case or not. In the coupled case, assuming a ferromagnetic coupling (J <0) and $|J|$ larger

that any other energy parameter, except for the value of the electronic level, ε_σ, the full system becomes a $S_T = 1$ spin system. The triplet states are energetically below the singlet state, explaining why we are in an effective spin one situation. Contrary, if the coupling is anti-ferromagnetic ($J > 0$), the singlet state is the one with the lowest energy. When J is close to zero, we have a decoupled $S_T = 1/2$ spin and the corresponding results can be found in the previous section.

When J and the transverse magnetic field are non zero, we mix the filled and empty states, making possible the appearance of ESR resonances between states with $\Delta S_z = S_{z_i} - S_{z_j} \approx \pm 1$ (spin flip), where i and j can be any state from 1 to 6 in Fig. 3.29.

The anisotropy term of the Hamiltonian given by $DS^2_{T,z}$, takes into account both spins of the system: the incoming from the electrode and S. Which implies having a spin-1 anisotropy. Interestingly, when replacing $S^2_{T,z}$ by $(S_z + s_z)^2$, we find that the term $D(S_z^2 + s_z^2)$ does nothing, but $2DS_z s_z$ is like an Ising term that adds to the z component of exchange interaction. Therefore, the anisotropy creates an effective J_z which breaks the degeneracy of the triplet states $S_z = \pm 1$.

The current is computed on the left electrode in a situation of large bias DC voltage where all the states are properly connected, as we did for the $S = 0$ case (see previous section). Therefore, the right Fermi energy level is below zero while the left one above it so $E_{f_L} = -E_{f_R}$ in our presently symmetric bias drop. The other control parameters are:

i) number of Floquet functions $n = 5$.

ii) driving strength $A_\alpha = 5\%$.

iii) polarization $P_R = 0.35$.

iv) temperature of one kelvin.

The coupling constant Γ'_α is specified on each case. The behavior of this system with respect to these parameters is very similar as the one analyzed in the previous section. Thus, we will focus on how the frequency spectra change with the spin interaction, anisotropy and applied magnetic field.

Two spin-1/2: effective spin 1

When two spin-1/2 atoms are magnetically coupled, the eigenstates are given by the singlet and triplet states. If the spin interaction J is ferromagnetic and satisfies that $\mu_B|\mathbf{B}| \ll |J|$, $|D| \ll |J|$, we are making the triplet states the lowest energy states, sending the singlet state high up in energy. This provides an effective spin one in the QD Hamiltonian with the exception of the empty states that are $S_z = \pm 1/2$. Similarly, if J is large and positive, the singlet becomes the ground state but the difference in energy between the triplet states do not change. This makes the frequency spectra identical for positive and negative J.

Figure 3.30 a) shows the results for large and negative exchange interaction in the system. Here "large" means bigger than any other energy scale of the problem. We display three different spectra depending on the values of the couplings to the left and right electrodes, Γ'_L and Γ'_R. The values of the electronic current have been scaled and shifted to make them visible in the same plot. Figure 3.30 c) and d) correspond to the symmetric case, $\Gamma'_L = \Gamma'_R$. We notice three resonance peaks in the large range of frequencies, Fig. 3.30 c). Each peak corresponds with a spin-flip transitions. The first one is the spin flip between the states corresponding to the empty electronic level. This is then a Rabi oscillation between $S_z = -1/2$ and $S_z = 1/2$. It coincides with the frequency of the Zeeman splitting due to the applied magnetic field, $f_{36} = 25.35$ GHz (where 3 and 6 are the two empty states in our tensorial-product basis set, see Fig. 3.29b)). The next two peaks match the transition between $S_z = 0$ and $S_z = 1$ at $f_{2,5} = 216.66$ GHz, and $S_z = 0$ and $S_z = -1$ at $f_{1,2} = 267.04$ GHz.

It can be noticed that the symmetric case gives stronger ESR signals. The change in the current over the ESR transitions becomes drastically reduced if $\Gamma'_L < \Gamma'_R$, Fig. 3.30 b), because the electron needs to populate the electronic level in order to induce transitions and the coupling to filled electrode states has been reduced the right reservoir is always below the Fermi energy in our simulation while the left one is above it). In these calculations, the line-widths are much thinner than the symmetric case because one coupling has been largely reduced. The available transitions are the same as for the symmetric case. If

instead we have $\Gamma'_L > \Gamma'_R$, we are decoupling the empty states. As a consequence, the ESR transition involving empty states disappear from Fig. 3.30 e) and f).

The lineshape of the ESR signals in Fig. 3.30 also changes depending on the coupling of the QD with the electrodes. The symmetrical case leads to an ESR signal that is closely resembling a Lorentzian function, Fig. 3.30 d). However, the cases with asymmetric coupling leads to Fano-like lineshapes , see Fig. 3.30 f). Surprisingly, we find that Fano-like lineshapes are not common for the spin-1/2 case, while they are easily found for the present asymmetric $S_T = 1$ system.

Two spin-1/2: small coupling J

When the exchange interaction is similar in strength to the other energy parameters of the problem, the singlet state will give us a new transition in the frequency spectra. This can be noticed in Fig. 3.31 for the a) and c) plots where we find four resonance peaks. However, let us focus on the case without longitudinal magnetic anisotropy, $D = 0$, Fig. 3.31 b), that only presents three transitions.

The first transition at $f = 24.5$ GHz in Fig. 3.31 b) takes place between the singlet and the triplet with $S_z = -1$. The next peak coincides with $g\mu_B|\mathbf{B}|$ and involves the triplet states with $S_z = 0$ and $S_z = \pm 1$. These are two ESR transitions at the same frequency, yielding a strong peak in the ESR signal. The higher frequency peak corresponds to the resonance between the singlet and the triplet $S_z = -1$ state. Hence, the distance between the middle and lower/higher peaks is exactly J/h, because J equals the singlet-triplet excitation energy. The first and third transitions are the ones we sent high up in energy when the exchange interaction dominates.

In the presence of magnetic anisotropy, the degeneracy of the triplet states is lifted. This leads to the four peaks of Fig. 3.31 a), for $D < 0$ and c), for $D > 0$. The resonance peaks related to the triplet $S_z = -1$ move up in frequency by D/h while the ones where the $S_z = 1$ takes part go down by D/h. In other words, for $D < 0$, the triplet energy is reduced, leading to a smaller resonance energy pushing the different transitions closer, Fig. 3.31 a), while for $D < 0$, the triplet energy increases which translate into a larger

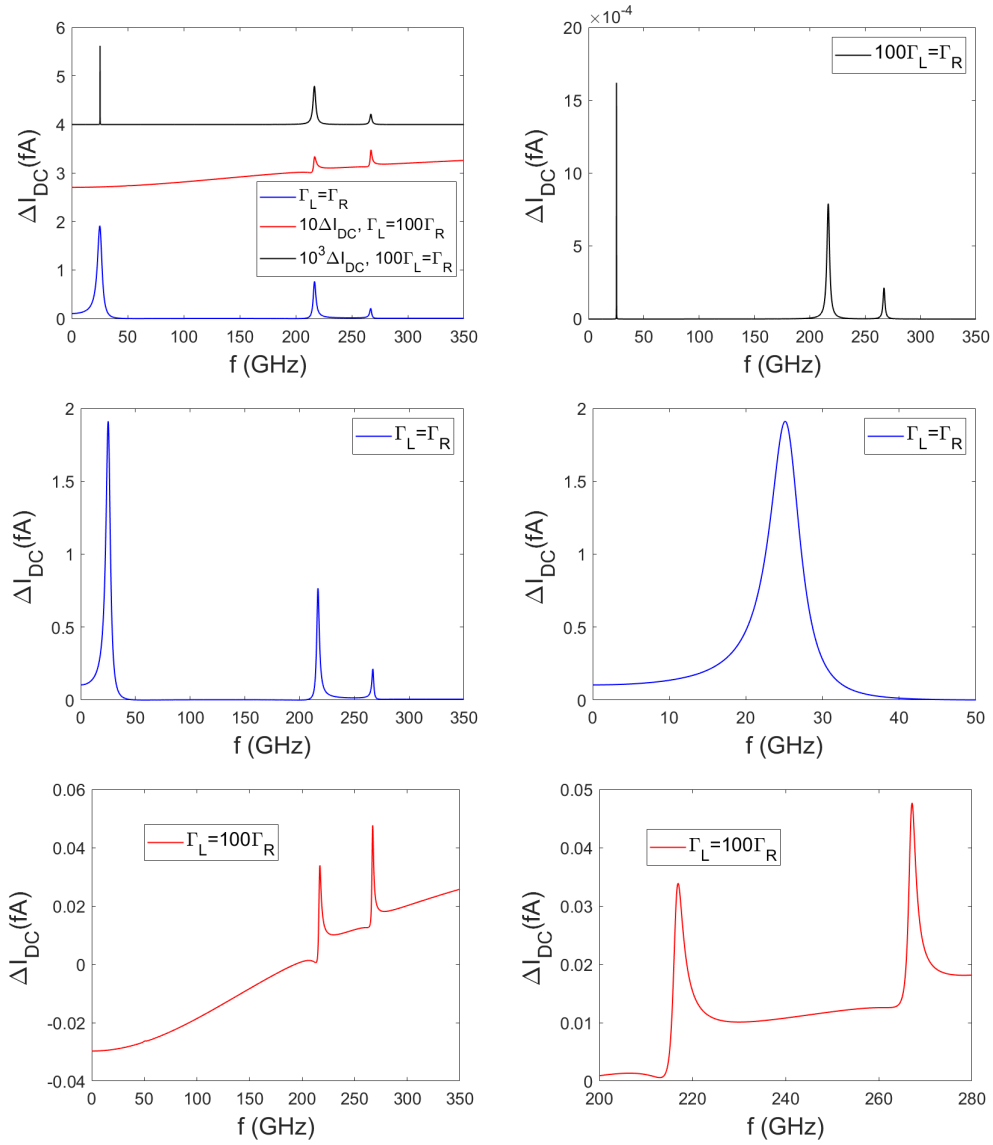

Figure 3.30: Frequency spectra for different couplings with the left electrode, for $J = -0.1$ eV. The parameters used in this case are: $\varepsilon_\sigma = -1$ meV, $\mathbf{B} = (0.1, 0, 0.9)$ T, $D = -1$ meV, $\Gamma'_R = 10$ μeV. a) contains the three cases. b) is a close up of the case $\Gamma'_L \ll \Gamma'_R$. The bias is such that the QD is resonant with empty states and filled states. Reducing the coupling of the left electrodes leads to a reduction of the occupation of the QD electronic level, with a drastic reduction of the current and ΔI_{DC}. c) and d) correspond to the symmetric case, $\Gamma'_L = \Gamma'_R$. Notice the almost-symmetric lineshape of the low-frequency transition. e) and f) refer to the $\Gamma'_L \gg \Gamma'_R$, leading to an increase of the electronic population. For this reason, the low-frequency transition, corresponding to a spin-1/2 (empty level) spin-flip transition, disappears. Resonance frequencies are: $f_{36} = 25.35$ GHz, $f_{25} = 216.66$ GHz, $f_{12} = 267.04$ GHz.

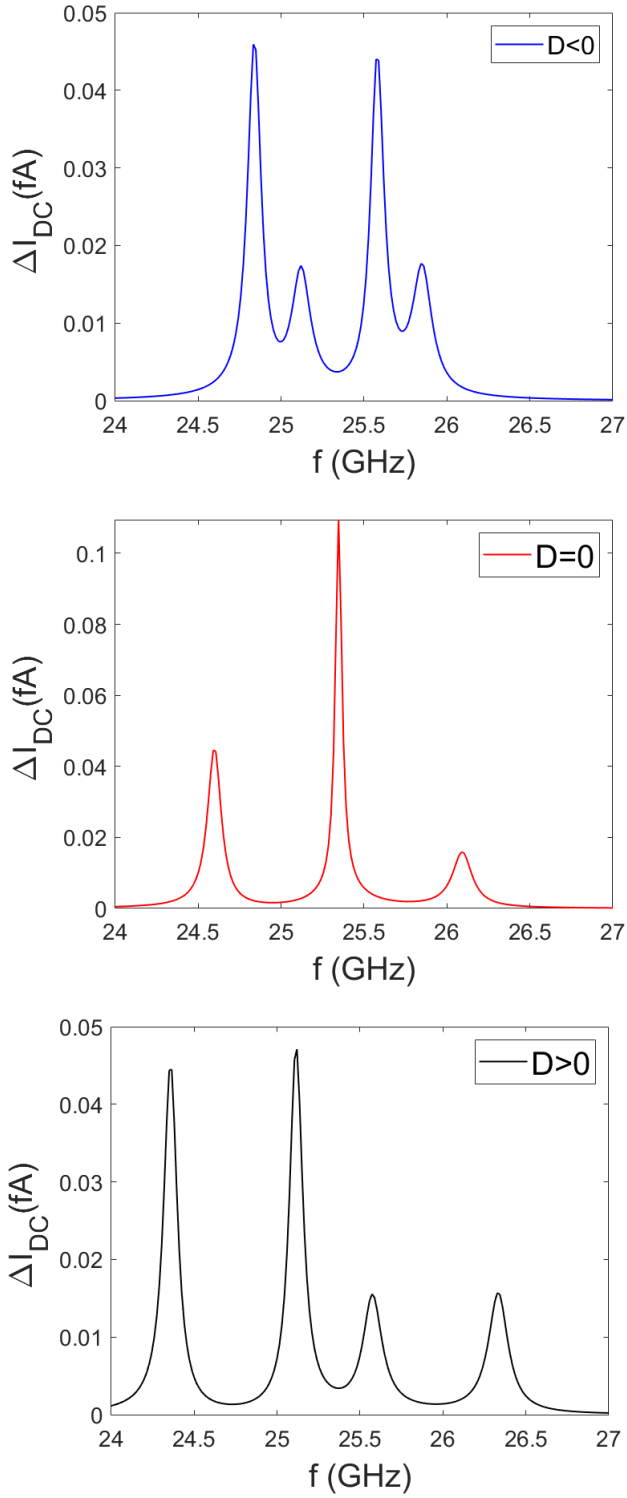

Figure 3.31: Frequency spectra for different anisotropic parameters. We used $\varepsilon_\sigma = -1$ meV, $\mathbf{B} = (0.1, 0, 0.9)$ T, $J = 3.1$ μeV= 0.75 GHz, $\Gamma'_R = \Gamma'_L = 0.5$ μeV. a) $D = -1$ μeV. b) $D = 0$ eV and c) $D = 1$ μeV. $|D| = 0.24$ GHz.

resonance energy and to more separated peaks in Fig. 3.31 c).

Two spin-1/2: applied magnetic fields

Inspired by the experiments on two Ti atoms on MgO/Ag (100), Ref. [93], we have computed the ESR spectra and compared them with the experimental ones. To do this, we needed two spin-1/2 that feel different magnetic fields. We just need to add a new Zeeman term to the QD Hamiltonian that only affects one spin-1/2 atom. The origin of this field is the magnetic interaction exerted by the tip on the atom where the current is measured. This new field is called $\mathbf{B_{tip}}$ following the notation of [93].

Figure 3.32 shows the results. The anisotropy parameter is now zero but, due to the presence of two different magnetic fields, we find four resonance peaks. The order of the resonance peaks is now, from lower to higher frequencies: transition singlet to the triplet state $S_z = 1$, transitions between the triplet states $S_z = 0$ and $S_z = -1$, next the triplet states $S_z = 0$ and $S_z = 1$ and finally singlet-triplet state $S_z = -1$ transition. The match with the experiment is satisfactory although the simulation could be better if anisotropy for the triplet states is introduced. In fact, we believe that one magnetic field is enough to fit the experiment as long as the D and J are both non zero.

3.3.3 Conclusions of the section

In this section, we have analyzed the effect of a radiofrequency bias voltage following the modulation of the tunneling barrier explained in the theory, but applying a Floquet-Green's function formalism instead of cotunneling one.

Firstly, we have focused on the simple case $S = 0$, $S_T = 1/2$, since it is the easiest one to understand and simple analytical calculations can be performed. Then we have chosen a specific set of parameters to work with and explore the effect of the DC bias and the frequency in the DC tunneling current and density matrix elements. Although all the experimental works [7, 11, 12, 13, 14, 15, 16, 17] have been realized in the cotunneling regime, in order to check out that the model is providing with appropriate results, we have placed ourself in the sequential tunneling regime. Additionally, both electrodes have

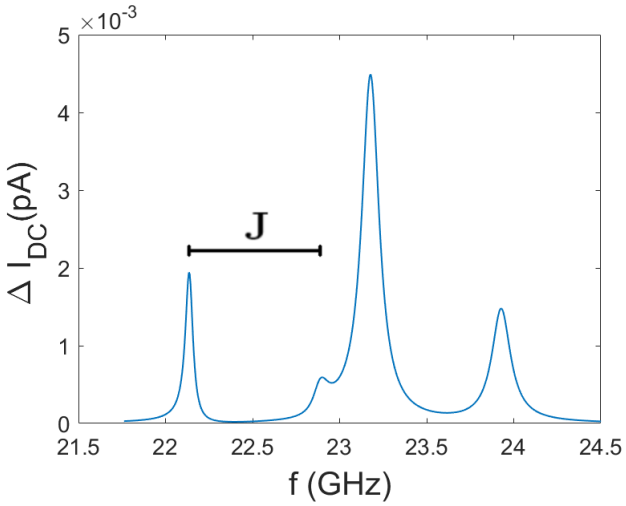

Figure 3.32: Frequency spectrum when the additional $\mathbf{B_{tip}}$ is applied. We used $\varepsilon_\sigma = -1$ meV, $\mathbf{B} = (0, 0, 0.89)$ T, $\mathbf{B_{tip}} = (0.035, 0, 0.05)$ T , $J = 3.1$ μeV$= 0.75$ GHz, $\Gamma'_R = 0.5$ μeV, $\Gamma'_L = 5$ eV, $D = 0$ eV, $A_\alpha = 50\%$, $P_R = 0.45$. In addition, we took into account the difference in magnetic moment as in the experiment of Ref. [93].

symmetrical Fermi energies. In this situation, a saturation of the DC current happens as we increase the DC bias voltage while and a peak in the conductance appears at $2\Delta_{31}/e$. This is what one would expect in the sequential regime.

Frequency spectra is computed for a fixed voltage when the DC current have been saturated. For the set of parameters used, we have found a peak at low frequencies which coincides with the Larmor frequency. By looking at the coherence between the two filled states, we could ensure that we are dealing with a ESR resonance peak. Therefore, we have induced a Rabi frequency term to the system. At higher frequencies, ω is larger enough to close Floquet channels and, therefore, it enhance the change in the current. However, none of those transitions are related to Rabi terms since the coherence do not change at high frequencies.

In order to fully comprehend these results, we started modifying one of the parameter previously used but keeping everything else constant and equal to the initial set of parameters applied. We first saw what happens for different electron spin polarization. It was shown that the change in the DC current at the Larmor frequency is proportional

to the square of the polarization of the right electrode. Since the model provide a Rabi flop rate proportional to the polarization, we concluded that $\Delta I_{DC}^{peak} \propto P_{\alpha}^{2}$. Therefore, polarization becomes essential to feature the ESR spectra: in the absence of polarization the Rabi term is zero and the impurity spin will not precess. It also provides an intrinsic axis of quantization.

Secondly, we have studied the transverse magnetic field B_x. This parameter is key to mix the character of the filled stated. Therefore, a zero perpendicular magnetic field leads to a no resonance peak. Gradually increasing the magnetic field moves linearly the ESR peak position. However, the peak height saturates rapidly. The reason behind this comes from the eigenstates of the QD Hamiltonian and how they rapidly reaches a constant value as the magnetic field is increased. We also showed that the lower the transverse magnetic is, the closer we go to a 50/50 population at zero DC bias voltage, i.e., $\rho_{11;0} \approx \rho_{22;0} \approx 0.5$ and $\rho_{33;0} \approx 0$. This happens because we are approaching the degeneracy case between states $|1\rangle$ and $|2\rangle$.

The next parameter we modified was the driving. To no one's surprise, zero driving gave us no peak at the Larmor frequency and, as we increased the driving, a square dependence of the peak height appears. In addition to this, we have shown that a large driving can lead to a second harmonic transition at half the Larmor frequency which is related with the Floquet number $n = 2$. Moreover, we have found that asymmetric drivings enhanced the change in the current at low frequency.

Finally, we have changed the temperature. One would expect a large increase in the coherence going to higher temperatures but, since we are in the sequential tunneling regime where the voltage is strong enough to open all the channels in the QD, the coherence is mostly control by electrons coming from its electrodes. Therefore, the ESR peak do not change significantly with the temperatures in this regime. Likely, in a cotunneling regime this will not be the case.

Having been studied the $S = 0$ system, we have gone a step beyond by computing the results of two spins 1/2 coupled. Again, we have placed ourself in a sequential tunneling regime to analyze the spectras easily. Exchange coupling J and anisotropy

parameter D become now relevant to the model Hamiltonian. We have found that a large exchange coupling lead to $S_T = 1$, where only three spin-flip transitions are possible if the broadening is symmetric. Two transitions are related to filled states, which are triplet states, while a third one happens between the empty states. It was shown that this last transition can disappear if the unpolarized electrode has a broadening larger than the polarized one. As a consequence, the two remaining resonance peaks have a closer fano shape than in the symmetric broadening. However, the change in the current have decreased.

Anisotropy D for a two spin $1/2$ coupled works as a Ising term in the Hamiltonian that adds a z component to the exchange coupling. If J and D are similarly small, we find four ESR transitions. Now, each of them is related to filled states since we have three triplet states and one singlet. Additionally, the transition between empty states is gone. If $D = 0$, a degeneracy between the two transitions related to the triplet state $S_z = 0$ happen, and one large resonance peak emerges in the middle at the frequency of the magnetic field applied. Moreover, it was shown that the distance in frequency between the central ESR peak and the other two remaining is exactly the exchange interaction J. Depending on the sign of the anisotropy, the peaks can move up or down in the spectra.

Finally, in the last simulation plotted in the results section, we have implemented two different magnetic field. One acting on the large spin S and the other one on the itinerant spin s. The aim behind this simulation was to compare with the experimental result in [93]. We did not expect a exact match from the beginning since we are not in the cotunneling regime. But at least we wanted to check if the essential information can be captured. The anisotropy parameter was setted to be zero but, due to the presence of two different magnetic fields, we found four resonance peaks. Although the peak position matches with the experiment, the Rabi frequencies of each transition are off the experimental ones by a factor $\sim \sqrt{30}$, which is translated into the current spectra has a factor of ~30. We think that this difference can be solved by, for example, going to the cotunneling regime. In any case, our simple model have demonstrated to be quite powerful and versatile and we are looking forward to exploring it even more in next works.

Chapter 4

Conclusions and outlook

Conclusions of the thesis

Since we already wrote conclusions at the end of each result section, here we will briefly summarize the main findings.

We have analyzed the ESR-STM problem in deep, trying to come out with a theoretical model that can simulate and predict experiments. We can outline the main task and findings of this work as follows:

- We have modeled the electronic properties of the ESR-STM experimental setups identifying the main ingredients. In doing so, we have simulated the electronic properties using density functional (DFT) calculations. This allows us to identify the coupling regime and the main effect of the applied electric field: a modulation of the tunnel barrier.
- The ESR-STM setup was simulated as a driven open quantum system. We did this on two counts:
  - A perturbative approach. First, the time-independent case was studied within a cotunneling description where the central region is modeled by a multiorbital Anderson model, and the tunneling with the electrodes is treated perturbatively. Then, the Bloch-Redfield theory was applied to study the dynamics of

the driven system under the assumption of weak driving, leading to Bloch-like equations. The Rabi frequency found was in qualitative agreement with the experiments, although it was a factor 10-20 larger than the the experimental one.

– Using Floquet non-equilibrium Green's function approach. This technique provides a more complete description of the all electrical ESR, being able to explore different regimes, from the cotunneling to the sequential transport regimes. In addition, it is not limited to weak driving. The results are quite remarkable even though the model is still largely unexplored and could be extended to more complex situations.

Outlook

The Floquet approach to the ESR problem is quite unexplored. For example, we did not explore the cotunneling regime where all the available ESR experiment were preformed. Moreover, the tunneling barrier mechanism can be extended to pulses instead of only using a harmonic driving. In addition, we could add a finite charging energy to the QD Hamiltonian to describe the double occupancy of the dot. A spin chain could also be described by our model as long as we provide the spin Hamiltonian and the corresponding basis. In conclusion, a lot of work waiting to be done.

Appendix A

Multiplet calculation: basic concepts

I used a home-made Fortran code made by Fernando Delgado to solve the many body multiorbital Hubbard Hamiltonian and compute the current and transition rates, as it was shown in the cotunneling section of this thesis. Here I just discuss the basic principles of the model and assumptions made to solved it. Full details about the code requires much more time than we have at our disposal and we encourage to ask directly to the code's creator for a better understanding of it. The goal of this appendix is then to give a general idea of how the many body multiorbital Hubbard Hamiltonian is managed.

A.1 Multiorbital Hubbard Model

As we explicitly said in Sec. 3.2, we have used a multiorbital Hubbard model to describe a magnetic atom (MA) embedded in a non-magnetic matrix or surface. This model only includes d orbitals of the partially filled shells of the magnetic atom (MA). The system is described as a close quantum system with N_0 electrons, where one electron can hope between the MA and the surface orbitals. The many body Hamiltonian includes four terms, electron-electron, crystal-field and ligand field, spin-orbit and Zeeman interactions:

$$\hat{\mathcal{H}} = \lambda_{\mathrm{Coul}}\hat{\mathcal{H}}_{\mathrm{Coul}} + \lambda_{\mathrm{CF}}\hat{\mathcal{H}}_{\mathrm{CF}} + \lambda_{\mathrm{SO}}\hat{\mathcal{H}}_{\mathrm{SO}} + \hat{\mathcal{H}}_{\mathrm{Zeem}}. \tag{A.1}$$

The dimensionless parameters $\lambda_{\mathrm{X}} \in [0-1]$ permits us to switch off each of these contributions independently for analysis reasons or to control its strength in order to achieve a

satisfactory result. The first term of Eq. (A.1) is

$$H_{\text{Coul}} = \frac{1}{2} \sum_{\ell,\ell' j,j'} V_{\ell j \ell' j'} \sum_{\sigma\sigma'} d^{\dagger}_{\ell\sigma} d^{\dagger}_{j\sigma'} d_{j'\sigma'} d_{\ell'\sigma} \tag{A.2}$$

where $d^{\dagger}_{\ell\sigma}$ ($d_{\ell\sigma}$) denotes the creation (annihilation) operator of an electron with spin σ in the ℓ orbital of the magnetic atom, denoted by $\phi_{\ell}(\vec{r})$, assumed to be equal to the product of a radial hydrogenic function (with effective charge Z and a effective Bohr radius a_{μ}) and a spherical harmonic. Under these approximations, the Coulomb integrals $V_{\ell j \ell' j'}$ can be calculated analytically in terms of the Wigner 3-j symbols and the Slater integrals $F^{n}(3d)$ and $F^{n}(4s)$ [94]. Since all the Coulomb integrals $V_{ij,kl}$ scales with the effective charge, we fix the strength of the electron-electron interaction by a single parameter, the average on-site Coulomb repulsion $U \equiv \langle U_{ll,ll} \rangle$ [82]. We took the values $F^{0} = 4.675(U-J)/5$ eVÅ^{-1}, $F^{2} = 1.94878(U-J)/5$ eV Å^{-1} and $F^{4} = 1.18173(U-J)/5$ eVÅ^{-1}.

The second term in Eq. (A.1) corresponds to the crystal field Hamiltonian, which we write as

$$\hat{\mathcal{H}}_{\text{CF}} = \sum_{\ell,\ell'} \langle \ell | \hat{\mathcal{H}}_{\text{CF}} | \ell' \rangle \sum_{\sigma} d^{\dagger}_{\ell\sigma} d_{\ell'\sigma},$$

where the braket corresponds to the single-particle elements of the potential created by the neighbouring atoms, which are modeled as point charges. Later on in this appendix we will explain the fundamentals of it.

The third term in Eq. (A.1) describes the spin-orbit coupling, which is assumed to be non-zero only on the MA orbitals

$$\hat{\mathcal{H}}_{\text{SO}} = \zeta \sum_{\ell\ell',\sigma\sigma'} \langle \ell\sigma | \vec{L} \cdot \vec{S} | \ell'\sigma' \rangle d^{\dagger}_{\ell\sigma} d_{\ell'\sigma'},$$

where ζ is the single particle spin-orbit coupling of the d-electrons. This term is also frequently expressed as $\lambda \vec{L} \cdot \vec{S}$, with $\vec{L}$ the total angular momentum [55]. The last term in Eq. (A.1) corresponds to the Zeeman Hamiltonian:

$$\hat{\mathcal{H}}_{\text{Zeem}} = \hat{\mathcal{H}}_{\text{Zeem-MA}} = \mu_B \vec{B} \cdot \sum_{\ell\ell',\sigma\sigma'} \langle \ell, \sigma | \left(\vec{L} + g\vec{S} \right) | \ell'\sigma' \rangle d^{\dagger}_{\ell\sigma} d_{\ell'\sigma'},$$

being the g-factor equal to 2.

For our particular case, Fe on MgO/Ag(001), the lambda factors used are $\lambda_{\mathrm{coul}} = 1$, $\lambda_{\mathrm{CF}} = 1$, $\lambda_{\mathrm{SO}} = 0.6$, and $\zeta = 0.05$ eV. We took a value of $U = 5.208$ eV, in agreement with typical values of U found in the literature [95, 96]. DFT calculation suggest an occupation of the Fe orbitals of approximately $4s^0 3d^6$. As the Fe *d*-levels lie in the gap opened by the MgO layer, a significant partial occupation of the surface orbitals is not expected, which makes the point charge model more adequate. This leads to a ground state multiplet corresponding to $S = 2$, in agreement with the experimental results [7, 10, 45].

A.2 Point Charge Model (PCM)

Essentially, the point charge model is a simplified model of a crystal lattice in which ligands are presented as point charges, and hence, the screening effects of the outer shell are excluded. This allows us not only to determine the potential at a given point, but to integrate the potential created by each charge over the whole electronic cloud corresponding to every *d*-orbital of the MA, which carries most of the symmetry of the system [97]. Then, the crystal field Hamiltonian is evaluated in the atomic bases set as explained elsewhere [81]. The results are parametrized in terms of the expectation values of the radial coordinate operators $\langle r^2 \rangle$ and $\langle r^4 \rangle$ [55]. The charges and positions are estimated from the DFT calculations.

Here we have taken the free ion atomic values of $\langle r^2 \rangle = 0.39\text{Å}$ and $\langle r^4 \rangle = 0.35\text{Å}$. The atomic charges and positions are given in Table A.1. Instead of correcting the $\langle r^2 \rangle$ and $\langle r^4 \rangle$ parameters due to covalency and other limitations of the model, we have taken the λ_{SO} as another fitting parameter, with an optimal value of $\lambda_{\mathrm{SO}} \approx 0.6$.

Atom	x (Å)	y (Å)	z (Å)	q (e)
O	0	0	−1.93	−0.70
Mg	0	−2.18	−2.31	0.82
Mg	2.18	0	−2.31	0.82
Mg	−2.18	0	−2.31	0.82
Mg	0	2.18	−2.31	0.82

Table A.1: Positions with respect to the Fe magnetic atom and charges from Badder analysis of the DFT results used for the point charge model calculation. Notice that only the firsts four Mg atoms and the O underneath have been included.

Appendix B

Energy integrals $\mathcal{I}^{\pm}(x, E_c, y)$

The following energy integrals can be done analytically by deformation in the complex energy plane

$$\mathcal{I}^{\pm}(\epsilon_0, E_c, \mu) = \mathcal{P} \int_{-E_c}^{E_c} d\epsilon \frac{n_F^{\pm}(\epsilon - \mu)}{\epsilon_0 - \epsilon}.$$

where $n_F^+ = n_F$ and $n_F^- = 1 - n_F$. The results are given by

$$\mathcal{I}^{+}(\epsilon_0, E_c, \mu) \approx \quad \ln(2\pi) - \ln(E_c - \mu + \epsilon_0) + \mathrm{Re}\left[\psi^{(0)}\left(\frac{1}{2} - \frac{i(\epsilon_0 - \mu)}{2\pi}\right)\right], \tag{B.1}$$

and

$$\mathcal{I}^{-}(\epsilon_0, E_c, \mu) \approx \ln\left|\frac{\epsilon_0 - E_c}{\epsilon_0 + E_c}\right| - \mathcal{I}^{+}(\epsilon_0, E_c, \mu). \tag{B.2}$$

where $\psi^{(0)}(x)$ is the digamma function and the arguments satisfy $-\epsilon_0 + \mu < E_c < \epsilon_0 - \mu$. The above approximations correspond to asymptotic expansions for $E_c \gg 1$. Notice that here we have used a description in terms of dimensionless variables, which is equivalent to measure all energies in units of $k_B T$. In the case of interest, $E_c \gg 1$ and $E_c/\epsilon_0 \sim 1$. In this limit, to lowest order in $1/E_c$, we have that

$$\mathcal{I}^{\pm}(\epsilon_0, E_c, \mu) \sim \mp \ln\left(\frac{1}{1 + \epsilon_0/E_c}\right).$$

Appendix C

Terms $\sum_\sigma \sigma \gamma_{ab}^{m^\pm}(\sigma,\sigma)$ in the Rabi flop rate

Following the assumptions in Sec. 3.2.1, we consider the scattering of the itinerant electrons with a localized magnetic impurity described by a single-orbital state, with a spin $S > 1/2$ (multiplicity $(2S+1)$) in its N_0 electrons state, and isotropic spins $S_{m_+} = S+(-1)^{c_+}/2$ and $S_{m_-} = S-(-1)^{c_-}/2$ in the charge states M_+ and M_-. In this situation, the Rabi flop rate is proportional to sum of the next two equations:

$$\sum_\sigma \sigma \gamma_{ab}^{m^-}(\sigma,\sigma) = \sum_\sigma \sigma \langle a|d_\sigma^\dagger|m_-\rangle\langle m_-|d_\sigma|b\rangle \tag{C.1}$$

$$\sum_\sigma \sigma \gamma_{ab}^{m^+}(\sigma,\sigma) = \sum_\sigma \sigma \langle a|d_\sigma|m_+\rangle\langle m_+|d_\sigma^\dagger|b\rangle. \tag{C.2}$$

States $|a\rangle$ and $|b\rangle$ are eigenstates of a spin Hamiltonian where the quantization axis is the x direction so

$$|a\rangle = \sum_m \phi_m^a |S,m\rangle \quad |b\rangle = \sum_{m'} \phi_{m'}^b |S,m'\rangle, \tag{C.3}$$

where ϕ_m^n are just the coefficients to change the basis from the spin Hamltonian one to the eigenstates of the neutral charge Hamiltonian, $\langle S,m|Q=0,N_0;n\rangle$. m is the S_x spin proyection. Since the spin in the $Q=\pm$ are isotropic we have

$$|m_+\rangle = |Q_-,N_0+1;m+\rangle = |S_{m_+},m_+\rangle \tag{C.4}$$

$$|m_-\rangle = |Q=+,N_0-1;m-\rangle = |S_{m_-},m_-\rangle. \tag{C.5}$$

Again, $m_\pm$ are the x spin proyection of charge states $Q = \pm$. Let us focus on $Q = -$ case first. Following the idea of [98], the creation of one electron in $|m_-\rangle$ can be written as $d_\sigma^\dagger|m_-\rangle = |S_{m_-}, m_-; 1/2, \sigma\rangle$, which is the coupling of the created electron with spin proyection σ and the spin state of the system with one less electron. Now, if we apply the braket in Eq. C.1, we will get a Clebsch-Gordan coefficient (CG) following the notation: $CG_{J,M}^{m_1,m_2} = \langle j_1, m_1; j_2, m_2|J, M\rangle$, $M = m_1 + m_2, J = |j_1 \pm j_2|$ with $j_1 > j_2$) that is different from zero only if $m_- + \sigma = m$. Also, $S = S_{m_-} \pm 1/2$. Therefore, by making use of Eqs. (3.7.60-3.7.63) from Sakurai [89], page 214, we are able to write down that:

$$|S, m\rangle = \sum_\sigma \sum_{m_-} |S_{m_-}, m_-; 1/2, \sigma\rangle\langle S_{m_-}, m_-; 1/2, \sigma|S, m\rangle =$$

$$\sqrt{\frac{S_{m_-} \mp m + 1/2}{2S_{m_-}+1}}|S_{m_-}, m + 1/2; 1/2, -1/2\rangle \pm \sqrt{\frac{S_{m_-} \pm m + 1/2}{2S_{m_-}+1}}|S_{m_-}, m - 1/2; 1/2, 1/2\rangle.$$

Since the state $|m_\rangle$ in Eq. C.1 is common to the states $|a\rangle$ and $|b\rangle$, a $\delta_{mm'}$ will appear and we can not have terms $\phi_m^a\phi_{m'}^b$, with $m \neq m'$. Therefore, by ortogonality, Eq. (C.1) become:

$$\sum_\sigma \sigma\gamma_{ab}^{m^-}(\sigma,\sigma) = -\frac{1}{2}\left(\sum_m \phi_m^{*a}\sqrt{\frac{S_{m_-} \mp m + 1/2}{2S_{m_-}+1}}\right)\left(\sum_{m'} \phi_{m'}^b\sqrt{\frac{S_{m_-} \mp m' + 1/2}{2S_{m_-}+1}}\right)\delta_{mm'}$$

$$\frac{1}{2}\left(\pm\sum_m \phi_m^{*a}\sqrt{\frac{S_{m_-} \pm m + 1/2}{2S_{m_-}+1}}\right)\left(\pm\sum_{m'} \phi_{m'}^b\sqrt{\frac{S_{m_-} \pm m' + 1/2}{2S_{m_-}+1}}\right)\delta_{mm'} =$$

$$-\frac{1}{2}\left(\sum_m \phi_m^{*a}\phi_m^b\frac{S_{m_-} \mp m + 1/2}{2S_{m_-}+1}\right) + \frac{1}{2}\left(\sum_m \phi_m^{*a}\phi_m^b\frac{S_{m_-} \pm m + 1/2}{2S_{m_-}+1}\right) = \frac{\pm 1}{2S_{m_-}+1}\left(\sum_m m\phi_m^{*a}\phi_m^b\right)$$

$$\implies \sum_\sigma \sigma\gamma_{ab}^{m^-}(\sigma,\sigma) = \pm\frac{1}{2S \pm 1 + 1}\langle a|S_x|b\rangle. \tag{C.6}$$

The plus sign associated to $S = S_{m_-} + 1/2$ and minus sign to $S = S_{m_-} - 1/2$. Same procedure can be done for the $|m_+\rangle$ state but now we create the electron in the neutral charge state. Taking into account that $S_{m_+} = S \pm 1/2$ and $m_+ = m + \sigma$ we have

$$|S_{m_+}, m_+\rangle = \sqrt{\frac{S \mp m + 1/2}{2S+1}}|S, m; 1/2, -1/2\rangle \pm \sqrt{\frac{S \pm m + 1/2}{2S+1}}|S, m; 1/2, 1/2\rangle.$$

Therefore

$$\sum_{\sigma} \sigma \gamma_{ab}^{m^+}(\sigma,\sigma) = -\frac{1}{2}\left(\sum_{m} \phi_m^{*a}\phi_m^b \frac{S \mp m + 1/2}{2S+1}\right) + \frac{1}{2}\left(\sum_{m} \phi_m^{*a}\phi_m^b \frac{S \pm m + 1/2}{2S+1}\right) =$$

$$\pm\frac{1}{2}\frac{1}{2S+1}\left(\sum_{m} 2m\phi_m^{*a}\phi_m^b\right)$$

$$\Longrightarrow \sum_{\sigma} \sigma \gamma_{ab}^{m^+}(\sigma,\sigma) = \pm\frac{1}{2S+1}\langle a|S_x|b\rangle. \tag{C.7}$$

Introducing $S_{m_+} = S + (-1)^{c_+}/2$ and $S_{m_-} = S - (-1)^{c_-}/2$ where c_+ and c_- can take the values 0 or 1 we have

$$\Omega \propto \sum_{\sigma} \sigma\left(\gamma_{ab}^{m^-}(\sigma,\sigma) + \gamma_{ab}^{m^+}(\sigma,\sigma)\right) = \langle a|S_x|b\rangle\left(\frac{(-1)^{c_-}}{2S+1+(-1)^{c_-}} + \frac{(-1)^{c_+}}{2S+1}\right). \tag{C.8}$$

And we can write Eq. 3.4.

Appendix D

Basic Keldysh formalism

More inside can be found in [73]. The name of the technique takes its origin from the 1964 paper of L. V. Keldysh [99]. Essentially, instead of using the time-ordering operator of the equilibrium theory, Keldysh proposed the contour-ordering operator which orders the time-labels according to their order on the Keldysh contour. Thus, a Green's Function is defined as

$$G^c(t,t') = -i\langle T_C[\phi(t)\phi^\dagger(t')]\rangle$$

where T_C is the contour-ordered operator. $\phi(t)$ ($\phi^\dagger(t)$) is creation (anniquilation) operator that follows the Wick's theorem [71]. The contour is shown is Fig. D.1 and it consists of two parts. The upper C_+ from $-\infty$ to $+\infty$ and the branch below C_- going backwards. Depending on where the two times variables t and t' are, the result would lead to one of the four linearly independent Green's Function:

$$G(t,t') = \begin{cases} G^a(t,t') = i\theta(t'-t)\langle\{\phi(t),\phi^\dagger(t')\}\rangle \;\; t,t' \in C_+ \\ G^r(t,t') = -i\theta(t-t')\langle\{\phi(t),\phi^\dagger(t')\}\rangle \;\; t,t' \in C_- \\ G^>(t,t') = -i\langle\phi(t)\phi^\dagger(t')\rangle \;\; t \in C_-, t' \in C_+ \\ G^<(t,t') = i\langle\phi^\dagger(t')\phi(t)\rangle \;\; t \in C_+, t' \in C_- \end{cases}. \tag{D.1}$$

Here we have introduced the advanced, retarded, greater and lesser Green's Function respectively. The curly brackets denote an anticommutator. It worths to mention Eq.

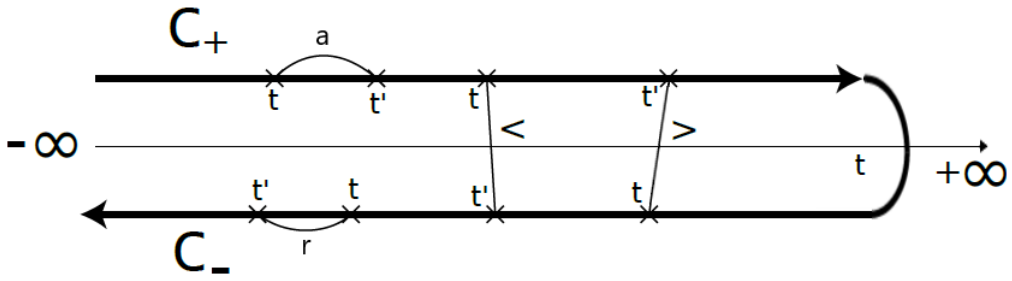

Figure D.1: Keldysh contour C. There are two branches: C_+ going from $-\infty$ to $+\infty$ and the branch below C_- going backwards. The relative position of the times t and t' in the branches provides one of the four possible functions. Each of them is marked in the picture.

(D.1) denotes that only three functions are linearly independent since $G^r - G^a = G^> - G^<$. This reflects the freedom of choice that the Green's Functions have [73].

Another important result to consider is the *Langreth Theorem*. We restrict ourself to the two product case for simplicity so we have

$$C(t,t') = \int_C d\tau A(t,\tau)B(\tau,t'). \tag{D.2}$$

For what is concerned, we only write the lesser particular case which is

$$C^<(t,t') = \int_{-\infty}^{+\infty} d\tau \left[A^r(t,\tau)B^<(\tau,t') + A^<(t,\tau)B^a(\tau,t')\right]. \tag{D.3}$$

Same can be applied for the greater function replacing "<" for ">". The retarded and advanced functions follow a simple product [73].

Appendix E

Derivation of the Floquet master equation

This appendix provides an inside in the algebra used to get the master equation (2.44) from Eq. (2.39). If we substitute the mixed Green's function into the equation of motion (2.39) we have

$$\dot{\rho}_{lj}(t) = \frac{i}{\hbar}(E_l - E_j)\rho_{lj}(t) + \frac{1}{\hbar}\sum_{\alpha k\sigma}\left[\sum_u w_\alpha(t)\lambda_{ul\sigma}G^<_{uj,\alpha k\sigma}(t,t) - \right.$$

$$\left.\sum_v w_\alpha(t)\lambda_{jv\sigma}G^<_{lv,\alpha k\sigma}(t,t) + \sum_u w^*_\alpha(t)\mu_{ul\sigma}G^<_{\alpha k\sigma,uj}(t,t) - \sum_v w^*_\alpha(t)\mu_{jv\sigma}G^<_{\alpha k\sigma,lv}(t,t)\right]. \quad \text{(E.1)}$$

Introducing the definitions

$$\Lambda_{lj,\alpha\sigma}(t) = \int dt_1 \sum_{uv}\mu_{uv\sigma}\left[g^r_{lj,uv}(t,t_1)\Sigma^<_{\alpha\sigma}(t_1,t) + g^<_{lj,uv}(t,t_1)\Sigma^a_{\alpha\sigma}(t_1,t)\right] \quad \text{(E.2)}$$

$$\bar{\Lambda}_{\alpha\sigma,lj}(t) = \int dt_1 \sum_{uv}\lambda_{uv\sigma}\left[\Sigma^r_{\alpha\sigma}(t,t_1)g^<_{uv,lj}(t_1,t) + \Sigma^<_{\alpha\sigma}(t,t_1)g^a_{uv,lj}(t_1,t)\right], \quad \text{(E.3)}$$

with the self-energy being

$$\Sigma^c_{\alpha\sigma}(t,t') = \sum_k w^*_\alpha(t)g^c_{\alpha k\sigma}(t-t')w_\alpha(t'), \quad \text{(E.4)}$$

we can rewrite Eq. (E.1) as follows:

$$\dot{\rho}_{lj}(t) = \frac{i}{\hbar}(E_l - E_j)\rho_{lj}(t) + \frac{1}{\hbar}\sum_{\alpha\sigma}\left[\sum_u \lambda_{ul\sigma}\Lambda_{uj,\alpha\sigma}(t) - \sum_v \lambda_{jv\sigma}\Lambda_{lv,\alpha\sigma}(t) + \sum_u \mu_{ul\sigma}\bar{\Lambda}_{\alpha\sigma,uj}(t) - \sum_v \mu_{jv\sigma}\bar{\Lambda}_{\alpha\sigma,lv}(t)\right], \tag{E.5}$$

Equations (E.2) and (E.3) would be Fourier-Floquet transformed later. We will see that this procedure simplifies the calculation because we will end up with a simple multiplication in the frequency domain of the self-energy and the isolated Green's function of the system. To this end, let us compute the Fourier-Floquet selfenergy first, Eq. (E.4). The Green's function of the reservoirs does not have a periodic structure, which means it follows a simple Fourier transformation. Contrary, the tunneling can be written as a Fourier series so we write:

$$\Sigma^c_{\alpha\sigma}(t_1,t_2) = \sum_n w^*_{\alpha n}e^{in\omega t_1}\sum_k \frac{1}{2\pi}\int_{-\infty}^{+\infty} d\varepsilon g^c_{\alpha k\sigma}(\varepsilon)e^{-i\varepsilon(t_1-t_2)}\sum_{n'} w_{\alpha n'}e^{-in'\omega t_2} = \frac{1}{2\pi}\sum_{nn'k}\int_{-\infty}^{+\infty} d\varepsilon e^{-i(\varepsilon-n\omega)t_1+i(\varepsilon-n'\omega)t_2}w^*_{\alpha,n}g^c_{\alpha k\sigma}(\varepsilon)w_{\alpha,n'}.$$

Making the change of variable $-n = n$ and $-n' = n'$ we have

$$\Sigma^c_{\alpha\sigma}(t_1,t_2) = \frac{1}{2\pi}\sum_{nn'}\int_{-\infty}^{+\infty} d\varepsilon e^{-i(\varepsilon/\hbar+n\omega)t_1+i(\varepsilon/\hbar+n'\omega)t_2}\sum_k w^*_{\alpha,-n}g^c_{\alpha k\sigma}(\varepsilon)w_{\alpha,-n'}, \tag{E.6}$$

where the Fourier-Floquet components of the tunneling are

$$w_{\alpha,n} = \frac{w^0_\alpha}{T}\int_{-T/2}^{T/2} dt(1 + A_\alpha\cos(\omega t))e^{-in\omega t} = w^0_\alpha\left[\delta_{n,0} + \frac{A_\alpha}{2}(\delta_{n,1} + \delta_{n,-1})\right]. \tag{E.7}$$

Giving that $\omega = 2\pi/T$, with T the period, and n is an integer number, we can rewrite Eq. (E.6) as:

$$\Sigma^c_{\alpha\sigma,nn'}(\varepsilon) = \sum_k |w^0_\alpha|^2\left[\delta_{n,0} + \frac{A_\alpha}{2}(\delta_{n,-1} + \delta_{n,1})\right]g^c_{\alpha k\sigma}(\varepsilon)\left[\delta_{n',0} + \frac{A_\alpha}{2}(\delta_{n',-1} + \delta_{n',1})\right]. \tag{E.8}$$

n and n' are called the Floquet numbers. With the Fourier-Floquet components of the self-energy, the only thing left is to compute the isolated Green's funcions of the system

and its Fourier transform. We have

$$g^{<}_{uv,lj}(t,t') = i\langle\hat{\rho}_{lj}(t')\hat{\rho}_{uv}(t)\rangle. \tag{E.9}$$

Following the equation of motion for the uncoupled central system Hamiltonian, Eq. (2.37), $\dot{\hat{\rho}}_{lj}(t) = \frac{i}{\hbar}(E_l - E_j)\hat{\rho}_{lj}(t)$, then $\hat{\rho}_{lj}(t) = \hat{\rho}_{lj}(0)e^{\frac{i}{\hbar}(E_l-E_j)t}$, which implies

$$g^{<}_{uv,lj}(t_1,t) = i\langle\hat{\rho}_{lj}(0)\hat{\rho}_{uv}(0)\rangle e^{\frac{i}{\hbar}(E_u-E_v)t_1}e^{\frac{i}{\hbar}(E_l-E_j)t} = i\langle\hat{\rho}_{lv}(0)\rangle\delta_{ju}e^{\frac{i}{\hbar}((E_u-E_v)t_1+(E_l-E_j)t)}.$$

We wish to obtain a lesser Green's function that only depends on a time difference, making the future Fourier transform easier to compute. If we divide and multiply this last equation by $e^{-i(E_l-E_j+E_u-E_v)t/\hbar} = e^{-iEt/\hbar}$ then

$$g^{<}_{uv,lj}(t_1,t) = i\langle\hat{\rho}_{lv}(0)\rangle\delta_{ju}\frac{e^{\frac{i}{\hbar}(E_u-E_v)(t_1-t)}}{e^{-iEt/\hbar}}.$$

In other words, $g^{<}_{uv,lj}(t_1,t)e^{-iEt/\hbar}$ only depends on a time difference which what we are looking for. Similarly, the greater Green's function is

$$g^{>}_{uv,lj}(t_1,t) = -i\langle\hat{\rho}_{uv}(t_1)\hat{\rho}_{lj}(t)\rangle\frac{e^{-iEt/\hbar}}{e^{-iEt/\hbar}} = -i\langle\hat{\rho}_{uj}(0)\rangle\delta_{vl}e^{\frac{i}{\hbar}(E_u-E_v)(t_1-t)}/e^{-iEt/\hbar}.$$

From the greater and the lesser Green's functions we can compute the retarded and advanced ones as

$$g^{r}_{uv,lj}(t_1,t) = \theta(t_1-t)\left[g^{>}_{uv,lj}(t_1,t) - g^{<}_{uv,lj}(t_1,t)\right]e^{-iEt/\hbar}/e^{-iEt/\hbar} =$$

$$-i\theta(t_1-t)e^{\frac{i}{\hbar}(E_u-E_v)(t_1-t)}(\langle\hat{\rho}_{uj}(0)\rangle\delta_{vl} + \langle\hat{\rho}_{lv}(0)\rangle\delta_{ju})e^{iEt/\hbar}$$

$$g^{a}_{uv,lj}(t_1,t) = -\theta(t-t_1)\left[g^{>}_{uv,lj}(t_1,t) - g^{<}_{uv,lj}(t_1,t)\right]e^{-iEt/\hbar}/e^{-iEt/\hbar} =$$

$$i\theta(t-t_1)e^{\frac{i}{\hbar}(E_u-E_v)(t_1-t)}(\langle\hat{\rho}_{uj}(0)\rangle\delta_{vl} + \langle\hat{\rho}_{lv}(0)\rangle\delta_{ju})e^{iEt/\hbar}.$$

Notice that if we combine the terms $\langle\hat{\rho}_{uj}(0)\rangle\delta_{vl}$ (or equivalently $\langle\hat{\rho}_{lv}(0)\rangle\delta_{ju}$) with the exponential $e^{iEt} = e^{i(\cancel{E_l}-E_j+E_u-\cancel{E_v})t}$, where the energies E_l and E_v cancel out due to δ_{vl}, we have $\rho_{uj}(t)$ as a result of applying the Heisenberg equation and making the mean value over $\hat{\rho}_0$. This implies that all the exponentials with E can be absorbed into the $\hat{\rho}_{lj}(0)$. This

will be later taken into account when we write the Fourier form of the Green's function. Apart from terms like $g^c_{uv,lj}(t_1,t)$, we will have $g^c_{lj,uv}(t,t_1)$. We need to divide and multiply by $e^{-i(E_l-E_j+E_u-E_v)t/\hbar} = e^{-iEt/\hbar}$ in this case, which will lead to terms proportional to $\hat{\rho}_{lj}(0)$ that will depend on the first time t. This is actually crucial since we want to take them out of the integrals in Eqs. (E.2) and (E.3). So

$$g^<_{lj,uv}(t,t_1) = i\langle\hat{\rho}_{uj}(0)\rangle\delta_{vl}e^{\frac{i}{\hbar}((E_l-E_j)t+(E_u-E_v)t_1)}\frac{e^{-iEt/\hbar}}{e^{-iEt/\hbar}} =$$

$$i\rho_{uj}(t)\delta_{vl}e^{-\frac{i}{\hbar}(E_u-E_v)(t-t_1)} = \rho_{uj}(t)\delta_{vl}f^<_{uv}(t-t_1). \tag{E.10}$$

And we can write

$$g^r_{lj,uv}(t,t_1) = -i\theta(t-t_1)e^{-\frac{i}{\hbar}(E_u-E_v)(t-t_1)}e^{iEt}(\langle\hat{\rho}_{lv}(0)\rangle\delta_{ju} + \langle\hat{\rho}_{uj}(0)\rangle\delta_{vl}) =$$

$$f^r_{uv}(t-t_1)(\rho_{lv}(t)\delta_{ju} + \rho_{uj}(t)\delta_{vl}).$$

Where we have introduced the functions $f^c_{uv}(t-t_1)$ that only depend on a time difference. In summary, we have found that

$$\Lambda_{lj,\alpha\sigma} \implies g^c_{lj,uv}(t,t_1) \implies e^{-\frac{i}{\hbar}(E_u-E_v)(t-t_1)}.$$

Similarly

$$\bar{\Lambda}_{\alpha\sigma,lj} \implies g^c_{uv,lj}(t_1,t) \implies e^{-\frac{i}{\hbar}(E_v-E_u)(t_1-t)}. \tag{E.11}$$

We emphasized that we have a $\Delta_{uv} = E_u - E_v$ dependence in $\Lambda_{lj,\alpha\sigma}$ and a Δ_{vu} in $\bar{\Lambda}_{\alpha\sigma,lj}$. The functions $f^c_{uv}(t-t_1)$ can be easily Fourier transformed since they only depends on a time difference:

$$\frac{1}{2\pi}\int_{-\infty}^{+\infty} d\varepsilon f^c_{uv(vu)}(\varepsilon)e^{-i\varepsilon(t-t_1)}.$$

being $f^c_{uv(vu)}(\varepsilon)$ the Fourier transform of the object.

At this point, we just need to replace the self-energy and the Green's function of the central system into a kind of first term of $\Lambda_{lj,\alpha\sigma}$. Ordering the time of integrats leads to

$$\sum_{uv}\mu_{uv\sigma}\int_{-\infty}^{+\infty}\frac{d\varepsilon}{2\pi}f^c_{uv}(\varepsilon)e^{-i\varepsilon t}\sum_{nn'}\int_{-\infty}^{+\infty}\frac{d\varepsilon'}{2\pi}\Sigma^c_{\alpha\sigma,nn'}(\varepsilon')e^{i(\varepsilon'+n'\omega)t}\underbrace{\int_{-\infty}^{+\infty}dt_1e^{-i(\varepsilon'+n\omega)t_1}e^{i\varepsilon t_1}}_{2\pi\delta(\varepsilon-\varepsilon'-n\omega)}.$$

No kronecker delta appears because the energies can have any value. The Dirac delta allows us to write

$$\frac{1}{2\pi}\sum_{uv\sigma}\mu_{uv\sigma}\sum_{nn'}\int_{-\infty}^{+\infty}d\varepsilon f^c_{uv}(\varepsilon)\Sigma^c_{\alpha\sigma,nn'}(\varepsilon-n\omega)e^{i(n'-n)\omega t}.$$

Therefore

$$\Lambda_{lj,\alpha\sigma}(t)=\frac{1}{2\pi}\sum_{uv}\mu_{uv\sigma}(\rho_{lv}(t)\delta_{ju}+\rho_{uj}(t)\delta_{vl})\sum_{nn'}e^{i(n'-n)\omega t}\int_{-\infty}^{+\infty}d\varepsilon f^r_{uv}(\varepsilon)\Sigma^<_{\alpha\sigma,nn'}(\varepsilon-n\omega)+$$
$$\frac{1}{2\pi}\sum_{uv}\mu_{uv}\rho_{uj}(t)\delta_{vl}\sum_{nn'}e^{i(n'-n)\omega t}\int_{-\infty}^{+\infty}d\varepsilon f^<_{uv}(\varepsilon)\Sigma^a_{\alpha\sigma,nn'}(\varepsilon-n\omega). \tag{E.12}$$

If we now introduce the following η definitions

$$\begin{aligned}\eta'_{ul,\alpha\sigma}(t)&=\frac{1}{2\pi}\mu_{ul\sigma}\sum_{nn'}e^{i(n'-n)\omega t}\int_{-\infty}^{+\infty}d\varepsilon\left[f^r_{ul}(\varepsilon)\Sigma^<_{\alpha\sigma,nn'}(\varepsilon-n\omega)+g^<_{ul}(\varepsilon)\Sigma^a_{\alpha\sigma,nn'}(\varepsilon-n\omega)\right]\\ \eta_{jv,\alpha\sigma}(t)&=\frac{1}{2\pi}\mu_{jv\sigma}\sum_{nn'}e^{i(n'-n)\omega t}\int_{-\infty}^{+\infty}d\varepsilon f^r_{jv}(\varepsilon)\Sigma^<_{\alpha\sigma,nn'}(\varepsilon-n\omega),\end{aligned} \tag{E.13}$$

we can rewrite $\Lambda_{lj,\alpha\sigma}$ as simple as

$$\Lambda_{lj,\alpha\sigma}(t)=\sum_v\rho_{lv}(t)\eta_{jv,\alpha\sigma}(t)+\sum_u\rho_{uj}(t)\eta'_{ul,\alpha\sigma}(t). \tag{E.14}$$

Moreover, we have to compute $\bar{\Lambda}_{\alpha\sigma,lj}$ which contains term like

$$\sum_{uv}\lambda_{uv\sigma}\sum_{nn'}\int_{-\infty}^{+\infty}\frac{d\varepsilon'}{2\pi}\Sigma^c_{\alpha\sigma,nn'}(\varepsilon')e^{-i(\varepsilon'+n\omega)t}\int_{-\infty}^{+\infty}\frac{d\varepsilon}{2\pi}f^c_{vu}(\varepsilon)e^{i\varepsilon t}\underbrace{\int_{-\infty}^{+\infty}dt_1e^{i(\varepsilon'+n'\omega)t_1}e^{-i\varepsilon t_1}}_{2\pi\delta(\varepsilon'+n'\omega-\varepsilon)}$$
$$\implies\frac{1}{2\pi}\sum_{uv\sigma}\lambda_{uv\sigma}\sum_{nn'}\int_{-\infty}^{+\infty}d\varepsilon\Sigma^c_{\alpha\sigma,nn'}(\varepsilon-n'\omega)f^c_{vu}(\varepsilon)e^{-i(n-n')\omega t}.$$

So

$$\bar{\Lambda}_{\alpha\sigma,lj}(t)=\frac{1}{2\pi}\sum_{uv}\lambda_{uv\sigma}(\rho_{uj}(t)\delta_{vl}+\rho_{lv}(t)\delta_{ju})\sum_{nn'}e^{-i(n-n')\omega t}\int_{-\infty}^{+\infty}d\varepsilon\Sigma^<_{\alpha\sigma,nn'}(\varepsilon-n'\omega)f^a_{vu}(\varepsilon)+$$
$$\frac{1}{2\pi}\sum_{uv}\lambda_{uv\sigma}\rho_{lv}(t)\delta_{ju}\sum_{nn'}e^{-i(n-n')\omega t}\int_{-\infty}^{+\infty}d\varepsilon\Sigma^r_{\alpha\sigma,nn'}(\varepsilon-n'\omega)f^<_{vu}(\varepsilon). \tag{E.15}$$

Introducing now the following γ definitions

$$\gamma'_{\alpha\sigma,jv}(t) = \frac{\lambda_{jv\sigma}}{2\pi}\sum_{nn'} e^{-i(n-n')\omega t}\int_{-\infty}^{+\infty} d\varepsilon\left[\Sigma^{r}_{\alpha\sigma,nn'}(\varepsilon - n'\omega)f^{<}_{vj}(\varepsilon) + \Sigma^{<}_{\alpha\sigma,nn'}(\varepsilon - n'\omega)f^{a}_{vj}(\varepsilon)\right]$$
$$\gamma_{\alpha\sigma,ul}(t) = \frac{\lambda_{ul\sigma}}{2\pi}\sum_{nn'} e^{-i(n-n')\omega t}\int_{-\infty}^{+\infty} d\varepsilon\Sigma^{<}_{\alpha\sigma,nn'}(\varepsilon - n'\omega)f^{a}_{lu}(\varepsilon), \tag{E.16}$$

we can write

$$\bar{\Lambda}_{\alpha\sigma,lj}(t) = \sum_{u}\rho_{uj}(t)\gamma_{\alpha\sigma,ul}(t) + \sum_{v}\rho_{lv}(t)\gamma'_{\alpha\sigma,jv}(t). \tag{E.17}$$

With all this, let us go back to the master equation (E.5) changing a bit the notation in order to avoid mistakes. Particulary, we change u by l' and v by j' in Eq. (E.5) and we have

$$\begin{aligned}\dot{\rho_{lj}}(t) = \frac{i}{\hbar}(E_l - E_j)\rho_{lj}(t) + \frac{1}{\hbar}\sum_{\alpha\sigma}\Bigg[&\sum_{l'}\lambda_{l'l\sigma}\left(\sum_{v}\rho_{l'v}(t)\eta_{jv,\alpha\sigma}(t) + \sum_{u}\rho_{uj}(t)\eta'_{ul',\alpha\sigma}(t)\right)\\ &-\sum_{j'}\lambda_{jj'\sigma}\left(\sum_{v}\rho_{lv}(t)\eta_{j'v,\alpha\sigma}(t) + \sum_{u}\rho_{uj'}(t)\eta'_{ul,\alpha\sigma}(t)\right)\\ &+\sum_{l'}\mu_{l'l\sigma}\left(\sum_{u}\rho_{uj}(t)\gamma_{\alpha\sigma,ul'}(t) + \sum_{v}\rho_{l'v}(t)\gamma'_{\alpha\sigma,jv}(t)\right)\\ &-\sum_{j'}\mu_{jj'\sigma}\left(\sum_{u}\rho_{uj'}(t)\gamma_{\alpha\sigma,ul}(t) + \sum_{v}\rho_{lv}(t)\gamma'_{\alpha\sigma,j'v}(t)\right)\Bigg],\end{aligned} \tag{E.18}$$

where we have taken into account Eqs. (E.14) and (E.17). We can do $l' = j'$ and $u = v$ allowing $l' = v$ after that. Hence, if we now reorder the terms in a certain way while renaming accordingly the indexes, we have

$$\begin{aligned}\dot{\rho}_{lj}(t) = \frac{i}{\hbar}(E_l - E_j)\rho_{lj}(t) + \frac{1}{\hbar}\sum_{\alpha\sigma vu}\Big[&(\lambda_{vl\sigma}\eta_{ju,\alpha\sigma}(t) + \mu_{vl\sigma}\gamma'_{\alpha\sigma,ju}(t))\rho_{vu}(t)\\ &+(\mu_{vl\sigma}\gamma_{\alpha\sigma,uv}(t) + \lambda_{vl\sigma}\eta'_{uv,\alpha\sigma}(t))\rho_{uj}(t) - (\lambda_{jv\sigma}\eta_{vu,\alpha\sigma}(t) + \mu_{jv\sigma}\gamma'_{\alpha\sigma,vu}(t))\rho_{lu}(t)\\ &-(\mu_{jv\sigma}\gamma_{\alpha\sigma,ul}(t) + \lambda_{jv\sigma}\eta'_{ul,\alpha\sigma}(t))\rho_{uv}(t)\Big].\end{aligned} \tag{E.19}$$

Hence, by introducing these rates into the equation of motion of the reduced density matrix (E.19), we find

$$\hbar\dot{\rho}_{lj}(t) - i\Delta_{lj}\rho_{lj}(t) = \sum_{vu}\left[\Gamma_{vl,ju}(t)\rho_{vu}(t) + \bar{\Gamma}_{vl,uv}(t)\rho_{uj}(t) - \Gamma_{jv,vu}(t)\rho_{lu}(t) - \bar{\Gamma}_{jv,ul}(t)\rho_{uv}(t)\right]. \tag{E.20}$$

Arriving finally to the master equation of the main text. The rates are computed in the Appendix F, which is the next one.

Appendix F

Explicit form of the Rates

In this appendix we calculate the different self-energies and Green's functions that we need in order to compute the rates (2.47) and (2.50). According to our definition, Eq. (E.8), the advanced and retarded self-energies are

$$\Sigma^{r,a}_{\alpha\sigma,nn'}(\varepsilon) = |t^0_\alpha|^2 \sum_k g^{r,a}_{\alpha k\sigma}(\varepsilon) \left[\delta_{n,0} + \frac{A_\alpha}{2}\left(\delta_{n,-1} + \delta_{n,1}\right)\right]\left[\delta_{n',0} + \frac{A_\alpha}{2}\left(\delta_{n',-1} + \delta_{n',1}\right)\right].$$

Since the electronic Green's function is

$$g^{r,a}_{\alpha k\sigma}(t-t') = \mp i\theta(\pm t \mp t')e^{-i\xi_{\alpha k\sigma}(t-t')/\hbar},$$

where upper sign is associated to the retarded Green's function and lower sign to the advanced one, the Fourier transform leads to

$$g^{r,a}_{\alpha k\sigma}(\varepsilon) = \mp i \int_{-\infty}^{+\infty} d(t-t')\theta(\pm t \mp t')e^{-i\xi_{\alpha k\sigma}(t-t')/\hbar} e^{i\varepsilon(t-t')} =$$

$$-\lim_{\chi\to 0^+} i \int_0^{\pm\infty} d(t-t')e^{i(\varepsilon-\xi_{\alpha k\sigma}/\hbar \pm i\chi)(t-t')}$$

Therefore, we can write

$$g^{r,a}_{\alpha k\sigma}(\varepsilon) = [\varepsilon \pm i0^+ - \xi_{\alpha k\sigma}/\hbar]^{-1}.$$

Notice that $g^a_{\alpha k\sigma}(\varepsilon) = g^{r*}_{\alpha k\sigma}(\varepsilon)$, and the same goes for the self-energy. We need to perform the sum over k. A trick to make it is to transform the sum into a integral over the energy:

$\sum_k \to \int_{-\infty}^{+\infty} d\xi_{\alpha k\sigma}\rho_{\alpha\sigma}(\xi_{\alpha k\sigma})/\hbar$, being $\rho_\alpha(\xi_{\alpha k\sigma})$ the density of states of the metal. We take the wide band limit, where ρ_α is constant up to a cut-off energy and 0 otherwise. If we now use the Lehmann representation we can write

$$\lim_{y\to 0^+}\int_{-\infty}^{+\infty}\frac{dx}{x\pm iy}\rho_{\alpha\sigma}(\varepsilon-x)=\lim_{y\to 0^+}\int_{-\infty}^{+\infty}dx\left(\frac{x}{x^2+y^2}\rho_{\alpha\sigma}(\varepsilon-x)\mp i\frac{y}{x^2+y^2}\rho_{\alpha\sigma}(\varepsilon-x)\right)$$

$$=P\left(\int_{-\infty}^{+\infty}\frac{dx}{x}\rho_{\alpha\sigma}(\varepsilon-x)\right)\mp i\pi\int_{-\infty}^{+\infty}dx\rho_{\alpha\sigma}(\varepsilon-x)\delta(x),$$

where P stands for the Cauchy principal part and x is equal to $\varepsilon-\xi_{\alpha k\sigma}/\hbar$ for us. The principal part is zero if the density of states $\rho_\alpha(\varepsilon-x)$ does not depend strongly on x, so that it can be taken out of the integral, i.e., $\rho_{\alpha\sigma}(\varepsilon-x)=\rho_{\alpha\sigma}(\varepsilon)$. In any case, since $\rho_{\alpha\sigma}$ does not depend on $\xi_{\alpha k\sigma}$ in wide band limit, so we can write

$$\Sigma^{r,a}_{\alpha\sigma,nn'}(\varepsilon)=\mp i\frac{\Gamma_{\alpha\sigma}}{2}\left[\delta_{n,0}+\frac{A_\alpha}{2}\left(\delta_{n,-1}+\delta_{n,1}\right)\right]\left[\delta_{n',0}+\frac{A_\alpha}{2}\left(\delta_{n',-1}+\delta_{n',1}\right)\right], \tag{F.1}$$

where we have defined the coupling constant $\Gamma_{\alpha\sigma}=2\pi\rho_{\alpha\sigma}|t^0_\alpha|^2$. Since we are assuming the wide band limit, $\Gamma_{\alpha\sigma}$ is constant between $-E_c$ and E_c, and zero otherwise. In addition to this

$$g^<_{\alpha k\sigma}(t-t')=in_F(\xi_{\alpha k\sigma})e^{-i\xi_{\alpha k\sigma}(t-t')/\hbar},$$

which leads to

$$g^<_{\alpha k\sigma}(\varepsilon)=2\pi i n_F(\xi_{\alpha k\sigma})\delta(\varepsilon-\xi_{\alpha k\sigma}/\hbar).$$

Again, we rewrite the sum over k as a integral over $\xi_{\alpha k\sigma}$. The result is quite straightforward: $2\pi i\rho_\alpha n_F(\hbar\varepsilon)$. Thus

$$\Sigma^<_{\alpha\sigma,nn'}(\varepsilon)=i\Gamma_{\alpha\sigma}n_F(\hbar\varepsilon)\left[\delta_{n,0}+\frac{A_\alpha}{2}\left(\delta_{n,-1}+\delta_{n,1}\right)\right]\left[\delta_{n',0}+\frac{A_\alpha}{2}\left(\delta_{n',-1}+\delta_{n',1}\right)\right]$$

Now we just need to compute the Fourier transform of the functions $f^c_{uv}(\varepsilon)$, Eq. (E.11), in the previous Appendix. The advanced and retarded functions are quite similar to the electronic ones

$$f^{ra}_{uv}(t-t_1)=\mp i\theta(\pm t\mp t_1)e^{-i(E_u-E_v)(t-t_1)/\hbar}$$

So

$$f_{uv}^{ra}(\varepsilon) = \mp i \int_{-\infty}^{+\infty} d(t-t_1)\theta(\pm t \mp t_1) e^{-i(E_u - E_v)(t-t_1)/\hbar} e^{i\varepsilon(t-t_1)} = [\varepsilon - \Delta_{uv}/\hbar \pm i0^+]^{-1}$$

These functions can be separated into imaginary and real parts

$$\Re f_{uv}^{a}(\varepsilon) = \Re f_{uv}^{r}(\varepsilon) = \frac{\varepsilon - \Delta_{uv}/\hbar}{(\varepsilon - \Delta_{uv}/\hbar)^2 + \chi^2}$$

$$\Im f_{uv}^{a}(\varepsilon) = -\Im f_{uv}^{r}(\varepsilon) = \frac{\chi}{(\varepsilon - \Delta_{uv}/\hbar)^2 + \chi^2} = \pi\delta(\varepsilon - \Delta_{uv}/\hbar).$$

For the lesser function we have that

$$f_{uv}^{<}(\varepsilon) = 2\pi i \delta(\varepsilon - \Delta_{uv}/\hbar)).$$

We have identified the imaginary part as a delta function because $\chi \to 0^+$. Let us now introduce everything into Eq. (2.47). We assumed a wide band limit that introduced a cut-off energy E_c. Although E_c is a raw approximation, it ensures us that the real part of the functions $f_{uv}^{ra}(\varepsilon)$ converge. In this situation, the imaginary parts of the rates always cancel out because we find differences between a Γ_{ijji} and a $\bar{\Gamma}_{jiij}$ in the master equation for any population equation. Therefore, only the real part of the rates survives. When this difference do not appear (coherence equation or Rabi terms), the imaginary part of the rates that survives can be thought as a energy renormalization term[1]. So we can write

$$\Gamma_{vl,ju;n'} = \frac{1}{2}\sum_{n\alpha\sigma}\left(\lambda_{vl\sigma}\mu_{ju\sigma}\Gamma_{\alpha\sigma} n_F(\Delta_{ju} - n\hbar\omega)\left[\delta_{n,n'} + \frac{A_\alpha}{2}\left(\delta_{n,n'+1} + \delta_{n,n'-1}\right)\right] - \right.$$

$$\left.\mu_{vl\sigma}\lambda_{ju\sigma}\Gamma_{\alpha\sigma}(n_F(\Delta_{uj} - n\hbar\omega) - 1)\left[\delta_{n,-n'} + \frac{A_\alpha}{2}\left(\delta_{n,-n'+1} + \delta_{n,-n'-1}\right)\right]\right)\left[\delta_{n,0} + \frac{A_\alpha}{2}\left(\delta_{n,1} + \delta_{n,-1}\right)\right]. \tag{F.2}$$

Making the sum of n we have

$$\Gamma_{vl,ju;n'} = \frac{1}{2}\sum_{\alpha\sigma}\left(\lambda_{al\sigma}\mu_{ju\sigma}\Gamma_{\alpha\sigma} n_F(\Delta_{ju} + \hbar\omega)\left[\delta_{n',-1} + \frac{A_\alpha}{2}\left(\delta_{n',-2} + \delta_{n',0}\right)\right] - \right.$$

[1]This statement is in general true but the terms that we are discarting can provide interesting results in the frequency spectra, mostly because of the Rabi terms. It is something that we need to investigate in future works.

$$\mu_{vl\sigma}\lambda_{ju\sigma}\Gamma_{\alpha\sigma}(n_F(\Delta_{uj}+\hbar\omega)-1)\left[\delta_{n',1}+\frac{A_\alpha}{2}(\delta_{n',2}+\delta_{n',0})\right]\Big)\frac{A_\alpha}{2}$$

$$+\frac{1}{2}\sum_{\alpha\sigma}\Big(\lambda_{vl\sigma}\mu_{ju\sigma}\Gamma_{\alpha\sigma}n_F(\Delta_{ju})\left[\delta_{n',0}+\frac{A_\alpha}{2}(\delta_{n',-1}+\delta_{n',1})\right]-$$

$$\mu_{vl\sigma}\lambda_{ju\sigma}\Gamma_{\alpha\sigma}(n_F(\Delta_{uj})-1)\left[\delta_{n',0}+\frac{A_\alpha}{2}(\delta_{n',1}+\delta_{n',-1})\right]\Big)$$

$$+\frac{1}{2}\sum_{\alpha\sigma}\Big(\lambda_{vl\sigma}\mu_{ju\sigma}\Gamma_{\alpha\sigma}n_F(\Delta_{ju}-\hbar\omega)\left[\delta_{n',1}+\frac{A_\alpha}{2}(\delta_{n',0}+\delta_{n',2})\right]-$$

$$\mu_{vl\sigma}\lambda_{ju\sigma}\Gamma_{\alpha\sigma}(n_F(\Delta_{uj}-\hbar\omega)-1)\left[\delta_{n',-1}+\frac{A_\alpha}{2}(\delta_{n',0}+\delta_{n',-2})\right]\Big)\frac{A_\alpha}{2}. \tag{F.3}$$

Similarly we can write

$$\bar{\Gamma}_{jv,ul;n'}=-\frac{1}{2}\sum_{n\alpha\sigma}\Big(\mu_{ja\sigma}\lambda_{ul\sigma}\Gamma_{\alpha\sigma}n_F(\Delta_{lu}-n\hbar\omega)\left[\delta_{n,-n'}+\frac{A_\alpha}{2}(\delta_{n,-n'+1}+\delta_{n,-n'-1})\right]-$$

$$\lambda_{jv\sigma}\mu_{ul\sigma}\Gamma_{\alpha\sigma}(n_F(\Delta_{ul}-n\hbar\omega)-1)\left[\delta_{n,n'}+\frac{A_\alpha}{2}(\delta_{n,n'+1}+\delta_{n,n'-1})\right]\Big)\left[\delta_{n,0}+\frac{A_\alpha}{2}(\delta_{n,1}+\delta_{n,-1})\right]. \tag{F.4}$$

Computing the sum of n we have

$$\bar{\Gamma}_{jv,ul;n'}=-\frac{1}{2}\sum_{\alpha\sigma}\Big(\mu_{ja\sigma}\lambda_{ul\sigma}\Gamma_{\alpha\sigma}n_F(\Delta_{lu}+\hbar\omega)\left[\delta_{n',1}+\frac{A_\alpha}{2}(\delta_{n',2}+\delta_{n',0})\right]-$$

$$\lambda_{jv\sigma}\mu_{ul\sigma}\Gamma_{\alpha\sigma}(n_F(\Delta_{ul}+\hbar\omega)-1)\left[\delta_{n',-1}+\frac{A_\alpha}{2}(\delta_{n',-2}+\delta_{n',0})\right]\Big)\frac{A_\alpha}{2}$$

$$-\frac{1}{2}\sum_{\alpha\sigma}\Big(\mu_{jv\sigma}\lambda_{ul\sigma}\Gamma_{\alpha\sigma}n_F(\Delta_{lu})\left[\delta_{n',0}+\frac{A_\alpha}{2}(\delta_{n',1}+\delta_{n',-1})\right]-$$

$$\lambda_{jv\sigma}\mu_{ul\sigma}\Gamma_{\alpha\sigma}(n_F(\Delta_{ul})-1)\left[\delta_{n',0}+\frac{A_\alpha}{2}(\delta_{n',-1}+\delta_{n',1})\right]\Big)$$

$$-\frac{1}{2}\sum_{\alpha\sigma}\Big(\mu_{jv\sigma}\lambda_{ul\sigma}\Gamma_{\alpha\sigma}n_F(\Delta_{lu}-\hbar\omega)\left[\delta_{n',-1}+\frac{A_\alpha}{2}(\delta_{n',0}+\delta_{n',-2})\right]-$$

$$\lambda_{jv\sigma}\mu_{ul\sigma}\Gamma_{\alpha\sigma}(n_F(\Delta_{ul}-\hbar\omega)-1)\left[\delta_{n',1}+\frac{A_\alpha}{2}(\delta_{n',0}+\delta_{n',2})\right]\Big)\frac{A_\alpha}{2}. \tag{F.5}$$

Equations (F.4) and (F.5) show us that the index n' can take only the values $-2, -1, 0, 1, 2$, therefore, in Eq. (2.52), a fixed n is connected to four different Floquet numbers: from $n-2$ to $n+2$.

Appendix G

Indications for the Floquet program

Here we will introduce the basic points to take into account for the ERS Floquet simulation code. The ket basis applied is the following

$$(\{-1/2,-S;1/2,-S;0,-S\},\{-1/2,-S+1;1/2,-S+1;0,-S+1\}\ldots\{-1/2,S;1/2,S;0,S\})\,.$$

With this basis we just simply compute the eigenvector and eigenvalues of the system using the matrix representation of the central system Hamiltonian

$$H_S=\sum_{mp}\varepsilon_{pm}(t)|p,m\rangle\langle p,m|+\sum_{m}^{S-1}(J_+|\downarrow,m+1\rangle\langle\uparrow,m|+J_-|\uparrow,m\rangle\langle\downarrow,m+1|)$$

$$+\frac{g\mu_B}{2}\sum_{m}^{S-1}B_+J_-\,(|\uparrow,m\rangle\langle\uparrow,m+1|+|\downarrow,m\rangle\langle\downarrow,m+1|+|0,m\rangle\langle 0,m+1|)$$

$$+\frac{g\mu_B}{2}\sum_{m}^{S-1}B_-J_+\,(|\uparrow,m+1\rangle\langle\uparrow,m|+|\downarrow,m+1\rangle\langle\downarrow,m|+|0,m+1\rangle\langle 0,m|)$$

$$+\frac{g\mu_B}{2}(B_+|\downarrow,m\rangle\langle\uparrow,m|+B_-|\uparrow,m\rangle\langle\downarrow,m|),$$

where $\varepsilon_{pm}=(\varepsilon_\sigma+Jm\sigma+g\mu_BB_z\sigma)\delta_{\sigma p}+g\mu_BB_zm+D(m+\sigma\delta_{p,\sigma})^2$ while J_+ and J_- are equals to $J\sqrt{S(S+1)-m(m+1)}/2$ and $B_+=B_x+iB_y$, $B_-=B_x-iB_y$. The second sum over m cannot reach the value $m=S$. Notice that we have chosen the particular case of a spin S coupled to a $s=1/2$ with a empty state. If the lector wish to introduce another

spin Hamiltonian with a more complex structure, such as spin-chain, the basis should be changed accordingly. The next step would be to compute the rates $\Gamma_{vl,ju;n}$ in order to write the matrix form of the Floquet master equation

$$(E_l - E_j)\rho_{lj;n} + n\hbar\omega\rho_{lj;n} = \\ i\sum_{vu;n'}\left[\Gamma_{vl,ju;n'}\rho_{vu;n-n'} + \bar{\Gamma}_{vl,uv;n'}\rho_{uj;n-n'} - \Gamma_{jv,vu;n'}\rho_{lu;n-n'} - \bar{\Gamma}_{jv,ul;n'}\rho_{uv;n-n'}\right],$$

in a matrix form $Ax = 0$ being x a row vector that contains all the $\rho_{lj,n}$ components i.e. all indices l, j and n that our problem has. In fact, due to the form of the rates

$$(E_l - E_j)\rho_{lj;n} + n\hbar\omega\rho_{lj;n} = i\sum_{au}\left[\Gamma_{al,ju;0}\rho_{au;n} + \bar{\Gamma}_{al,ua;0}\rho_{uj;n} - \Gamma_{ja,au;0}\rho_{lu;n} - \bar{\Gamma}_{ja,ul;0}\rho_{ua;n}\right] + \\ i\sum_{au}\left[\Gamma_{al,ju;-1}\rho_{au;n+1} + \bar{\Gamma}_{al,ua;-1}\rho_{uj;n+1} - \Gamma_{ja,au;-1}\rho_{lu;n+1} - \bar{\Gamma}_{ja,ul;-1}\rho_{ua;n+1}\right] + \\ i\sum_{au}\left[\Gamma_{al,ju;-2}\rho_{au;n+2} + \bar{\Gamma}_{al,ua;-2}\rho_{uj;n+2} - \Gamma_{ja,au;-2}\rho_{lu;n+2} - \bar{\Gamma}_{ja,ul;-2}\rho_{ua;n+2}\right] + \\ i\sum_{au}\left[\Gamma_{al,ju;1}\rho_{au;n-1} + \bar{\Gamma}_{al,ua;1}\rho_{uj;n-1} - \Gamma_{ja,au;1}\rho_{lu;n-1} - \bar{\Gamma}_{ja,ul;1}\rho_{ua;n-1}\right] \\ i\sum_{au}\left[\Gamma_{al,ju;2}\rho_{au;n-2} + \bar{\Gamma}_{al,ua;2}\rho_{uj;n-2} - \Gamma_{ja,au;2}\rho_{lu;n-2} - \bar{\Gamma}_{ja,ul;2}\rho_{ua;n-2}\right].$$

Which suggests a ρ vector of the form:

$$\rho_S = \Big(\rho_{11,n_i}, \rho_{12,n_i}, \cdots \rho_{1j_{max},n_i}, \rho_{21,n_i}, \cdots \rho_{l_{max}1,n_i}, \cdots \rho_{l_{max}j_{max},n_i}, \cdots \\ \rho_{11,n_f}, \rho_{12,n_f}, \cdots \rho_{1j_{max},n_f}, \rho_{21,n_f}, \cdots \rho_{l_{max}1,n_f}, \cdots \rho_{l_{max}j_{max},n_f}\Big). \tag{G.1}$$

Being $l_{max} = j_{max} = 3(2S+1)$ and n_i, n_f the first and last floquet number respectively, $n_i < n_f$. The Floquet master equation needs to be cut by chosing a maximum and minimum Floquet number to keep. Giving n, we will have that $n_i = n_0 - n_{cut_1}$ and $n_f = n_0 + n_{cut_2}$, with the $n_{cut_j} > 1$ being the Floquet number cut-off. Therefore, if we choose, for example, $n_{cut_1} = 2$ and $n_{cut_2} = 3$ we will have $3(2S+1)(n_{cut_1} + n_{cut_2} + 1) = 18(2S+1)$ equations. The value n_0 can be freely chosen, however, since one always wants to include the zero Floquet equation, which contains the detailed balance, it is convenient to fix it at zero.

The detailed balance becomes essential to break the linear dependence of the master equation. It reads as $\sum_l \rho_{ll} = 1$ which implies $\sum_{ln} e^{-in\omega t}\rho_{ll;n} = 1$. Multiplying by $e^{in'\omega t}$ and integrating over t, we obtain $\sum_l \rho_{ll;n} = \delta_{n,0}$. Therefore, the dimension of ρ_S is reduced by $(n_{cut_1} + n_{cut_2} + 1)$.

The matrix that multiplies the vector ρ_S is

$$\begin{pmatrix} Rateblock_0 & Rateblock_{-1} & Rateblock_{-2} & 0 & 0 & \cdots & 0 \\ Rateblock_1 & Rateblock_0 & Rateblock_{-1} & Rateblock_{-2} & 0 & \cdots & 0 \\ Rateblock_2 & Rateblock_1 & Rateblock_0 & Rateblock_{-1} & Rateblock_{-2} & \cdots & 0 \\ \vdots & & & \ddots & & & \vdots \\ 0 & \cdots & 0 & Rateblock_2 & Rateblock_1 & Rateblock_0 & Rateblock_{-1} \\ 0 & \cdots & 0 & 0 & Rateblock_2 & Rateblock_1 & Rateblock_0 \end{pmatrix}. \tag{G.2}$$

Every rate block is a matrix with dimension $9(2S+1)(2S+1) - 1$. We substract one since the detailed balance have been applied. Then, the matrix (G.2) has a total dimension of $[(3(2S+1)-1)(n_{cut_1} + n_{cut_2} + 1)]^2$. In general, a row of the rateblock is

$$Rateblock_{n'}(l,j) = \Big(\Gamma_{1l,j1;n'} - \bar{\Gamma}_{j1,1l;n'} \quad \Gamma_{1l,j2;n'} - \bar{\Gamma}_{j2,1l;n'} \cdots \quad \Gamma_{1l,jj;n'} - \bar{\Gamma}_{jj,1l;n'} + \textstyle\sum_u \bar{\Gamma}_{ul,1u;n'}$$

$$\cdots \quad \Gamma_{1l,ju_{max};n'} - \bar{\Gamma}_{ju_{max},1l;n'} \quad \Gamma_{2l,j1;n'} - \bar{\Gamma}_{j1,2l;n'} \quad \Gamma_{2l,j2;n'} - \bar{\Gamma}_{j2,2l;n'} - \Gamma_{1l,j1;n'}$$

$$\cdots \quad \Gamma_{ll,j1;n'} - \bar{\Gamma}_{j1,ll;n'} - \textstyle\sum_v \Gamma_{jv,v1;n'} \quad \cdots \quad \Gamma_{v_{max}l,ju_{max};n'} - \bar{\Gamma}_{jv_{max},u_{max}l;n'}.\Big)$$

In order to make clear how the detailed balance is introduced, let us focus on the $n = 0$ case alone, so l and j cannot be both equal to one. Thus, the master equation reads as

$$(E_l - E_j)\rho_{lj;0} = i\sum_{vu}\left[\Gamma_{vl,ju;0}\rho_{vu;0} + \bar{\Gamma}_{vl,uv;0}\rho_{uj;0} - \Gamma_{jv,vu;0}\rho_{lu;0} - \bar{\Gamma}_{jv,ul;0}\rho_{uv;0}\right].$$

The sum will contain terms with $\rho_{11;0} = 1 - \sum_{k>1}\rho_{kk;0}$ so we can write

$$\begin{aligned} -i(E_l - E_j)\rho^0_{lj;0} = &\sum_{vu}\Gamma_{vl,ju;0}\rho_{vu;0}(1-\delta_{v,1}\delta_{u,1}) - \sum_{k>1}\Gamma_{1l,j1;0}\rho_{kk;0} + \Gamma_{1l,j1;0} \\ &+ \sum_{vu}\bar{\Gamma}_{vl,uv;0}\rho_{uj;0}(1-\delta_{j,1}\delta_{u,1}) - \sum_{v,k>1}\delta_{1,j}\bar{\Gamma}_{vl,1v;0}\rho_{kk;0} + \sum_v \delta_{1,j}\bar{\Gamma}_{vl,1v;0} \\ &- \sum_{vu}\Gamma_{jv,vu;0}\rho_{lu;0}(1-\delta_{l,1}\delta_{u,1}) + \sum_{v,k>1}\delta_{1,l}\Gamma_{jv,v1;0}\rho_{kk;0} - \sum_v \delta_{1,l}\Gamma_{jv,v1;0} \end{aligned}$$

$$-\sum_{vu}\bar{\Gamma}_{jv,ul;0}\rho_{uv;0}(1-\delta_{v,1}\delta_{u,1})+\sum_{k>0}\bar{\Gamma}_{j1,1l;0}\rho_{kk;0}-\bar{\Gamma}_{j1,1l;0}.$$

Where we have use the kronecker deltas to indicate that the sums over v and u do not contain the element $v = 1$, $u = 1$. If we extend this to the other Floquet numbers that includes the zero Floquet number, we have a system of equation of the form $Ax = B$ with $B \neq 0$ due to the constrain that the detailed balance adds.

Bibliography

[1] Tadahiro Komeda. "Chemical identification and manipulation of molecules by vibrational excitation via inelastic tunneling process with scanning tunneling microscopy". In: *Progress in Surface Science* 78.2 (2005), pp. 41–85. ISSN: 0079-6816. DOI: 10.1016/j.progsurf.2005.05.001. URL: http://www.sciencedirect.com/science/article/pii/S0079681605000262 (visited on 03/08/2013) (cit. on p. 12).

[2] Jean-Pierre Gauyacq, Nicolas Lorente, and Frederico Dutilh Novaes. "Excitation of local magnetic moments by tunneling electrons". In: *Progress in Surface Science* 87.5?8 (2012), pp. 63–107. ISSN: 0079-6816. DOI: http://dx.doi.org/10.1016/j.progsurf.2012.05.003 (cit. on p. 12).

[3] Y. Manassen et al. "Direct observation of the precession of individual paramagnetic spins on oxidized silicon surfaces". In: *Phys. Rev. Lett.* 62 (21 May 1989), pp. 2531–2534. DOI: 10.1103/PhysRevLett.62.2531. URL: https://link.aps.org/doi/10.1103/PhysRevLett.62.2531 (cit. on p. 13).

[4] D. Shachal and Y. Manassen. "Mechanism of electron-spin resonance studied with use of scanning tunneling microscopy". In: *Phys. Rev. B* 46 (8 Aug. 1992), pp. 4795–4805. DOI: 10.1103/PhysRevB.46.4795. URL: https://link.aps.org/doi/10.1103/PhysRevB.46.4795 (cit. on p. 13).

[5] Alexander V. Balatsky, Mitsuaki Nishijima, and Yishay Manassen. "Electron spin resonance-scanning tunneling microscopy". In: *Advances in Physics* 61.2 (2012), pp. 117–152. DOI: 10.1080/00018732.2012.668775. URL: https://doi.org/10.1080/00018732.2012.668775 (cit. on p. 13).

[6] Stefan Müllegger et al. "Radio Frequency Scanning Tunneling Spectroscopy for Single-Molecule Spin Resonance". In: *Phys. Rev. Lett.* 113 (13 Sept. 2014), p. 133001. DOI: 10.1103/PhysRevLett.113.133001. URL: https://link.aps.org/doi/10.1103/PhysRevLett.113.133001 (cit. on pp. 13, 14).

[7] Susanne Baumann et al. "Electron paramagnetic resonance of individual atoms on a surface". In: *Science* 350.6259 (2015), pp. 417–420. DOI: 10.1126/science.aac8703 (cit. on pp. 13, 18, 37, 71, 73, 74, 76, 77, 79, 81, 82, 104, 112, 120).

[8] Stefan Müllegger et al. "Mechanism for nuclear and electron spin excitation by radio frequency current". In: *Phys. Rev. B* 92 (22 Dec. 2015), p. 220418. DOI: 10.1103/PhysRevB.92.220418. URL: https://link.aps.org/doi/10.1103/PhysRevB.92.220418 (cit. on pp. 13, 18).

[9] Sebastian Loth et al. "Measurement of Fast Electron Spin Relaxation Times with Atomic Resolution". In: *Science* 329.5999 (2010), pp. 1628–1630. DOI: 10.1126/science.1191688 (cit. on p. 13).

[10] William Paul et al. "Control of the millisecond spin lifetime of an electrically probed atom". In: *Nature Physics* 13.4 (2017), pp. 403–407 (cit. on pp. 13, 78, 120).

[11] Taeyoung Choi et al. "Atomic-scale sensing of the magnetic dipolar field from single atoms". In: *Nature nanotechnology* 12.5 (2017), p. 420 (cit. on pp. 13, 18, 37, 71, 76, 77, 81, 112).

[12] Philip Willke et al. "Magnetic Resonance Imaging of Single Atoms". arXiv:1807.08944. 2018 (cit. on pp. 13, 18, 37, 71, 76, 77, 81, 112).

[13] Fabian D Natterer et al. "Reading and writing single-atom magnets". In: *Nature* 543.7644 (2017), pp. 226–228 (cit. on pp. 13, 15, 16, 18, 37, 71, 76, 77, 81, 112).

[14] Philip Willke et al. "Probing quantum coherence in single-atom electron spin resonance". In: *Science Advances* 4.2 (2018). DOI: 10.1126/sciadv.aaq1543. eprint: http://advances.sciencemag.org/content/4/2/eaaq1543.full.pdf (cit. on pp. 13, 18, 37, 71, 73, 76, 77, 78, 79, 80, 81, 82, 87, 96, 112).

[15] Kai Yang et al. "Engineering the Eigenstates of Coupled Spin-1/2 Atoms on a Surface". In: *Phys. Rev. Lett.* 119 (22 Nov. 2017), p. 227206. DOI: 10.1103/PhysRevLett.119.227206. URL: https://link.aps.org/doi/10.1103/PhysRevLett.119.227206 (cit. on pp. 13, 14, 18, 37, 71, 73, 76, 77, 81, 84, 104, 106, 112).

[16] Philip Willke et al. "Hyperfine interaction of individual atoms on a surface". In: *Science* 362.6412 (2018), pp. 336–339. ISSN: 0036-8075. DOI: 10.1126/science.aat7047. eprint: http://science.sciencemag.org/content/362/6412/336.full.pdf. URL: http://science.sciencemag.org/content/362/6412/336 (cit. on pp. 13, 18, 37, 71, 73, 76, 77, 81, 112).

[17] Kai Yang et al. "Electrically controlled nuclear polarization of individual atoms". In: *Nature nanotechnology* 13.12 (2018), p. 1120 (cit. on pp. 14, 16, 17, 18, 37, 71, 76, 77, 81, 112).

[18] T. S. Seifert et al. "Single-atom electron paramagnetic resonance in a scanning tunneling microscope driven by a radio-frequency antenna at 4 K". In: *Phys. Rev. Research* 2 (1 Jan. 2020), p. 013032. DOI: 10.1103/PhysRevResearch.2.013032. URL: https://link.aps.org/doi/10.1103/PhysRevResearch.2.013032 (cit. on p. 15).

[19] Tom S. Seifert et al. "Longitudinal and transverse electron paramagnetic resonance in a scanning tunneling microscope". In: *Science Advances* 6.40 (2020). DOI: 10.1126/sciadv.abc5511. eprint: https://advances.sciencemag.org/content/6/40/eabc5511.full.pdf. URL: https://advances.sciencemag.org/content/6/40/eabc5511 (cit. on p. 15).

[20] Kai Yang et al. "Coherent spin manipulation of individual atoms on a surface". en. In: *Science* 366.6464 (Oct. 2019), pp. 509–512. ISSN: 0036-8075, 1095-9203. DOI: 10.1126/science.aay6779. URL: http://www.sciencemag.org/lookup/doi/10.1126/science.aay6779 (visited on 01/23/2020) (cit. on p. 17).

[21] E. M. Chudnovsky, D. A. Garanin, and R. Schilling. "Universal mechanism of spin relaxation in solids". In: *Phys. Rev. B* 72 (9 Sept. 2005), p. 094426. DOI: 10.1103/PhysRevB.72.094426. URL: https://link.aps.org/doi/10.1103/PhysRevB.72.094426 (cit. on p. 18).

[22] C. Calero and E. M. Chudnovsky. "Rabi Spin Oscillations Generated by Ultrasound in Solids". en. In: *Physical Review Letters* 99.4 (July 2007). ISSN: 0031-9007, 1079-7114. DOI: 10.1103/PhysRevLett.99.047201. URL: https://link.aps.org/doi/10.1103/PhysRevLett.99.047201 (visited on 11/14/2018) (cit. on p. 18).

[23] Peter Berggren and Jonas Fransson. "Electron paramagnetic resonance of single magnetic moment on a surface". In: *Scientific reports* 6 (2016), p. 25584 (cit. on p. 18).

[24] J. L. Lado, A. Ferrón, and J. Fernández-Rossier. "Exchange mechanism for electron paramagnetic resonance of individual adatoms". In: *Phys. Rev. B* 96 (20 Nov. 2017), p. 205420. DOI: 10.1103/PhysRevB.96.205420. URL: https://link.aps.org/doi/10.1103/PhysRevB.96.205420 (cit. on pp. 18, 42).

[25] Alexey M Shakirov, Alexey N Rubtsov, and Pedro Ribeiro. "Spin-Transfer Torque Induced Paramagnetic Resonance". arXiv:1806.08260. 2018 (cit. on p. 18).

[26] J. Bardeen. "Tunnelling from a Many-Particle Point of View". In: *Phys. Rev. Lett.* 6 (2 Jan. 1961), pp. 57–59. DOI: 10.1103/PhysRevLett.6.57 (cit. on pp. 19, 81).

[27] N. Lorente and M. Persson. "Theory of Single Molecule Vibrational Spectroscopy and Microscopy". In: *Physical Review Letters* 85.14 (Oct. 2000), p. 2997. DOI: 10.1103/PhysRevLett.85.2997. URL: http://link.aps.org/doi/10.1103/PhysRevLett.85.2997 (visited on 09/19/2011) (cit. on pp. 19, 40).

[28] N. Lorente. "Mode excitation induced by the scanning tunnelling microscope". en. In: *Applied Physics A* 78.6 (Mar. 2004), pp. 799–806. ISSN: 0947-8396, 1432-0630. DOI: 10.1007/s00339-003-2434-8. URL: http://link.springer.com/10.1007/s00339-003-2434-8 (visited on 08/21/2018) (cit. on pp. 19, 40).

[29] F Delgado and Joaquín Fernández-Rossier. "Spin decoherence of magnetic atoms on surfaces". In: *Progress in Surface Science* 92.1 (2017), pp. 40–82 (cit. on pp. 20, 36, 42, 75, 91, 93, 104).

[30] Iker Gallardo. "Magnetic properties of Co on different environments". PhD thesis. Centro de Física de Materiales, Donostia, Spain, 2019 (cit. on p. 21).

[31] Richard Korytar. "Molecular Kondo Problem". PhD thesis. Universidad autonoma de Barcelona, Barcelona, Spain, 2011 (cit. on p. 21).

[32] Charles Kittel and Ching-Yao Fong. *Quantum theory of solids*. Vol. 33. Wiley New York; 2nd rev. edition, 1987 (cit. on p. 21).

[33] Brian T. Sutcliffe and R. Guy Woolley. "On the quantum theory of molecules". In: *The Journal of Chemical Physics* 137.22 (2012), 22A544. DOI: 10.1063/1.4755287. eprint: https://doi.org/10.1063/1.4755287. URL: https://doi.org/10.1063/1.4755287 (cit. on p. 21).

[34] Gabriele Giuliani and Giovanni Vignale. *Quantum Theory of the Electron Liquid*. Cambridge University Press, 2005. DOI: 10.1017/CBO9780511619915 (cit. on p. 21).

[35] P. Hohenberg and W. Kohn. "Inhomogeneous Electron Gas". In: *Phys. Rev.* 136 (3B Nov. 1964), B864–B871. DOI: 10.1103/PhysRev.136.B864. URL: https://link.aps.org/doi/10.1103/PhysRev.136.B864 (cit. on p. 21).

[36] W. Kohn and L. J. Sham. "Self-Consistent Equations Including Exchange and Correlation Effects". In: *Phys. Rev.* 140 (4A Nov. 1965), A1133–A1138. DOI: 10.1103/PhysRev.140.A1133. URL: https://link.aps.org/doi/10.1103/PhysRev.140.A1133 (cit. on p. 22).

[37] D. M. Ceperley and B. J. Alder. "Ground State of the Electron Gas by a Stochastic Method". In: *Phys. Rev. Lett.* 45 (7 Aug. 1980), pp. 566–569. DOI: 10.1103/PhysRevLett.45.566. URL: https://link.aps.org/doi/10.1103/PhysRevLett.45.566 (cit. on p. 24).

[38] John P. Perdew, Kieron Burke, and Matthias Ernzerhof. "Generalized Gradient Approximation Made Simple". In: *Phys. Rev. Lett.* 77 (18 Oct. 1996), pp. 3865–3868. DOI: 10.1103/PhysRevLett.77.3865. URL: https://link.aps.org/doi/10.1103/PhysRevLett.77.3865 (cit. on p. 24).

[39] B. Hammer, L. B. Hansen, and J. K. Nørskov. "Improved adsorption energetics within density-functional theory using revised Perdew-Burke-Ernzerhof functionals". In: *Phys. Rev. B* 59 (11 Mar. 1999), pp. 7413–7421. DOI: 10.1103/PhysRevB.59.7413. URL: https://link.aps.org/doi/10.1103/PhysRevB.59.7413 (cit. on p. 24).

[40] Stefan Grimme. "Semiempirical GGA-Type Density Functional Constructed with a Long-Range Dispersion Correction". In: *Journal of computational chemistry* 27 (Nov. 2006), pp. 1787–99. DOI: 10.1002/jcc.20495 (cit. on p. 25).

[41] Mark Casida and M Huix-Rotllant. "Progress in Time-Dependent Density-Functional Theory". In: *Annual review of physical chemistry* 63 (Apr. 2011), pp. 287–323. DOI: 10.1146/annurev-physchem-032511-143803 (cit. on p. 25).

[42] P. E. Blöchl. "Projector augmented-wave method". In: *Phys. Rev. B* 50 (24 Dec. 1994), pp. 17953–17979. DOI: 10.1103/PhysRevB.50.17953. URL: https://link.aps.org/doi/10.1103/PhysRevB.50.17953 (cit. on p. 26).

[43] He Bingling et al. "Ag (1 0 0)/MgO (1 0 0) interface: A van der Waals density functional study". In: *Applied Surface Science* 288 (Jan. 2014), pp. 115–121. DOI: 10.1016/j.apsusc.2013.09.158 (cit. on pp. 27, 66).

[44] Jörg Neugebauer and Matthias Scheffler. "Adsorbate-substrate and adsorbate-adsorbate interactions of Na and K adlayers on Al(111)". In: *Phys. Rev. B* 46 (24 Dec. 1992), pp. 16067–16080. DOI: 10.1103/PhysRevB.46.16067. URL: https://link.aps.org/doi/10.1103/PhysRevB.46.16067 (cit. on p. 27).

[45] S. Baumann et al. "Origin of Perpendicular Magnetic Anisotropy and Large Orbital Moment in Fe Atoms on MgO". In: *Phys. Rev. Lett.* 115 (23 Dec. 2015), p. 237202. DOI: 10.1103/PhysRevLett.115.237202. URL: https://link.aps.org/doi/10.1103/PhysRevLett.115.237202 (cit. on pp. 27, 120).

[46] J. Reina Gálvez et al. "Cotunneling mechanism for all-electrical electron spin resonance of single adsorbed atoms". In: *Phys. Rev. B* 100 (3 July 2019), p. 035411. DOI: 10.1103/PhysRevB.100.035411. URL: https://link.aps.org/doi/10.1103/PhysRevB.100.035411 (cit. on pp. 29, 45, 62, 87).

[47] Heinz-Peter Breuer and Francesco Petruccione. *The theory of open quantum systems*. Oxford University Press, 2002 (cit. on pp. 29, 35, 37, 81).

[48] J. von Neumann. "Mathematische Begründung der Quantenmechanik". In: *Nachrichten von der Gesellschaft der Wissenschaften zu Göttingen, Mathematisch-Physikalische Klasse* 1927 (1927), pp. 1–57. URL: http://eudml.org/doc/59215 (cit. on p. 29).

[49] A. P. Jauho, N. S. Wingreen, and Y. Meir. "Time-dependent transport in interacting an noninteracting resonant-tunneling systems". In: *Phys. Rev. B.* 50 (1994), p. 5528 (cit. on pp. 29, 30).

[50] Daniel W. Hone, Roland Ketzmerick, and Walter Kohn. "Statistical mechanics of Floquet systems: The pervasive problem of near degeneracies". In: *Physical Review E* 79.5 (May 2009). ISSN: 1550-2376. DOI: 10.1103/physreve.79.051129. URL: http://dx.doi.org/10.1103/PhysRevE.79.051129 (cit. on pp. 30, 47).

[51] Claude Cohen-Tannoudji, Gilbert Grynberg, and Jacques Dupont-Roc. *Atom-Photon Interactions*. Wiley and Sons, INC., New York, 1998 (cit. on pp. 36, 37, 81).

[52] Andrei Tokmakoff. *Book: Time Dependent Quantum Mechanics and Spectroscopy (Tokmakoff)*. 2020. URL: https://chem.libretexts.org/Bookshelves/Physical_and_Theoretical_Chemistry_Textbook_Maps/Book%3A_Time_Dependent_Quantum_Mechanics_and_Spectroscopy_(Tokmakoff) (visited on 12/12/2020) (cit. on p. 36).

[53] Patrick P Hofer et al. "Markovian master equations for quantum thermal machines: local versus global approach". In: *New Journal of Physics* 19.12 (Dec. 2017), p. 123037. DOI: 10.1088/1367-2630/aa964f (cit. on p. 37).

[54] J. Onam González et al. "Testing the Validity of the 'Local' and 'Global' GKLS Master Equations on an Exactly Solvable Model". In: *Open Systems & Information Dynamics* 24.04 (2017), p. 1740010. DOI: 10.1142/S1230161217400108 (cit. on p. 37).

[55] A. Abragam and B. Bleaney. *Electron Paramagnetic Resonance of Transition Ions*. Oxford University Press, Oxford, 1970 (cit. on pp. 38, 72, 75, 119, 120).

[56] Albert Messiah. *Quantum Mechanics*. Dover, New York, 1999 (cit. on pp. 41, 87).

[57] F. Delgado and J. Fernández-Rossier. "Cotunneling theory of atomic spin inelastic electron tunneling spectroscopy". In: *Phys. Rev. B* 84 (4 July 2011), p. 045439. DOI: 10.1103/PhysRevB.84.045439 (cit. on pp. 42, 72).

[58] C. A. Klausmeier. "Floquet theory: a useful tool for understanding nonequilibrium dynamics". In: *Theoretical Ecology* 1 (2008), pp. 153–161 (cit. on p. 44).

[59] N. W. Ashcroft and N. D.Mermin. *Solid State Physics*. Thomson Learning, 1976 (cit. on pp. 44, 77).

[60] Liliana Arrachea and Michael Moskalets. "Relation between scattering-matrix and Keldysh formalisms for quantum transport driven by time-periodic fields". In: *Phys. Rev. B* 74 (24 Dec. 2006), p. 245322. DOI: 10.1103/PhysRevB.74.245322. URL: https://link.aps.org/doi/10.1103/PhysRevB.74.245322 (cit. on p. 45).

[61] F. Delgado, C.F. Hirjibehedin, and J. Fernández-Rossier. "Consequences of Kondo exchange on quantum spins". In: *Surface Science* 630 (Dec. 2014), pp. 337–342. ISSN: 0039-6028. DOI: 10.1016/j.susc.2014.07.009. URL: http://dx.doi.org/10.1016/j.susc.2014.07.009 (cit. on p. 45).

[62] Herbert Schoeller and Gerd Schön. "Mesoscopic quantum transport: Resonant tunneling in the presence of a strong Coulomb interaction". In: *Phys. Rev. B* 50 (24 Dec. 1994), pp. 18436–18452. DOI: 10.1103/PhysRevB.50.18436. URL: https://link.aps.org/doi/10.1103/PhysRevB.50.18436 (cit. on p. 47).

[63] Jürgen König, Herbert Schoeller, and Gerd Schön. "Zero-Bias Anomalies and Boson-Assisted Tunneling Through Quantum Dots". In: *Phys. Rev. Lett.* 76 (10 Mar. 1996), pp. 1715–1718. DOI: 10.1103/PhysRevLett.76.1715. URL: https://link.aps.org/doi/10.1103/PhysRevLett.76.1715 (cit. on p. 47).

[64] Jürgen König et al. "Resonant tunneling through ultrasmall quantum dots: Zero-bias anomalies, magnetic-field dependence, and boson-assisted transport". In: *Phys. Rev. B* 54 (23 Dec. 1996), pp. 16820–16837. DOI: 10.1103/PhysRevB.54.16820. URL: https://link.aps.org/doi/10.1103/PhysRevB.54.16820 (cit. on p. 47).

[65] Janine Splettstoesser et al. "Adiabatic pumping through a quantum dot with coulomb interactions: A perturbation expansion in the tunnel coupling". In: *Phys. Rev. B* 74 (8 Aug. 2006), p. 085305. DOI: 10.1103/PhysRevB.74.085305. URL: https://link.aps.org/doi/10.1103/PhysRevB.74.085305 (cit. on p. 47).

[66] Fabio Cavaliere, Michele Governale, and Jürgen König. "Nonadiabatic Pumping through Interacting Quantum Dots". In: *Phys. Rev. Lett.* 103 (13 Sept. 2009), p. 136801.

DOI: 10.1103/PhysRevLett.103.136801. URL: https://link.aps.org/doi/10.1103/PhysRevLett.103.136801 (cit. on p. 47).

[67] M. Moskalets and M. Büttiker. "Floquet scattering theory of quantum pumps". In: *Physical Review B* 66.20 (Nov. 2002). ISSN: 1095-3795. DOI: 10.1103/physrevb.66.205320. URL: http://dx.doi.org/10.1103/PhysRevB.66.205320 (cit. on p. 47).

[68] Bibek Bhandari et al. *From non-equilibrium Green's functions to quantum master equations for the density matrix and out-of-time-order correlators: steady state and adiabatic dynamics*. 2021. arXiv: 2103.04373 [cond-mat.mes-hall] (cit. on pp. 47, 49).

[69] Alexander Cyril Hewson. *The Kondo Problem to Heavy Fermions*. Cambridge Studies in Magnetism. Cambridge University Press, 1993. DOI: 10.1017/CBO9780511470752 (cit. on p. 48).

[70] Gerhard Dorn, Enrico Arrigoni, and Wolfgang von der Linden. "Efficient energy resolved quantum master equation for transport calculations in large strongly correlated systems". In: *Journal of Physics A: Mathematical and Theoretical* 54.7 (Jan. 2021), p. 075301. DOI: 10.1088/1751-8121/abd736. URL: https://doi.org/10.1088/1751-8121/abd736 (cit. on p. 48).

[71] G. C. Wick. "The Evaluation of the Collision Matrix". In: *Phys. Rev.* 80 (2 Oct. 1950), pp. 268–272. DOI: 10.1103/PhysRev.80.268. URL: https://link.aps.org/doi/10.1103/PhysRev.80.268 (cit. on pp. 49, 126).

[72] Carlos Ortega Taberner. "Periodically driven S-QD-S junction Floquet dynamics of Andreev Bound states". In: 2017 (cit. on p. 50).

[73] A. P. Jauho. *Introduction to the Keldysh Nonequilibrium Green Function Technique*. Oct. 2006. URL: https://nanohub.org/resources/1877 (cit. on pp. 50, 126, 127).

[74] Antti-Pekka Jauho, Ned S. Wingreen, and Yigal Meir. "Time-dependent transport in interacting and noninteracting resonant-tunneling systems". In: *Phys. Rev. B* 50 (8 Aug. 1994), pp. 5528–5544. DOI: 10.1103/PhysRevB.50.5528. URL: https://link.aps.org/doi/10.1103/PhysRevB.50.5528 (cit. on p. 51).

[75] Christoph Wolf et al. "Efficient Ab Initio Multiplet Calculations for Magnetic Adatoms on MgO". In: *The Journal of Physical Chemistry A* 124.11 (2020). PMID: 32098473, pp. 2318–2327. DOI: 10.1021/acs.jpca.9b10749. eprint: https://doi.org/10.1021/acs.jpca.9b10749. URL: https://doi.org/10.1021/acs.jpca.9b10749 (cit. on pp. 62, 72, 82).

[76] Anna Ferrari. "Interface geometry of Ag thin films supported at the MgO(1 0 0) surface: An ab-initio periodic study". In: *Chemical Physics Letters - CHEM PHYS LETT* 400 (Dec. 2004), pp. 541–547. DOI: 10.1016/j.cplett.2004.11.012 (cit. on p. 65).

[77] O.E. Taurian, M. Springborg, and N.E. Christensen. "Self-consistent electronic structures of MgO and SrO". In: *Solid State Communications* 55.4 (1985), pp. 351–355. ISSN: 0038-1098. DOI: https://doi.org/10.1016/0038-1098(85)90622-2. URL: https://www.sciencedirect.com/science/article/pii/0038109885906222 (cit. on p. 66).

[78] Sanliang Ling, Matthew B. Watkins, and Alexander L. Shluger. "Effects of Oxide Roughness at Metal Oxide Interface: MgO on Ag(001)". In: *The Journal of Physical Chemistry C* 117.10 (2013), pp. 5075–5083. DOI: 10.1021/jp311141k. eprint: https://doi.org/10.1021/jp311141k. URL: https://doi.org/10.1021/jp311141k (cit. on p. 66).

[79] Alexander F. Otte et al. "The role of magnetic anisotropy in the Kondo effect". In: *Nature Physics* 4.11 (Sept. 2008), pp. 847–850. ISSN: 1745-2481. DOI: 10.1038/nphys1072. URL: http://dx.doi.org/10.1038/nphys1072 (cit. on p. 68).

[80] Taeyoung Choi and Jay A Gupta. "Building blocks for studies of nanoscale magnetism: adsorbates on ultrathin insulating Cu 2 N". In: *Journal of Physics: Condensed Matter* 26.39 (2014), p. 394009 (cit. on p. 68).

[81] E. Dagotto. *Nanoscale Phase Separation and Colossal Magnetoresistance*. Springer-Verlag, Berlin, 2003 (cit. on pp. 72, 73, 120).

[82] A Ferrón, F Delgado, and J Fernández-Rossier. "Derivation of the spin Hamiltonians for Fe in MgO". In: *New J. Phys.* 17.3 (2015), p. 033020 (cit. on pp. 72, 119).

[83] F. Delgado, J. J. Palacios, and J. Fernández-Rossier. "Spin-transfer torque on a single magnetic adatom". In: *Phys. Rev. Lett.* 104 (2010), p. 026601 (cit. on p. 73).

[84] S. Loth et al. "Controlling the state of quantum spins with electric currents". In: *Nature Physics* 6 (2010), pp. 340–344 (cit. on p. 73).

[85] P. W. Anderson. "Localized Magnetic States and Fermi-Surface Anomalies in Tunneling". In: *Phys. Rev. Lett.* 17 (1966), p. 95 (cit. on p. 73).

[86] J. R. Schrieffer and P. A. Wolff. "Relation between the Anderson and Kondo Hamiltonians". In: *Phys. Rev.* 149 (1966), pp. 491–492 (cit. on pp. 73, 86).

[87] Nicolás Lorente and Jean-Pierre Gauyacq. "Efficient Spin Transitions in Inelastic Electron Tunneling Spectroscopy". In: *Phys. Rev. Lett.* 103 (2009), p. 176601 (cit. on p. 75).

[88] J. Fernández-Rossier. "Theory of Single-Spin Inelastic Tunneling Spectroscopy". In: *Phys. Rev. Lett.* 102 (2009), p. 256802 (cit. on p. 75).

[89] Jun John Sakurai. *Modern quantum mechanics; rev. ed*. Reading, MA: Addison-Wesley, 1994. URL: https://cds.cern.ch/record/1167961 (cit. on pp. 76, 106, 124).

[90] Susanne Baumann. "Investigation of the unusual magnetic properties of Fe and Co on MgO with high spatial, energy and temporal resolution". PhD thesis. University_of_Basel, 2015. URL: http://edoc.unibas.ch/diss/DissB_11597 (cit. on p. 77).

[91] Samir Lounis. "Theory of scanning tunneling microscopy". In: *ArXiv:1404.0961* (2014) (cit. on p. 81).

[92] J. Tersoff and D. R. Hamann. "Theory of the scanning tunneling microscope". In: *Phys. Rev. B* 31 (2 Jan. 1985), pp. 805–813. DOI: 10.1103/PhysRevB.31.805 (cit. on p. 81).

[93] Y. Bae et al. "Enhanced quantum coherence in exchange coupled spins via singlet-triplet transitions". In: *Science Advances* 4.11 (2018). DOI: 10.1126/sciadv.aau4159. eprint: https://advances.sciencemag.org/content/4/11/eaau4159.full.pdf.

URL: https://advances.sciencemag.org/content/4/11/eaau4159 (cit. on pp. 84, 104, 106, 112, 113, 115).

[94] John Clarke Slater and James C Phillips. "Quantum theory of molecules and solids Vol. 4: The self-consistent field for molecules and solids". In: *Physics Today* 27 (1974), p. 49 (cit. on p. 119).

[95] V. V. Mazurenko et al. "Correlation effects in insulating surface nanostructures". In: *Phys. Rev. B* 88 (8 Aug. 2013), p. 085112. DOI: 10.1103/PhysRevB.88.085112 (cit. on p. 120).

[96] A. Ferrón, J. L. Lado, and J. Fernández-Rossier. "Electronic properties of transition metal atoms on $Cu_2N(100)$". In: *Phys. Rev. B* 92 (17 Nov. 2015), p. 174407. DOI: 10.1103/PhysRevB.92.174407 (cit. on p. 120).

[97] H. A. Bethe. "Termaufspaltung in Kristallen". In: *Annalen der Physik* 395.2 (1929), pp. 133–208. DOI: https://doi.org/10.1002/andp.19293950202 (cit. on p. 120).

[98] M. Kepenekian et al. "Simulations of Constant Current STM Images of Open-Shell Systems". In: *Imaging and Manipulating Molecular Orbitals*. Ed. by Leonhard Grill and Christian Joachim. Berlin, Heidelberg: Springer Berlin Heidelberg, 2013, pp. 117–136. ISBN: 978-3-642-38809-5 (cit. on p. 124).

[99] L. V. Keldysh. "Diagram technique for nonequilibrium processes". In: *Soviet Physics JETP* 20 (47 Apr. 1965), pp. 1018–1026 (cit. on p. 126).